Surface Engineering of Lanthanide-Doped Nanoparticles for Assays, Sensing and Theranostic Applications

DISSERTATION ZUR ERLANGUNG DES DOKTORGRADES DER NATURWISSENSCHAFTEN (DR. RER. NAT.) DER FAKULTÄT CHEMIE UND PHARMAZIE

DER UNIVERSITÄT REGENSBURG

DEUTSCHLAND

vorgelegt von

Markus Buchner

aus Ergoldsbach

Im Jahr **2018**

Die vorliegende Dissertation entstand in der Zeit von September 2014 bis Februar 2018 am Institut für Analytische Chemie, Chemo- und Biosensorik der Universität Regensburg.

Die Arbeit wurde angeleitet von Prof. Dr. Antje J. Bäumner und Dr. Thomas Hirsch.

Promotionsgesuch eingereicht am: 08.02.2018

Kolloquiumstermin: 23.03.2018

Prüfungsausschuss:

Vorsitzender: Prof. Dr. Hubert Motschmann

Erstgutachter: Prof. Dr. Antje J. Bäumner

Zweitgutachter: PD Dr. Miriam Breunig

Drittprüfer: Prof. Dr. Joachim Wegener

ACKNOWLEDGEMENTS

Table of Contents

1 INTRODUCTION TO LANTHANIDE-DOPED NANOPARTICLES

Nanomaterials, especially nanoparticles, have become very popular in our modern society. Most people are not necessarily aware which products of their daily life contain nanomaterials. For example, silver nanoparticles are widely used for their antimicrobial properties in refrigerators, clothes, but also in baby bottles.[1] Microscale TiO_2 particles are known for their ability to strongly scatter light due to their high refractive index and are therefore utilized as white pigment in painting, food (E number: 171) and in synthetic materials.[2] By downsizing to the nanoscale range their ability to efficiently scatter light gets lost, however new application possibilities in sunscreens and textile fibers are offered.[3] The size-dependent properties of nanoparticles play an important role in toxicity. Usually, smaller particles are suspected to be taken up faster by cells and therefore may accumulate in higher concentrations in the tissue as cells may not be able to expel them again. While many studies deal with this effect, the sheer breadth of nanoparticle chemistry, nanoparticle size, the number of biological and environmental systems affected is so large that much information is missing especially regarding long-term toxicity induced by nanoparticles.[4,5,6]

Colloidal gold (gold nanoparticles), for example, have been used for centuries for glass coloring, however only with the development of transmission electron microscopy discovery and characterization of nanoparticles was possible in the late 20th century (**Figure 1.1**).
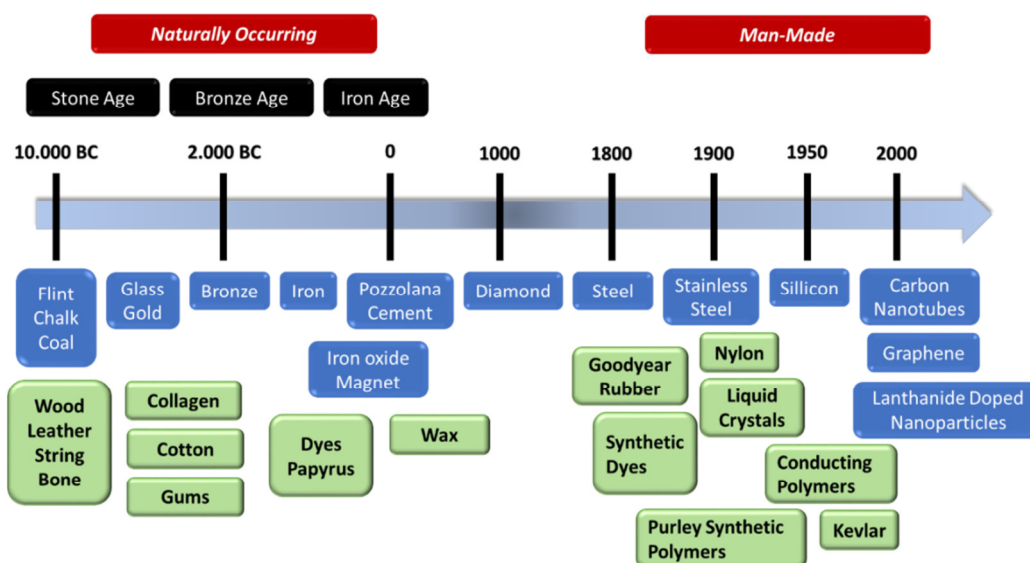
Figure 1.1‖ Selection of important materials discovered by humans are presented in a timeline, separating between naturally occurring and "man-made" materials.

Nanoparticles with size-dependent material properties attract the attention of researcher more and more. The increased surface-to-volume ratio can accelerate chemical reactions by faster mass transfer rates. Nanoparticles have also been investigated for drug delivery due their high drug loading capacity and in bioanalytical chemistry they are promising for sensor development. Here, especially their potential to lower limits of detection through inherent signal enhancement in many transduction principles is of special interest.

A specific classification of nanomaterials is based on their chemical and physical properties, e.g. between magnetic, catalytically active or luminescent nanoparticles. Among the luminescent nanomaterials a wide variety regarding composition and optical properties exists such as semiconductor-type quantum dots,[7] carbon dots[8], metal nanoclusters,[9] metal-doped nanoparticles[10] and organic-inorganic hybrid materials.[11] The luminescence in carbon dots, quantum dots or metal nanoclusters is related to the quantum-confinement effects, where the position of the emission bands depends on the size and shape of the particles. As a consequence, it is difficult to synthesize nanoparticles with a desired diameter, without changing the optical properties. In contrast, the emission bands of luminescent organic-inorganic hybrid nanomaterials and metal doped nanoparticles are not influenced by the size; however, intensity and ratios of the bands might show size-dependent variations.[10]

Among the metal doped nanoparticles, the lanthanide doped nanoparticles have extraordinary optical properties. Lanthanide ions have the electron configuration [Xe] $4f^n$ (n = 0-14).[12] The energy levels are well defined since they are shielded by the filled $5s^2$ and $5p^6$ shells. As a consequence, the inner-shell 4f – 4f transitions are sharp and specific for each lanthanide ion, ranging from the UV to the near infrared. However, the 4f - 4f transitions are formally forbidden due to Laporte´s parity rule, thereby the excited f-states have very long luminescent lifetimes, favorable for time-resolved detection systems in biological samples, minimizing background fluorescence.

Considering the different energy levels of the lanthanide ions shown in **Figure 1.2** defined energy ladders with short energy gaps can be found for most of the lanthanide ions, indicating the probability of non-radiative deactivation processes.[13] Eu^{3+}, Gd^{3+} and Tb^{3+} are an exception among the lanthanide ions. The large energy gaps of these ions enable luminescence measurements with large *Stokes* shifted emissions. Gd^{3+} is only able to emit UV light and is less interesting for bioanalytical applications, since UV-light is strongly absorbed by biological samples and can lead to phototoxicity.
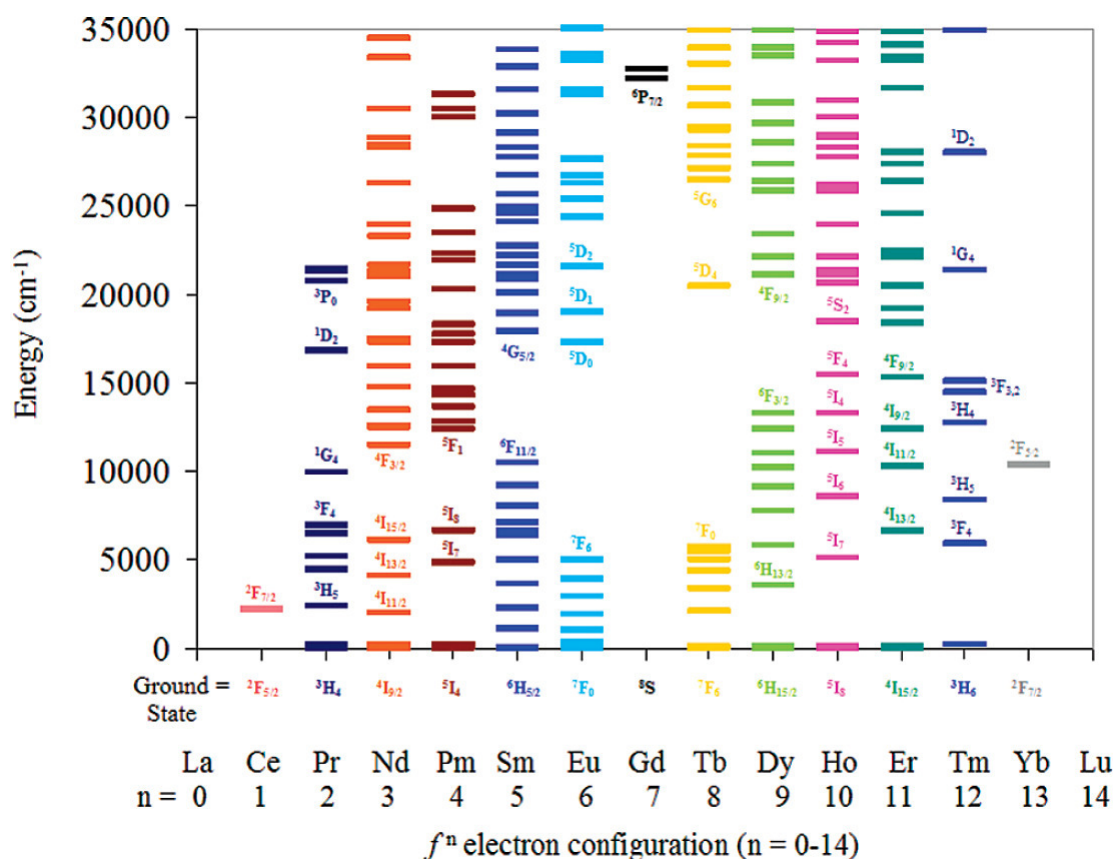
Figure 1.2‖ Energy diagram for the trivalent lanthanide ions with f^n electron configuration (n = 0-14). The electronic states of the lanthanide ions are presented as horizontal lines in cm^{-1}. Reprinted with permission from Ref. 14. Copyright 2009 American Chemical Society.

Organic dyes usually have broad absorption and emission bands with *Stokes* shifts less than 50 nm due to their vibrations levels attached to the excited states. With their line like emissions and their large *Stokes* shifted emissions lanthanide ions are thus more attractive than organic dyes for measurements in biological samples, since background luminescence is significantly reduced.

One major drawback of the lanthanides is their relatively low molar absorption coefficient (below 1 $M^{-1} \cdot cm^{-1}$). In comparison, good organic dyes have coefficients in the range of 25,000 to 250,000 $M^{-1} \cdot cm^{-1}$.[15] Since direct excitation of the Ln^{3+} ions leads to very low luminescence signals, high energy excitation or light harvesting molecules have been used to enhance the luminescence of the lanthanide ions. These so-called antenna ligands are usually coordinated to lanthanide ions, absorbing and transferring the excitation light to Ln^{3+} in the center. Due to the coordination of the ligands water molecules are repressed, which is highly beneficial as the long lifetime of the lanthanide ions can be easily quenched via OH groups in close proximity. The light harvesting molecules typically are organic dyes, which are themselves prone to photobleaching,

however, as Ln^{3+} ions are good quenchers of the triplet states, photobleaching of the organic dyes is reduced in these complexes.[13]

Another strategy to overcome the low absorption coefficients of the lanthanide ions and water quenching is the entrapment of lanthanide ions in host materials. Furthermore, entrapment of Ln^{3+} ions inside solid host materials causes a distortion of the orbital symmetry, which can increase the probability of the f-f transitions.[16] Inorganic nanoparticles like Y_2O_3,[17] Gd_2O_3,[18] $NaYF_4$,[19] CeO_2[20] or $CaMoO_4$[21] nanoparticles have been synthesized as a host lattice for europium or terbium ions. A suitable secondary effect is, when the new host lattice contributes to the lanthanide emissions by charge transfer processes. This can lead to dramatically enhanced luminescent properties, for example in $GdVO_4$:Eu nanoparticles. Other ways to enhance the luminescence properties are antenna ligands, which can also be utilized in nanoparticles, by binding the light harvesting molecules directly to the surface of the nanoparticles.[22,23]

Upconversion Nanoparticles

Upconversion nanoparticles are a special group of lanthanide doped nanoparticles, able to convert near infrared light to UV and visible light by multiphoton processes. The non-linear process was first discovered in bulk materials doped with Yb^{3+} and Tm^{3+} ions in the 1960s.[24] Generally, several mechanisms are described in literature, which are leading to upconversion: photon avalanche (PA), excited state absorption (ESA) and energy transfer upconversion (ETU).[25] PA requires a high pump intensity to induce the cycle process and is rarely observed.[26] The ESA and the ETU mechanisms include both a sequential absorption of two or more photons to populate higher energy levels. However, in the ESA process the sensitizer and the emitting ion are identical. Both models require laser irradiation due to the low molar absorption coefficient of the lanthanide ions. In the ETU process the energy is transferred stepwise from sensitizer ions to emitting ions (activators). Most upconversion materials are designed for utilizing the ETU process to generate anti *Stokes* shifted emissions, since this is the most efficient mechanism and can be achieved with low laser power irradiation.
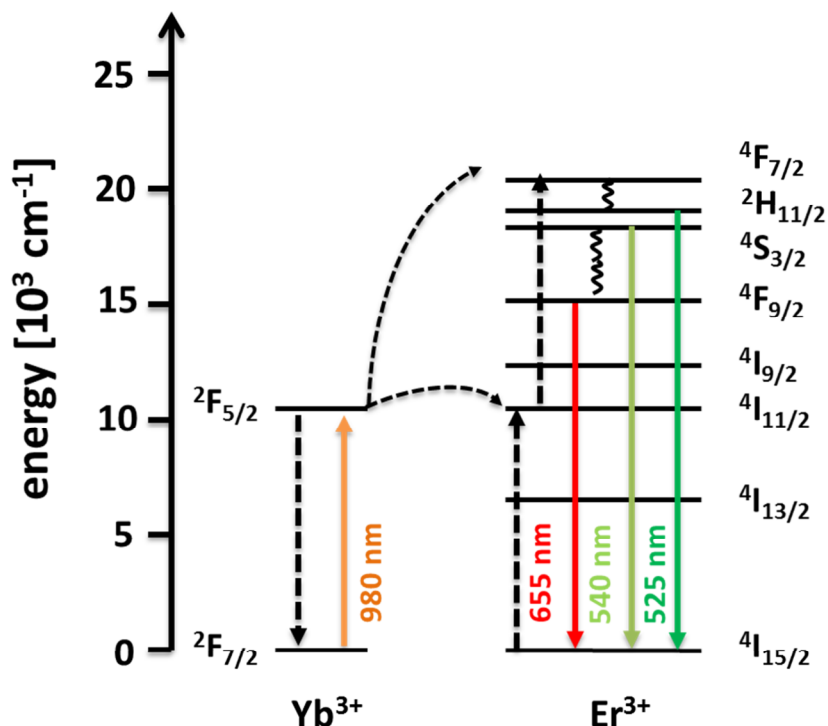
Figure 1.3 ‖ ETU mechanism of an Yb^{3+}/Er^{3+} system for the generation of upconversion luminescence is presented. The dotted black arrows represent photon transmission. The colored arrows signify a distinct absorption or emission of a photon; the curly black lines indicate non-radiative relaxations.

In **Figure 1.3** the ETU mechanism for the upconversion process of an Yb^{3+}/Er^{3+} system is shown.[27] First a photon gets absorbed by a so-called sensitizer ion, which then transfers the energy to emitting ions. As sensitizer ions Yb^{3+} has been established as the most suitable ones, since they absorb near infrared light at a wavelength of 980 nm with a relatively high absorption coefficient ($10\ M^{-1}cm^{-1}$) compared to other lanthanide ions.[28] Another advantage is that 980 nm lasers are comparatively cheap and commercially available.[29] The excited Yb^{3+} in the $^5F_{5/2}$ state is able to transfer the energy to excited state levels of adjacent lanthanides ions, e.g. to Er^{3+} to populate the $^4I_{11/2}$ energy level. Subsequent absorption and transfer of another photon to the excited Er^{3+} leads then to the population of the $^4F_{7/2}$ energy level. Two main emissions of Er^{3+} after non-radiative relaxation from the $^4F_{7/2}$ state are the green emissions from $^2H_{11/2}$ and $^4S_{3/2}$ to the ground state, resulting in emissions at 525 nm and 540 nm, respectively. The third main emission leads to red luminescence at 655 nm, following the transition of $^4F_{9/2}$ to the ground state. Other popular upconversion systems are the combinations Yb^{3+}/Ho^{3+} and Yb^{3+}/Tm^{3+}, where even UV-light can be generated ($^1D_2 \rightarrow\ ^3H_6$, 360 nm) by a four-photon process.[30]

In general, a host lattice must meet several requirements for high upconversion efficiency. First of all, the host lattice has to be easily doped with the sensitizer and activator ions. The dopants should be distributed homogenously throughout the whole nanocrystal to

achieve optimum and controllable doping ratios. This demands similar ionic radii and charge of the Ln^{3+} with a cation of the host lattice, also to reduce crystal defects.[31] Another requirement is low phonon energy of the nanocrystals to minimize non-radiative deactivation processes and to enhance the radiative emissions. Fluoride host lattices are known to have lowest phonon energies (< 350 cm^{-1}).[27] Considering bioanalytical applications the host material has also to be thermodynamically stable, non-toxic and chemically inert. For example, leaching of ions can significantly influence viability of cells or lead to undesired side reactions, like complexation reactions.

Furthermore, the crystal structure of the host material affects the upconversion efficiency. The distance between sensitizer and emitting ions as well as symmetries around the Ln^{3+} get changed by variations of the crystal structure. Up to now the most efficient and favored host lattice is hexagonal β-$NaYF_4$ with phonon energies (below 350 cm^{-1}) showing ten times higher brighter upconversion luminescence compared to cubic α-$NaYF_4$.[32] The ionic radius of Y^{3+} is similar to the radii of the lanthanides ions facilitating the doping with Ln^{3+}, without excessive deformations of the host lattice. Other popular host lattices are Ln_2O_3, LnF_3 and YVO_4, which have higher phonon energies and therefore have lower upconversion efficiency.[33]

In contrary to nanoparticles connected to the quantum-confinement effect the position of the emission bands of the upconverting nanoparticles are fixed and are independent of the host lattice. Only the intensity ratios of the anti-*Stokes* shifted emissions depend on the applied laser power (multi-photon process), the doping ratio of the lanthanide ions, the size of the nanocrystals, and the microenvironment of the lanthanide ions. The influence of this parameters demands accurate characterization of the upconverting nanoparticles or in general for all lanthanide doped nanoparticles. The size of nanocrystals can be evaluated by transmission electron microscopy (TEM) and dynamic light scattering (DLS). While by evaluating TEM-images the exact diameter of the nanoparticles together with the particle size distribution can be determined, DLS measurements give valuable information about the dispersed nanoparticles, e.g. agglomeration of the nanoparticles. X-ray diffraction (XRD) measurements are important for the determination of the crystal phase, which can have distinct influence on the optical properties of the nanoparticles. Regarding doping ratio inductively coupled plasma optical emission spectrometry (ICP-OES) or mass spectrometry (ICP-MS) are useful techniques for the determination of the lanthanide ion content in the nanocrystals.

Thermogravimetric analysis (TGA), fourier-transform infrared spectroscopy (FTIR) and mass spectroscopy are methods to determine the surface architecture of the nanoparticles. After synthesis nanoparticles are stabilized by several organic ligands,

preventing agglomeration of the nanoparticles. The properties of the ligands determine the stability of the nanoparticles in different solvents. For bioanalytical applications surface modifications are necessary to enable colloidal stability of the nanocrystals in aqueous solutions or to functionalize the nanoparticles. The three main techniques for surface modification are ligand exchange, coating with amphiphilic polymers and growing of a silica shell.[34] Detailed presentation of the different surface modification techniques is given in **Chapter 4**.

Enhancement Strategies for UCNPs

For bioanalytical applications reduced luminescence brightness of the UCNPs in aqueous dispersions can be observed. Two different effects contribute to this reduction: A) Continuous attenuation of the excitation light by a local absorption band of water at 980 nm accompanied by heating effects of the samples. B) Quenching of the upconversion luminescence caused due to O-H vibrations go along with changes in the peak ratios of the UCNPs.[35]

Several strategies have been developed to enhance the luminescence properties of the UCNPs in aqueous dispersions (**Figure 1.4**): A) surface passivation by synthesis of core-shell nanoparticles, B) Host lattice manipulation, C) Improving the excitation efficiency or D) Plasmonic enhancement.[36]

Surface Passivation　　**Broadband Sensitization**

Host Lattice Manipulation　　**Plasmonic Enhancement**
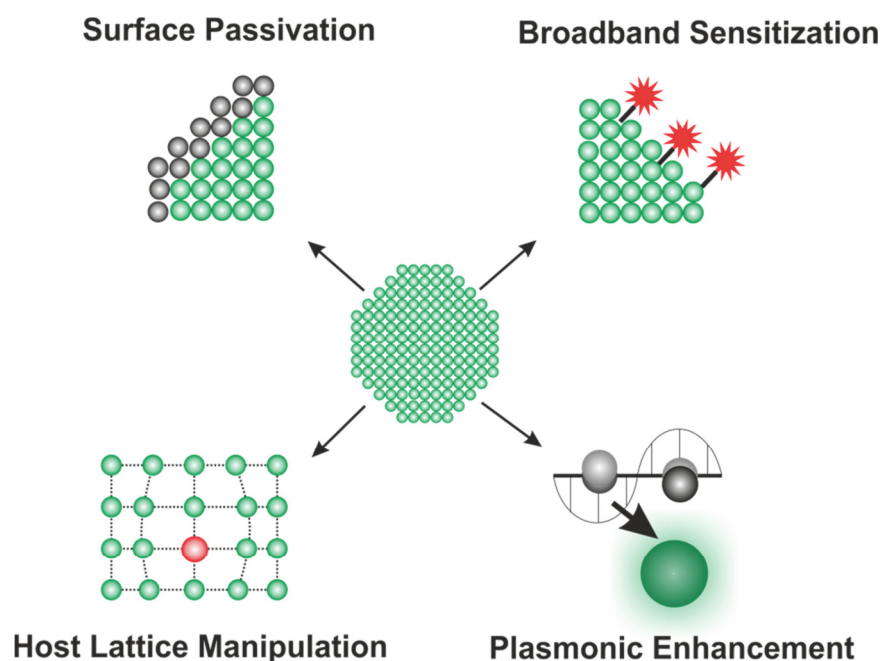
Figure 1.4‖ Enhancement strategies for lanthanide doped nanoparticles are presented: Surface passivation, broadband sensitization, host lattice manipulation and plasmonic enhancement.

Surface passivation by growing a shell around the core-particles is a well-established method to reduce crystals defects and surface quenching effects, therefore increase the emission of the UCNPs. Zhang et al. (2012) showed that by a homogenous shell growth of $NaGdF_4$ on $NaYF_4$,Yb,Er core particles surface defects on the nanocrystal can be passivated, consequently an enhancement in emission intensity and lifetime can be observed.[37] Fischer et al. (2016) demonstrated that the maximum upconversion quantum yield was obtained for a shell thickness of around 4 nm for $NaYF_4$:Yb,Er@$NaLuF_4$ nanoparticles.[38] For FRET based applications the thickness of the shell has to be adapted for high luminescent quantum yield of the particles and at the same time high energy transfer efficiency.[39]

The emission intensity of upconverting nanoparticles is influenced by the crystal phase, the local crystal field of Ln^{3+} ions in the host matrix and the Ln^{3+}-Ln^{3+} distance. Therefore, host lattice manipulation is an effective way to enhance the luminescence properties of upconverting nanoparticles. Co-doping with small alkali metal ions like Li^+ alters crystal field symmetries, leading to enhanced optical properties.[40] Hu et al. (2017) combined the Li^+ co-doping with the growth of a passivating shell around $NaLuF_4$:Yb,Tm nanoparticles to enhance the upconversion luminescence synergistically by a factor of 210.[41] Transition metal ions like Sc^{3+}, Mn^{2+} and Fe^{3+} have been also inserted to tune the upconversion emission or to selectively enhance single emission bands inside the nanocrystals.[42,43,44]

Improving the excitation efficiency is another strategy to enhance the luminescence properties of UCNPs in aqueous dispersions.[45] This can either be achieved by enhancing the absorption at 980 nm by light harvesting NIR dyes or by shifting the excitation wavelength to shorter wavelength by co-doping of the nanocrystals with Nd^{3+} ions. The light harvesting NIR dyes or also called antenna ligands have to be bound directly on the surface of the nanocrystals enabling an energy transfer to the sensitizer ions, first shown by Zou et al. (2012).[46] Sensitization with NIR dyes with their broad absorptions bands provides more flexibility regarding the excitation wavelength considering the heating effects of water by 980 nm irradiation. Prasad et al. (2016) achieved UCNPs with a quantum yield of 9.2% by combining the surface passivation by formation of a shell, co-doped with Nd^{3+}, with the light harvesting abilities of NIR dyes.[47] However, NIR dyes are prone to photobleaching, especially considering higher excitation powers for the excitation, lowering the application in long-term experiments.

By co-doping of the nanoparticles with Nd^{3+} the excitation wavelength can be shifted to 808 nm, minimizing water absorption of the excitation light, reducing the overheating effect.[48] The energy, absorbed by Nd^{3+} ions, is first transferred to Yb^{3+} and then to the activator ions (Er^{3+}, Tm^{3+}). The energy levels of Nd^{3+} are numerous compared with the energy levels of Yb^{3+} limiting the doping concentrations of Nd^{3+} up to 1 mol%. Higher

concentration would lead to cross relaxations between the activator ions and Nd^{3+} ions, minimizing the efficiency of the upconversion process. Sophisticated core-shell architectures to separate the sensitizer and activator ions enable doping concentration of Nd^{3+} up to 20 mol% for effective upconversion.[49,50] Yb^{3+} acts as a bridging sensitizer, transferring the energy from the active shell to the core of the nanocrystals.

Plasmonic enhancement is another strategy to improve the absorption and emission process of upconverting nanoparticles. Noble metal nanoparticles, mostly gold or silver nanoparticles, can influence neighboring activator ions either by concentrating the incident field or modifying the local density of the energy levels leading either to enhancing the absorption efficiency or to faster radiative decay rates. Several different UC-plasmonic structures have been developed to enhance the upconverting efficiency.[51,52,53]

References

1   J. I. Choi, S. J. Chae, J. M. Kim, J. C. Choi, S. J. Park, H. J. Choi, H. Bae and H. J. Park, Potential silver nanoparticles migration from commercially available polymeric baby products into food simulants, *Food Addit. Contam. Part A Chem. Anal. Control Expo. Risk. Assess.*, **2018**, 1–10.

2   D. P. Macwan, P. N. Dave and S. Chaturvedi, A review on nano-TiO_2 sol–gel type syntheses and its applications, *J. Mater. Sci.*, **2011**, 46, 3669–3686.

3   M. Ge, C. Cao, J. Huang, S. Li, Z. Chen, K.-Q. Zhang, S. S. Al-Deyab and Y. Lai, A review of one-dimensional TiO_2 nanostructured materials for environmental and energy applications, *J. Mater. Chem. A*, **2016**, 4, 6772–6801.

4   L. Armand, A. Tarantini, D. Beal, M. Biola-Clier, L. Bobyk, S. Sorieul, K. Pernet-Gallay, C. Marie-Desvergne, I. Lynch, N. Herlin-Boime and M. Carriere, Long-term exposure of A549 cells to titanium dioxide nanoparticles induces DNA damage and sensitizes cells towards genotoxic agents, *Nanotoxicology*, **2016**, 10(7), 913.

5   B. Annangi, L. Rubio, M. Alaraby, J. Bach, R. Marcos and A. Hernández, Acute and long-term in vitro effects of zinc oxide nanoparticles, *Arch. Toxicol.*, **2016**, 90(9), 2201.

6   X. Liang, H. Wang, Y. Zhu, R. Zhang, V. C. Cogger, X. Liu, Z. P. Xu, J. E. Grice and M. S. Roberts, Short- and long-term tracking of anionic ultrasmall nanoparticles in kidney, *ACS Nano*, **2016**, 10(1), 387.

7   B. S. Mashford, M. Stevenson, Z. Popovic, C. Hamilton, Z. Zhou, C. Breen, J. Steckel, V. Bulovic, M. Bawendi, S. Coe-Sullivan and P. T. Kazlas, High-efficiency

quantum-dot light-emitting devices with enhanced charge injection, *Nature Photon*, **2013**, 7, 407–412.

8   P. Zuo, X. Lu, Z. Sun, Y. Guo and H. He, A review on syntheses, properties, characterization and bioanalytical applications of fluorescent carbon dots, *Microchim. Acta*, **2016**, 183, 519.

9   L.-Y. Chen, C.-W. Wang, Z. Yuan and H.-T. Chang, Fluorescent gold nanoclusters, *Anal. Chem.*, **2015**, 87, 216–229.

10   C. Feldmann, Luminescent nanomaterials, *Nanoscale*, **2011**, 3, 1947–1948.

11   L. Armelao, S. Quici, F. Barigelletti, G. Accorsi, G. Bottaro, M. Cavazzini and E. Tondello, Design of luminescent lanthanide complexes, *Coord. Chem. Rev.*, **2010**, 254, 487–505.

12   J.-C. G. Bünzli and C. Piguet, Taking advantage of luminescent lanthanide ions, *Chem. Soc. Rev.*, **2005**, 34, 1048–1077.

13   J.-C. G. Bünzli, Lanthanide luminescence for biomedical analyses and imaging, *Chemi. Rev.*, **2010**, 110, 2729–2755.

14   E. G. Moore, A. P. S. Samuel and K. N. Raymond, From antenna to assay, *Acc. Chem. Res.*, **2009**, 42, 542–552.

15   U. Resch-Genger, M. Grabolle, S. Cavaliere-Jaricot, R. Nitschke and T. Nann, Quantum dots versus organic dyes as fluorescent labels, *Nat. Methods*, **2008**, 5(9), 763.

16   S. Han, R. Deng, X. Xie and X. Liu, Enhancing luminescence in lanthanide-doped upconversion nanoparticles. *Angew. Chem. Int. Ed.*, **2014**, 53, 11702–11715.

17   M. G. Ivanov, I. V. Krutikova, U. Kynast, M. Lezhnina and I. S. Puzyrev, Laser-synthesized Y_2O_3:Eu^{3+} nanophosphors and their stabilization in water suspensions, *Opt. Mater.*, **2017**, 74, 67–75.

18   T. K. Anh, P. T. M. Chau, N. T. Q. Hai, V. T. T. Ha, H. van Tuyen, S. Bounyavong, N. T. Thanh and Q. Le Minh, Facile fabrication and properties of Gd_2O_3:Eu^{3+}, Y_2O_3:Eu^{3+} nanophosphors and Gd_2O_3:Eu^{3+}/silica, Y_2O_3:Eu^{3+}/silica nanocomposites, *J. Electron. Mater.*, **2018**, 47, 585–593.

19   C. Li, Z. Quan, J. Yang, P. Yang and J. Lin, Highly uniform and monodisperse beta-$NaYF_4$: Ln^{3+} (Ln = Eu, Tb, Yb/Er, and Yb/Tm) hexagonal microprism crystals: Hydrothermal synthesis and luminescent properties, *Inorg. Chem.*, **2007**, 46, 6329–6337.

20   L. Li, H. K. Yang, B. K. Moon, Z. Fu, C. Guo, J. H. Jeong, S. S. Yi, K. Jang and H. S. Lee, Photoluminescence Properties of CeO_2:Eu^{3+} nanoparticles synthesized by a sol-gel method, *J. Phys. Chem. C*, **2009**, 113, 610–617.

21   R. Wang, Red Fluorescence Enhancement via Using the Charge Compensation and Co-doping WO_3 in $CaMoO_4$:Eu^{3+} Phosphor for Ultraviolet Converted LEDs, *JIOP*, **2017**, 27, 1028–1036.

22   S. W. Li, H. J. Ren and S. G. Ju, Sensitized luminescence of LaF_3:Eu^{3+} nanoparticles through pyromellitic acid, *J. Nanosci. Nanotech.*, **2014**, 14, 3677–3682.

23   L. J. Charbonnière, J.-L. Rehspringer, R. Ziessel and Y. Zimmermann, Highly luminescent water-soluble lanthanide nanoparticles through surface coating sensitization, *New J. Chem.*, **2008**, 32, 1055.

24   F. Auzel, Upconversion and anti-Stokes processes with f and d ions in solids, *Chem. Rev.*, **2004**, 104, 139–173.

25   F. Zhang, Photon upconversion nanomaterials, *Springer Berlin Heidelberg*, **2015**.

26   J. Zhou, Q. Liu, W. Feng, Y. Sun and F. Li, Upconversion luminescent materials: advances and applications, *Chem. Rev.*, **2015**, 115, 395–465.

27   M. Haase and H. Schäfer, Upconverting nanoparticles, *Angew. Chem. Inter. Ed.*, **2011**, 50, 5808–5829.

28   J.-C. G. Bünzli, On the design of highly luminescent lanthanide complexes, *Coord. Chem. Rev.*, **2015**, 293-294, 19–47.

29   E. Y. Chan, J. C. Adams, J. M. Saint Clair, K. A. Morrison and M. Sosa, R. M. Rao, S. A. Dianat and M. D. Zoltowski, Application of COTS high-speed 980-nm pump laser diode and driver for free-space laser communication terminal, *SPIE*, **1999**, pp. 79–86.

30   L. M. Jin, X. Chen, C. K. Siu, F. Wang and S. F. Yu, Enhancing multiphoton upconversion from $NaYF_4$:Yb/Tm@$NaYF_4$ core–shell nanoparticles via the use of laser cavity, *ACS Nano*, **2017**, 11(1), 843.

31   R. Naccache, Q. Yu and J. A. Capobianco, The Fluoride Host: Nucleation, Growth, and upconversion of lanthanide-doped nanoparticles, *Adv. Opt. Mat.*, **2015**, 3, 482–509.

32   J.-H. Zeng, J. Su, Z.-H. Li, R.-X. Yan and Y.-D. Li, Synthesis and Upconversion Luminescence of Hexagonal-Phase $NaYF_4$:Yb, Er^{3+} Phosphors of Controlled Size and Morphology, *Adv. Mater.*, **2005**, 17, 2119–2123.

33   F. Wang and X. Liu, Recent advances in the chemistry of lanthanide-doped upconversion nanocrystals, *Chem. Soc. Rev.*, **2009**, 38, 976–989.

34   V. Muhr, S. Wilhelm, T. Hirsch and O. S. Wolfbeis, Upconversion nanoparticles: From hydrophobic to hydrophilic surfaces, *Acc. Chem. Res.*, **2014**, 47, 3481–3493.

35   C. Würth, M. Kaiser, S. Wilhelm, B. Grauel, T. Hirsch and U. Resch-Genger, Excitation power dependent population pathways and absolute quantum yields of upconversion nanoparticles in different solvents, *Nanoscale*, **2017**, 9, 4283–4294.

36   U. Resch-Genger and H. H. Gorris, Perspectives and challenges of photon-upconversion nanoparticles - Part I: routes to brighter particles and quantitative spectroscopic studies. *Anal. Bioanal. Chem.*, **2017**, 409, 5855–5874.

37   F. Zhang, R. Che, X. Li, C. Yao, J. Yang, D. Shen, P. Hu, W. Li and D. Zhao, Direct imaging the upconversion nanocrystal core/shell structure at the subnanometer level, *Nano letters*, **2012**, 12, 2852–2858.

38   S. Fischer, N. D. Bronstein, J. K. Swabeck, E. M. Chan and A. P. Alivisatos, Precise tuning of surface quenching for luminescence enhancement in core-shell lanthanide-doped nanocrystals, *Nano letters*, **2016**, 16, 7241–7247.

39   V. Muhr, C. Würth, M. Kraft, M. Buchner, A. J. Baeumner, U. Resch-Genger and T. Hirsch, particle-size-dependent förster resonance energy transfer from upconversion nanoparticles to organic dyes, *Anal. Chem.*, **2017**, 89(9), 4868.

40   C. Zhao, X. Kong, X. Liu, L. Tu, F. Wu, Y. Zhang, K. Liu, Q. Zeng and H. Zhang, Li^+ ion doping: an approach for improving the crystallinity and upconversion emissions of $NaYF_4:Yb^{3+}$, Tm^{3+} nanoparticles, *Nanoscale*, **2013**, 5(17), 8084.

41   M. Hu, D. Ma, Y. Cheng, C. Liu, Z. Zhang, Y. Cai, S. Wu and R. Wang, Synergistically enhanced upconversion luminescence in Li^+-doped core–shell-structured ultrasmall nanoprobes for dual-mode deep tissue fluorescence/CT imaging, *J. Mater. Chem. B*, **2017**, 5(14), 2662.

42   H. Li, Q. Huang, Y. Wang, K. Chen, J. Xie, Y. Pan, H. Su, X. Xie, L. Huang and W. Huang, Sc^{3+}-induced morphology, phase structure, and upconversion luminescence evolution of $YF_3:Yb/Er$ nanocrystals, *J. Mater. Chem. C*, **2017**, 5(26), 6450.

43   Z. Huang, H. Gao and Y. Mao, Understanding the effect of Mn^{2+} on Yb^{3+}/Er^{3+} upconversion and obtaining a maximum upconversion fluorescence enhancement in inert-core/active-shell/inert-shell structures, *RSC Adv.*, **2016**, 6(86), 83321.

44   Y. Hu, X. Liang, Y. Wang, E. Liu, X. Hu and J. Fan, Enhancement of the red upconversion luminescence in $NaYF_4:Yb^{3+}$, Er^{3+} nanoparticles by the transition metal ions doping, *Ceram. Int.*, **2015**, 41(10), 14545.

45   M. K. G. Jayakumar, N. M. Idris, K. Huang and Y. Zhang, A paradigm shift in the excitation wavelength of upconversion nanoparticles, *Nanoscale*, **2014**, 6, 8441–8443.

46   W. Zou, C. Visser, J. A. Maduro, M. S. Pshenichnikov and J. C. Hummelen, Broadband dye-sensitized upconversion of near-infrared light, *Nature Photon.*, **2012**, 6, 560–564.

47   G. Chen, W. Shao, R. R. Valiev, T. Y. Ohulchanskyy, G. S. He, H. Ågren and P. N. Prasad, Efficient Broadband Upconversion of Near-Infrared Light in Dye-Sensitized Core/Shell Nanocrystals, *Adv. Opt. Mat.*, **2016**, 4(11), 1760.

48   Y.-F. Wang, G.-Y. Liu, L.-D. Sun, J.-W. Xiao, J.-C. Zhou and C.-H. Yan, Nd^{3+}-Sensitized Upconversion Nanophosphors: Efficient In Vivo Bioimaging Probes with Minimized Heating Effect, *ACS Nano*, **2013**, 7(8), 7200.

49   X. Huang and J. Lin, Active-core/active-shell nanostructured design: an effective strategy to enhance Nd^{3+}/Yb^{3+} cascade sensitized upconversion luminescence in lanthanide-doped nanoparticles, *J. Mater. Chem. C*, **2015**, 3, 7652–7657.

50   S. F. Himmelstoß, L. M. Wiesholler, M. Buchner, V. Muhr, S. Märkl, A. J. Baeumner, and T. Hirsch. 980 nm and 808 nm excitable upconversion nanoparticles for the detection of enzyme-related reactions. *Proc. SPIE* **2017**, 100770L.

51   K. Green, J. Wirth and S. F. Lim, Optical investigation of gold shell enhanced 25 nm diameter upconverted fluorescence emission, *Nanotechnology*, **2016**, 27, 135201.

52   A. L. Feng, M. L. You, L. Tian, S. Singamaneni, M. Liu, Z. Duan, T. J. Lu, F. Xu and M. Lin, Distance-dependent plasmon-enhanced fluorescence of upconversion nanoparticles using polyelectrolyte multilayers as tunable spacers, *Sci. Rep.*, **2015**, 5, 7779.

53   Q. Zhan, X. Zhang, Y. Zhao, J. Liu and S. He, Tens of thousands-fold upconversion luminescence enhancement induced by a single gold nanorod, *Laser Photonics Rev.*, **2015**, 9, 479–487.

2 MOTIVATIONS AND OBJECTIVES

Lanthanide doped nanoparticles/nanomaterials have several outstanding optical properties, which have been identified. The aim of this work was to implement their unique properties in (bio)analytical applications. Assay, theranostic or sensing applications demands specific optical and structural properties of the applied particles. However, one overall basic requirement is the full characterization of the lanthanide nanoparticles regarding size distribution, crystallinity, doping ratios and optical properties.

In general, for optical assays or luminescent probes high quantum yields, fast signal responses, selectivity and reproducibility are favored properties. $GdVO_4$ nanoparticles doped with europium are known for their high quantum yields due to the efficient charge transfer process from the vanadate groups and their large *Stokes* shifted emission. Hydrogen peroxide is an efficient quencher for several europium complexes. Since dynamic quenching of luminescence has rate constants in the time range of diffusion constant, fast signal responses are obtained without changes of the probe. The objective was to investigate the suitability of the europium nanoparticles for the detection of H_2O_2 and to monitor enzyme coupled reactions producing H_2O_2.

For theranostic applications of lanthanide doped nanoparticles additionally requirements like biocompatibility, cellular uptake, high tissue penetration of the inserted light source, low background luminescence caused by the tissue and colloidal stability of the nanoparticles in aqueous solutions are necessary. Here, upconverting nanoparticles have the benefit to generate light directly inside in biological tissue with minimized background luminescence due to their near infrared excitation. Accordingly, their desired application includes imaging, drug delivery or photodynamic therapy which requires the surface functionalization of the nanoparticles. Either the nanoparticles have to be transferred first from the organic phase into the aqueous phase, or the already dispersed particles must be functionalized. Key parameters after the surface modification are the colloidal stability in aqueous solutions of different ionic strengths and the prevention of cross-linking of the nanoparticles. Based on the later application the thickness and the morphology of the new surface layer have to be adapted. For example, for delivery systems thick mesoporous structures are favorable for high drug loading capacities, however for FRET based energy transfer systems the distance between the emitting ions of the nanocrystals and the acceptor molecule should be as small as possible.

Upconverting nanoparticles are used in photodynamic therapy as carriers for the photosensitizer and to shift the excitation wavelength of the photosensitizer. The aim is to indirectly excite the singlet oxygen producing dyes with near infrared light by energy transfer from the upconverting nanoparticles for applications in deeper tissues. Therefore, several aspects have to be considered. First of all, the size of the particles plays a significant role in the cellular uptake and therefore also in the efficiency of the photodynamic therapy. Since the brightness increases with the size of the nanoparticles, but cellular uptake favors small particles, the aim is to synthesize small and bright nanoparticles. Secondly a suitable photosensitizer has to be chosen, which can produce reactive oxygen species and has an overlap of its main absorption with an emission of the UCNPs. In the next step the surface of the nanoparticles has to be modified to bind the photosensitizer, provide colloidal stability and cell permeability. The challenge is to bind as many as possible photosensitizers close to the surface with respect to the colloidal stability, since the efficiency of the energy transfer decrease in the order of six with the distance of the photosensitizer to the activator ions. In a last step the theranostic approach has to be proven by cell toxicity tests of cells incubated with the functionalized nanoparticles.

For sensing applications fast and stable signal responses are afforded from a device. Regarding luminescent sensor application photobleaching and light scattering are major drawback of commercial light emitting materials like organic dyes. Lanthanide doped nanoparticles are resistant to photobleaching due their inorganic design, however light scattering on rough or spongy like surfaces limits their application. On the other side dense nanofiber networks for example would generate extremely high surface-to-volume ratios, which are advantageous for sensors for lower of detection limits. Upconverting nanoparticles with their large anti-*Stokes* shifted emissions (over 300 nm) offer the opportunities for luminescent based sensing devices with dense nanofibermats. The aim was to generate visible light directly inside a sample by entrapping UCNPs inside nanofibers. Finally, for building a sensing device, nanofibermats have to be incoperated into a microfluidic system enabling luminescent online monitoring. The entrapment of the nanoparticles should negotiate time consuming surface modifications or centrifugation steps to achieve colloidal stability in solutions with different ionic strength or pH values. The well separated emission bands of upconverting nanoparticles are investigated regarding possible ratiometric measurements.

3 EUROPIUM-DOPED GDVO$_4$ NANOCRYSTALS AS A LUMINESCENT PROBE FOR HYDROGEN PEROXIDE AND FOR ENZYMATIC SENSING OF GLUCOSE

3.1 Abstract

The authors describe the preparation of Eu^{3+}-doped $GdVO_4$ nanocrystals (NCs) by precipitation of the Gd^{3+} (Eu^{3+})-citrate complex which was then converted to the respective vanadate by dialysis. The fractions of Eu^{3+} ranged from 5 to 100 mol%. The NCs were characterized by XRD, TEM, ICP-OES and dynamic light scattering which revealed that they possess superior colloidal stability in aqueous solutions in that no precipitation can be observed even after several months. The NCs display red and largely red-shifted fluorescence (peaking at 618 nm) on photoexcitation at around 300 nm. Fluorescence is strongly quenched by hydrogen peroxide. It is also shown that the fraction of doping with Eu^{3+} strongly affects quenchability. Most efficient quenching by H_2O_2 is observed if the NCs are doped with 50% of Eu^{3+}. The findings were exploited to develop a fluorometric assay for H_2O_2 that works in the 5 to 250 µM concentration range, with a limit of detection as low as 1.6 µM (at a signal-to-noise ratio of 3). The probe was further employed to design a highly sensitive enzymatic assay for glucose via measurement of the quantity of H_2O_2 formed as a result of the catalytic action of glucose oxidase.
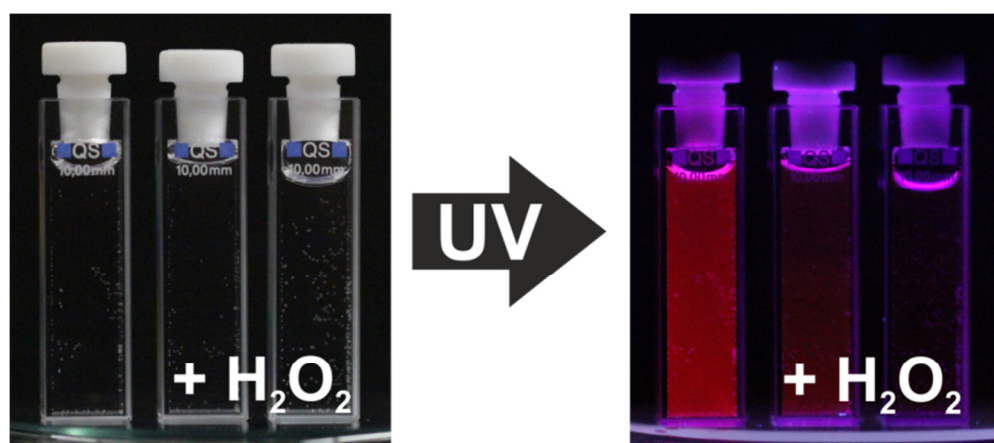
Figure 3.1‖ GdVO$_4$ nanocrystals doped with Eu(III) ions display strong red luminescence which is efficiently quenched by hydrogen peroxide. The NCs therefore are a viable probe for detection of H_2O_2 which often is formed by enzymatic action such as by glucose oxidase.

This chapter has been published.

Verena Muhr, Markus Buchner, Thomas Hirsch, Dragana J. Jovanović, Slobodan D. Dolic, Miroslav D. Dramićanin, Otto S. Wolfbeis

Author contributions

MB and VM wrote the manuscript, designed the figures and performed all optical, ICP-OES and DLS measurements for the sensing application. DJ and SD synthesized the nanocrystals and characterized them by XRD, quantum yield and TEM. The work was designed and supervised by TH, MD and OW (corresponding author).

3.2 Introduction

Vanadates of rare earths (such as $GdVO_4$, YVO_4 and $LuVO_4$) are known to display strong luminescence.[1] Among these, $GdVO_4$ and its co-doped congeners possess distinctly higher absorption cross sections than e.g. YVO_4 and therefore are brighter (brightness being defined as the product of molar absorbance and quantum yield; $\varepsilon \cdot \phi$). $GdVO_4$ can be easily doped with other luminescent lanthanide ions because of the equal valence and similar ionic radii. Such "doped" vanadates can be efficiently excited because of the strong absorption of the vanadate groups and the efficient energy transfer that occurs from $GdVO_4$ to the lanthanide dopand. Doped $GdVO_4$ materials have been used as phosphors (for example after doping with Eu^{3+}, Dy^{3+}, Sm^{3+}), as upconverters with a range of emission colors (after doping with Er^{3+}/Yb^{3+}, Ho^{3+}/Yb^{3+}, or Tm^{3+}/Yb^{3+}), and a lasing material (doped with Nd^{3+}).[2,3] In addition, $GdVO_4$ nanoparticles (NPs) can act as T1-positive contrast agents for magnetic resonance imaging, because Gd^{3+}ions possess unpaired electrons that efficiently alter the relaxation time of the surrounding water protons.[4,5] Hence, such materials may be used for multimodal imaging. It is also noted that $GdVO_4$ nanoparticles doped with Eu^{3+}or Er^{3+}/Yb^{3+} display a strongly temperature-dependent fluorescence.[6] It is generally observed that the fluorescence of lanthanide probes is strongly temperature-dependent. Hydrogen peroxide (H_2O_2, HP) is a product of the enzymatic action of all enzymes out of the class of oxidases, and also is a "natural" contaminant in rainwater. It is being produced industrially in large quantity because it is a useful additive to various commodity products including toothpastes and household chemicals, a precursor and a decomposition product of the explosive triacetone triperoxide, a rocket propellant, and a widely used industrial chemical for purposes such as pulp- and paper-bleaching, in waste water treatment via the Fenton reaction, in odor reduction by virtue of its power to oxidize thiols, in the sterilization of surfaces and medical tools, as a safe antimicrobial (with better activity against Gram-positive bacteria), as a hair bleach (along with ammonia), and in chemiluminescence based cold light sticks. Hence, there is a substantial interest in methods for quantifying HP under various circumstances. Electrochemical [7,8] and optical [9,10] detection schemes, but also chromatographic methods (for discontinuous assays), are by far most often used to determine H_2O_2. Sensors for H_2O_2 may be enzymatic (mainly using a peroxidase as the enzyme) [11,12] or non-enzymatic (via direct electroreduction of H_2O_2).[13,14] All have their respective merits. In electrochemical sensing, the trend is towards methods working at low potential, this rendering them less prone to interferences by other electroactive species.[15] Demchenko has summarized the various kinds of metal nanoparticles capable of fluorometric sensing and imaging of chemical species including H_2O_2.[16] A useful review on metal and metal ion-based nanomaterials for use in optical

probing of H_2O_2 has been presented by Burmistrova et al..[17] Various kinds of fluorescent carbonaceous nanomaterials also may be used,[18] but small molecular chromogenic and fluorogenic molecular probes are in most common.[19] In addition to enzymatic optical assays, enzyme mimics such as $AgVO_3$ nanobelts may be employed,[20] which catalyze the oxidation of tetramethylbenzidine by H_2O_2 to irreversibly form a blue dye. However, direct sensing schemes are preferred, and several ones are known that are exploiting the capability of H_2O_2 to dynamically or statically quench fluorescence. Examples for fluorescent probes include the Eu^{3+}-complex of the antibiotic tetracycline[21] and certain Eu^{3+}-based core/shell nanoparticles which are particularly sensitive.[22] In both single shot detection and in continuous sensing of H_2O_2,[23,24] the trend is towards methods working at long wavelengths, as this makes methods less prone to interferences by backgrounds absorbance and fluorescence of samples, which is particularly strong in case of biomatter. In this contribution, we describe the preparation of aqueous solutions of Eu^{3+}-doped $GdVO_4$ nanoparticles, their structural and morphological properties, and long-term stability of the solution. Then we describe in detail fluorescence of NC's and fluorescence quenching by H_2O_2. We also show that such nanoparticles are viable probes for H_2O_2 and that they also may be employed as transducers in enzymatic reactions accompanied by the formation (and possibly also the consumption) of H_2O_2.

3.3 Experimental

Chemical and reagents

Ammonium vanadate (NH_4VO_3; min. 99.0%, Alfa Aesar), trisodium citrate dehydrate ($Na_3C_6H_5O_7$; 99%, Sigma Aldrich), gadolinium(III) nitrate hexahydrate [$Gd(NO_3)_3$*$6H_2O$; 99.9%, Alfa Aesar] and europium(III) nitrate hexahydrate [$Eu(NO_3)_3$*$6H_2O$; 99.9%, Alfa Aesar] were used without further purification. Rhodamine B (Sigma-Aldrich) was used as a standard for the determination of quantum yields.

Synthesis of colloidal Eu^{3+}-doped $GdVO_4$ nanoparticles

The colloidal Eu^{3+}-doped $GdVO_4$ NCs were synthesized by analogy to the method presented in our previous papers.[25,26] In brief, 30 mL 0.05 M solution of trisodium citrate was added drop by drop to the mixture of 0.05 M solution of $Gd(NO_3)_3$ and $Eu(NO_3)_3$ (40 mL) in stoichiometric ratio (solutions were mixed in concentration of 5; 10; 25; 50 and 100 mol% Eu^{3+} with respect to Gd^{3+} ions) at room temperature. A white precipitate consisting of the Gd^{3+}(Eu^{3+})-Cit3−complex is formed. After vigorous stirring for 30 min, the white precipitate is completely dissolved by the addition, drop by drop, 30 mL of a 0.05 M

solution of NH_4VO_3 (dissolved in 0.15 M NaOH solution). A transparent solution is obtained that has a pH value of about 8. It is subsequently heated and stirred at 60 °C for 60 min. Finally, the colloidal solution is cooled down to room temperature. Slow growth of particles was accomplished by dialysis against distilled water for 24 h to remove the excess ions. Dialysis was terminated once the pH value had reached 7.0 so that such solutions can be used along with buffers of physiological pH values. Powder samples for structural characterization were obtained by evaporation of aqueous colloidal solutions. No signs of precipitation of particles has been evidenced over the period of several months, which confirmed the superior colloidal stability of Eu^{3+}-doped $GdVO_4$ NCs in aqueous solution.

Instrumentation

Powder X-ray diffraction (XRD) measurements were performed on a Rigaku SmartLab diffractometer using Cu-K$_{\alpha 1,2}$ radiation (λ = 0.15405 nm). Diffraction data were recorded with a step size of 0.02° and a counting time of 0.7 min^{-1} over the 2θ-range of 10° to 100°. Transmission electron microscopy (TEM) studies were made on a Tecnai G20 (FEI) operated at an accelerating voltage of 200 kV. Luminescence measurements were performed with an Aminco-Bowman Series 2 fluorescence spectrometer (band pass 4 nm), and Fluorolog-3 Model FL3-221 spectrofluorometer system (Horiba JobinYvon), was used for the determination of quantum yields. Absorption spectra were measured with a Shimadzu UV-2600 spectrophotometer (Shimadzu Corporation, Tokyo, Japan) equipped with an integrated sphere (ISR-2600 Plus (for UV-2600)) in the 220–700 nm range with 1 nm step. Dynamic light scattering (DLS) and zeta-potential measurements were conducted on a Malvern Zetasizer nano ZS (www.malvern.com). The determination of the Eu^{3+} content in the particles was performed on an inductively coupled plasma optical emission spectrometer (ICP-OES) from Spectro (www.spectro.com).

Determination of quantum yields (QYs)

For the determination of quantum yields room-temperature absorption (from 250 to 700 nm) and emission spectra (330 nm excitation, emission from 500 to 750 nm) of aqueous of NCs and Rhodamine B (reference, 10^{-6} mol dm^{-3}) were measured. QYs were calculated from the following expression:[27]

$$QY = QY_R \times \left(\frac{A_R}{I_R}\right) \times \left(\frac{I}{A}\right) \times \left(\frac{n^2}{n_R^2}\right)$$

where R refers to the reference (QY_R = 0.31),[28] I is the integrated emission intensity, A is the optical density, and n is the refractive index of the solvent (in both cases water,

n = 1.33). In order to minimize re-absorption effects, concentrations of NCs and Rhodamine B in solution were chosen to maintain optical density between 0.01 and 0.1 at 330 nm.

Quenching of fluorescence by H_2O_2

The effect of the fraction of Eu^{3+} in the NCs was studied by dispersing the various NCs in TRIS buffer (50 mM, pH 7.4) at a total Eu^{3+} concentration of 0.4 mM each. A solution of H_2O_2 (c = 0.1 M) was added to each cuvette to adjust the total concentrations of H_2O_2 to between 5 and 500 M. The total volume of each sample was 2 mL. The emission of the particles was recorded at 618 nm. The excitation wavelength was adjusted according to the excitation maximum of the different particles (**Figure 3.4**).

Selectivity studies

These were performed in the following way: $EuVO_4$ nanoparticles (containing 0.4 mM of Eu^{3+}) and quencher (100 M) were added to TRIS buffer (50 mM, pH 7.4) to yield a total volume of 2 mL. After mixing and incubating for 5 min, the emission intensity at 618 nm was recorded under photoexcitation at 295 nm. The data given are averages of three measurements.

Fluorometric determination of hydrogen peroxide

Time traces of the luminescence of $GdVO_4$(50%Eu) nanoparticles under 298/618 nm excitation/emission were acquired by dispersing the particles in 2 mL TRIS buffer of pH 7.4 and adding, after every 5 min 50 nmol of H_2O_2 (equivalent to 1 μL of a H_2O_2 standard solution) to the colloidal dispersion of the particles. The drop in luminescence intensity was recorded over the course of four addition steps.

Enzymatic determination of glucose

Time trace measurements of the luminescence under the same experimental conditions as above were performed were performed by adding glucose oxidase (149.8 kU g^{-1}; in a concentration of 2.3 mg mL^{-1} in TRIS buffer) to the nanoparticles dispersed in 2 mL of TRIS buffer of pH 7.4. Every five minutes 50 nmol glucose (equivalent to 1 μL glucose solution) was added to a dispersion of the particles containing a total Eu^{3+} concentration of 0.4 mM. The drop of the luminescence intensity was recorded over the course of four addition steps.

Determination of glucose in serum

Glucose in fetal bovine serum was determined by the standard addition method. The sample was diluted by a factor of 1/80 by addition of 25 µL of serum to an aqueous solution containing 2.0 mg mL^{-1} of glucose oxidase (=149.8 kU g^{-1}) and 0.4 mM Eu^{3+} in the form of GdVO$_4$(50%Eu) particles. This sample was spiked with glucose to give final concentrations between 20 µM and 120 µM. The samples were incubated at room temperature for 5 min and fluorescence was measured at 618 nm under 298 nm excitation. The glucose concentrations of samples were also determined using a commercial glucose meter (Contour Next; Bayer, https://www.contournext.com).

3.4 Results and Discussion

3.4.1 Characterization of the GdVO$_4$:Eu Nanocrystals

Synthesis of the NCs follows a simple but well reproducible strategy that results in good yields ($\sim$ 6 mg of NCs in 1 mL of solution). The NCs were submitted to XRD analysis. **Figure 3.2** shows are presentative XRD pattern for GdVO$_4$:Eu NCs (with 50 mol%). The pattern shows the presence of a single tetragonal zircon-type phase of GdVO$_4$ (space group I41/amd, ICDD card no. 01-086-0996). The absence of impurity phases and very small shift of reflections compared to the reflection positions of pure GdVO$_4$ indicate that the Eu^{3+} ions are successfully and uniformly incorporated into the GdVO$_4$ host lattice. In addition, the relatively intense reflection peaks suggest that the NCs are highly crystalline, and no additional thermal treatment is necessary.
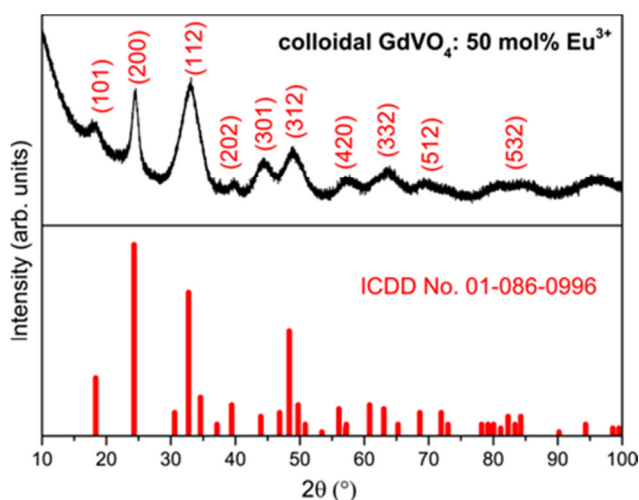
Figure 3.2‖ XRD pattern (without background correction) for GdVO$_4$ nanocrystals doped with 50 mol% of Eu^{3+} (upper graph), the main diffraction peaks are indexed according to ICCD No. 011-086-0996 card (lower graph).

Table 3.1 ‖ Parameters of the crystal structure of GdVO$_4$ nanocrystals doped with 50 mol% Eu^{3+}obtained by Rietveld refinement of experimental data.

Parameters	GdVO$_4$:50 mol% Eu^{3+}
a = b (nm)	0.7292(5)
c (nm)	0.6384(5)
Crystallite size (nm)	2.146(3)
strain	1.2(10)
Goodness of fit (GOF)	2.7546
Rietveld profile factor (Rp)	2.18%

The crystal lattice parameters given in **Table 3.1** were obtained after Rietveld fitting of the experimental data. The average crystallite size for GdVO$_4$:50 mol% Eu^{3+} was 2.1 nm.

The representative transmission electron microscopy image of Eu^{3+} GdVO$_4$ NCs is given in **Figure 3.3A** and the size distribution histogram of particles is presented in **Figure 3.3B**. Electron microscopy analysis showed that colloid consists of ultra-small NCs of about 2.7 nm in diameter. NCs of such dimensions have large surface to volume ratio, therefore, a large number of Eu^{3+} dopant ions are located in the vicinity or at the surface. For this reason, Eu^{3+} fluorescence is strongly affected by the surroundings of NCs. Zeta-potentials were determined in solutions of pH 6. The particles possess average zeta potentials between −22 mV in case of 100% Eu and −33 mV at 5% of Eu^{3+}, indicating their excellent colloidal stability due to the electrostatic stabilization by citrate as surface ligand. An increase in the fraction of Eu^{3+} ions causes the zeta potential to drop (which, however, always remains larger than −20 mV), possibly because of the smaller particle size. The excellent colloidal stability is underpinned by the observation that particle agglomeration cannot be detected by DLS or visually even after several months of storage of aqueous solutions. This is con-firmed by the dynamic light scattering data shown in **Figure 3.3C** which also gives mean hydrodynamic diameters and the corresponding polydispersity indices (PdI). The slight increase in size is interpreted in terms of a slight distortion the crystal lattice which affects crystal growth. The largest change can thus be seen in the lattice made from pure EuVO$_4$ lattice.
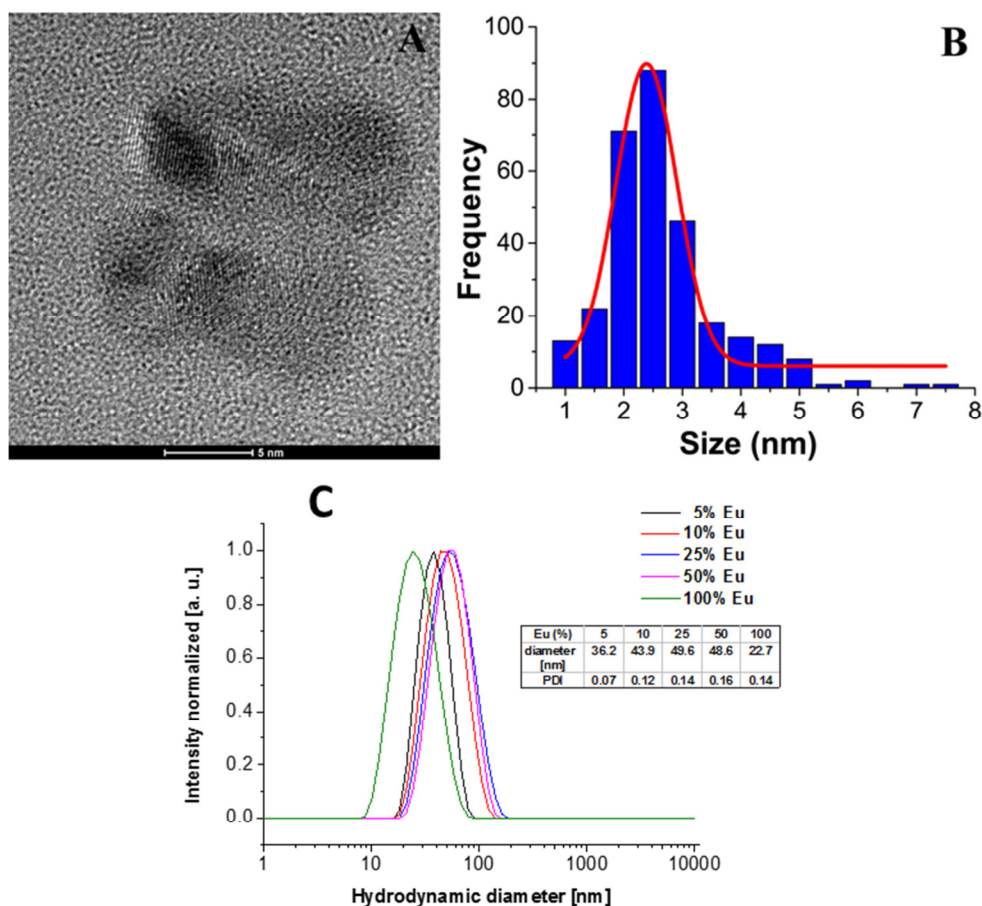
Figure 3.3‖ A) TEM image (the bar on the bottom symbolizes a length of 5 nm) and (**B**) size histogram of GdVO$_4$ nanocrystals doped with 50% Eu^{3+}.**C**) Intensity-weighed dynamic light scattering measurements of citrate-capped, Eu^{3+}-doped GdVO$_4$ nanoparticles in TRIS buffer (50 mM, pH 7.4). The table gives the mean hydrodynamic diameters and the corresponding polydispersity indices (PdI) depending on the Eu^{3+} content. Percentages refer to the theoretical percentages as given in **Table 3.2**.

In order to compare calculated doping parameters (% doping according to the fractions of ions employed) to true doping in the NCs finally obtained, the particles were analyzed for their content of Gd^{3+} and Eu^{3+} ions by ICP-OES. **Table 3.2** summarizes the results and shows that the calculated fractions of Eu^{3+} in the NCs sometimes are quite different from the experimental values. In the rest of this article, the NCs are specified by their calculated fraction of Eu^{3+}. **Table 3.2** also presents quantum yields of NCs for different Eu^{3+} concentrations.

Table 3.2 ‖ Comparison of the theoretical and real Eu^{3+} fraction in the $GdVO_4$ nanoparticles determined by ICP-OES, and respective quantum yields in aqueous colloidal solution.

calculated fraction of Eu^{3+} [%]	real content of Eu^{3+} [%]	quantum yield [%]
5	7	18.3
10	14	22.1
25	32	15.2
50	58	14.7
100 [a]	100	n.d.

The NCs display strong red fluorescence if excited at around 300 nm. The excitation peak wavelength depends on the Eu^{3+} content in the NCs (**Figure 3.4A**). On increasing the fraction of Eu^{3+}, the main excitation peak is blue shifted from 325 nm to 295 nm. The emission band has the typical narrow shape of Eu^{3+}−based emitters and peaks at 618 nm which corresponds to the $^5D_0 \rightarrow {}^7F_2$ transition (**Figure 3.4B**). Particles containing 25 mol% Eu^{3+} show the highest overall luminescence intensity when compared to the other compositions (all adjusted to the same total Eu^{3+} concentration of 0.4 mM). This can be interpreted by the occurrence of two effects: First, the emission intensity increases on account of the larger number of emission centers. However, an opposite effect simultaneously occurs since optically excited rare earth doped materials suffer from concentration quenching. When excitation energy is transferred between many ions in the time required for the radiative decay, the probability of non-radiative deexcitation is strongly increased. The energy transfer probability increases with decreasing distance between dopant ions (a result of increasing their concentration), and this results in decreased emission intensity at high dopant concentrations. The optimal dopant concentration depends on the kind of rare-earth ion and the properties of the host material, and therefore has to be independently optimized for each dopant-host combination.
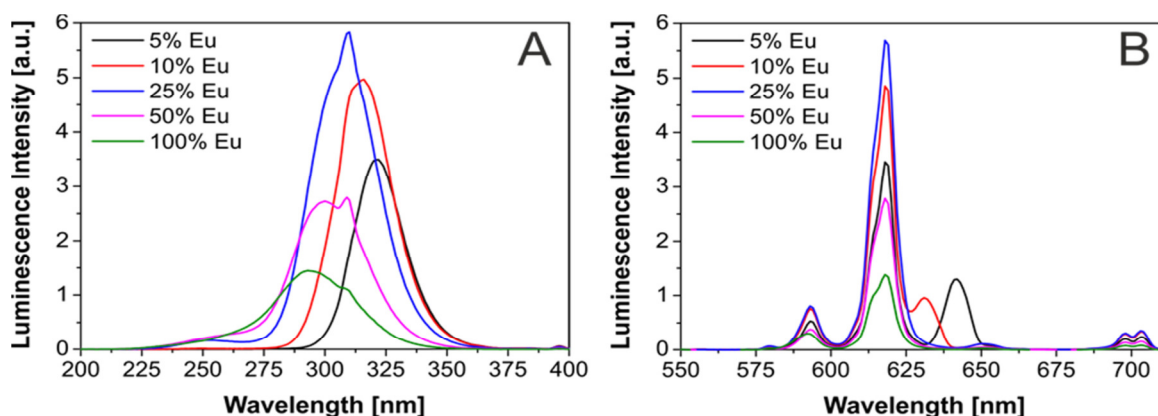
Figure 3.4‖ A) Excitation and (**B**) emission spectra of GdVO$_4$(x% Eu^{3+}) nanoparticles in TRIS buffer (50 mM, pH 7.4). The Eu^{3+} concentration in all samples was 0.4 mM. Emission spectra were recorded under photoexcitation at the maximum of the respective excitation spectrum, i.e. $\lambda_{exc,5\%}$ at 325 nm, $\lambda_{exc,10\%}$ at 316 nm, $\lambda_{exc,25\%}$ at 310 nm, $\lambda_{exc,50\%}$ at 298 nm, and $\lambda_{exc,100\%}$ at 295 nm.

3.4.2 Eu^{3+}-doped GdVO$_4$ Nanocrystals as a Fluorescent Probe for Determination of Hydrogen Peroxide

Optimization of the fraction of the Eu^{3+}dopant

Based on the spectral characterization, an Eu^{3+} fraction of 10% yields the highest quantum yield. However, the Eu^{3+} concentration on the surface of the particles should affect the quenching efficiency. It was found that the fraction of dopant (Eu^{3+}) exerts a distinct effect on the quenchability by H$_2$O$_2$ as shown in **Figure 3.5**. While particles doped with up to 25% Eu^{3+} show a negligible sensitivity against H$_2$O$_2$ in concentrations below 100 µM, those containing 50% and 100% Eu^{3+} display high sensitivity and are quenched by H$_2$O$_2$ in concentrations as low as 5 µM. Based on the stronger overall luminescence intensity (**Figure 3.4**) and wider analytical range of GdVO$_4$(50%Eu), the following experiments were performed using these particles.
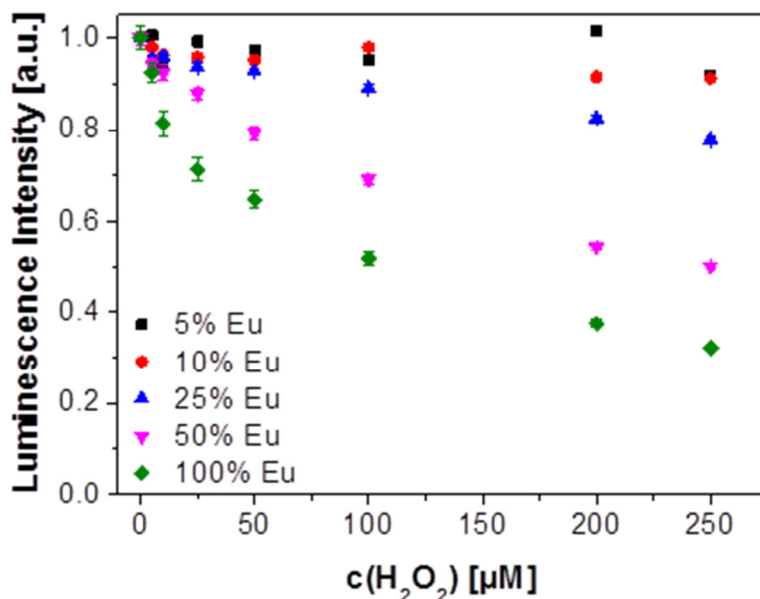
Figure 3.5 ‖ Quenching of the (normalized) luminescence of Eu^{3+}-doped $GdVO_4$ nanoparticles (λ_{exc} = 298 nm, λ_{em} = 618 nm; pH 7.4) by H_2O_2 as a function of the % fraction of Eu^{3+} dopand. The total concentration of Eu^{3+} always was adjusted to 0.4 mM.

Stern-Volmer kinetics

H_2O_2 was found to act as a strong quencher of the fluorescence of the NPs. **Figure 3.6** shows a Stern-Volmer plot of the quenching of NCs doped with 50% Eu^{3+}. It is linear in the 5 to 250 µM concentration range (with an R^2 value of 0.993; for n = 3), but later levels off, probably due to quenching effects other than dynamic quenching. The respective quenching constant (calculated from the initial slope) is 5.4 mM^{-1}. The limit of detection (at a signal-to-noise ratio of 3) is 1.6 µM H_2O_2.
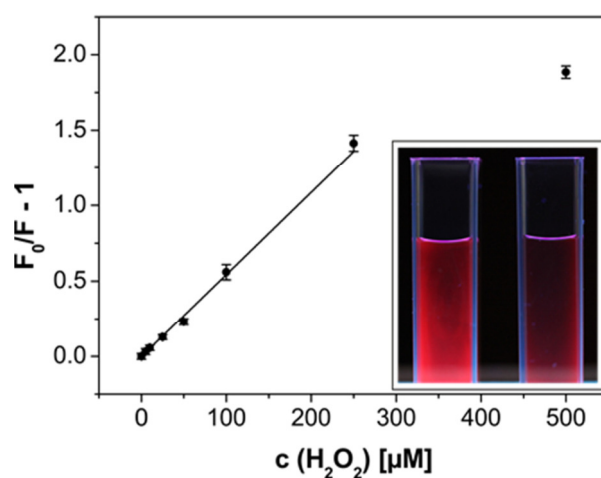
Figure 3.6 ‖ Stern-Volmer plot for the quenching of the emission (λ_{exc} = 298 nm, λ_{em} = 618 nm) of $GdVO_4$(50%Eu) nanoparticles by hydrogen peroxide at pH 7.4. The concentration of Eu^{3+} is 0.4 mM. The inset shows a digital photograph of a dispersion of $GdVO_4$(50%Eu) nanoparticles in water before and after the addition of H_2O_2. The decrease of the luminescence intensity in presence of H_2O_2 is clearly visible.

Interference study

In order to test the selectivity for H_2O_2, several potentially interfering ions were also tested with respect to quenching. **Figure 3.7** shows that metal ions commonly encountered in physiology (such as Ca^{2+}, Zn^{2+}, Mg^{2+}) do not cause an effect on fluorescence intensity. However, Cu^{2+} and Fe^{3+} quench with an efficiency even higher than that of H_2O_2. It is noted, however, at this point that these species rarely occur in species where H_2O_2 is to be determined, and if so, their concentration does not change over time. In fact, Fe^{2+} would be quickly oxidized to Fe^{3+} by H_2O_2. Alternatively, Cu^{2+} may be complexed by EDTA or any other strong complexing agent. We therefore conclude that $GdVO_4(50\%Eu)$ is a quite sensitive probe for H_2O_2 that compares well to other NP-based fluorescent probes for H_2O_2 as can be seen in **Table 3.3**.
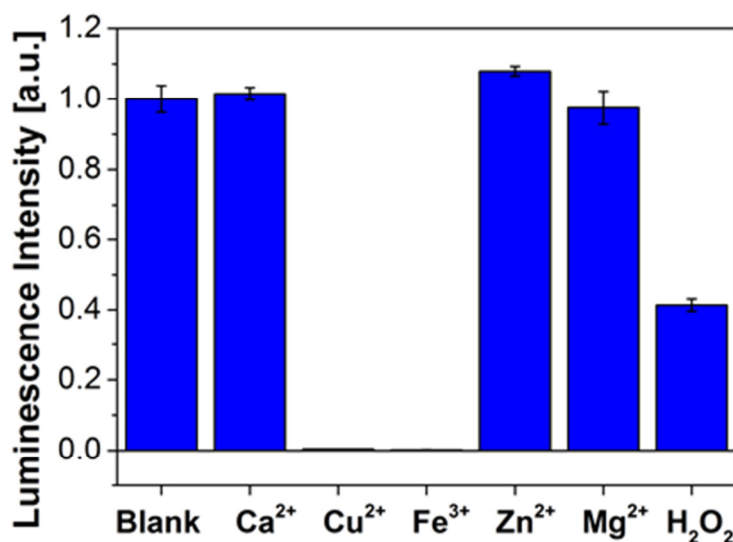
Figure 3.7 ‖ Interference study of Eu^{3+} doped $GdVO_4$ nanoparticles against physiologically relevant metal ions performed in TRIS buffer (pH 7.4). The total Eu^{3+} concentration was 0.4 mM in all samples. The luminescence intensities were normalized to a "blank" not containing any quencher. The concentration of all quenchers was adjusted to 100 µM.

Europium-Doped GdVO4 Nanocrystals as a Luminescent Probe for Hydrogen Peroxide and for Enzymatic Sensing of Glucose

Table 3.1 ‖ Figures of merit of nanomaterial based optical probes and sensors for the detection of hydrogen peroxide, and respective limits of detection (LODs).

Material	Method	Limit of detection	Ref.
Fe_3O_4 NPs on graphene oxide acting as enzyme mimic	Chromogenic reaction; photometry at 550 nm.	40 nM	29
Gold nanodots	Quenching of luminescence.	30 nM	30
Gold nanoclusters	Fluorescence resonance energy transfer.	0.5 pM	31
Cu^{2+}/CeO_2 nanocomposite with peroxidase-like activity	Chromogenic reaction. photometry.	50 µM	32
Carbon nanotube composite with peroxidase	Fluorogenic reaction.	1.2 µM	33
Luminescent ZnO nanoparticles.	Quenching of luminescence.	10 mM	34
$NaYF_4$:Yb/Er upconversion nanoparticles and peroxidase	Chromogenic reaction that causes an inner filter effect on the emission of the NPs.	45 nM	35
Carbon nanodots and Fe^{3+} ions	Fluorescence turn-off detection.	25 nM	36
$AgVO_3$ nanobelts with peroxidase-like activity	Chromogenic reaction; photometry at 662 nm.	5 µM	18
Gold nanoparticles	Exploits an inner filter effect.	0.8 µM	37
Poly(N-isopropylacrylamide)-co-(acrylic acid) microgel and AgNPs	Colorimetric (absorbance at 400 nm).	0.3 µM	38
Silver nanoparticles	Measures the oxygen formed by catalytic decomposition of H_2O_2 by using the luminescent oxygen probe $Ru(bipy)_3^{2+}$.	150 µM	21

Enzymatic determination of glucose in water

The enzyme glucose oxidase catalyzes the oxidation of glucose by oxygen, and this is accompanied by the formation of H_2O_2. **Figure 3.8A** shows normalized time trace measurements of the luminescence of GdVO4(50%Eu) nanoparticles at 618 nm. After 5, 10, 15 and 20 min 50 nmol H_2O_2 or glucose were added to the nanoparticle dispersion. After each addition a distinct drop in the emission intensity was detected. The signal response was immediate and reached a constant level after 1 min. In case of GOx/glucose the overall signal response was reduced and less stable, as a constant drift to lower intensities was obtained. The drift at the beginning of the measurement already has been explained by other groups.[1] The surface ligands seem to be involved in a complex quenching mechanism, leading to a slow and steady decrease of the luminescence over the course of about 60 min. For both systems a linear behavior between 25 and 100 µM analyte was found in the Stern-Volmer plot (**Figure 3.8B**). The detection limit for glucose is 2.1 µM. The signal changes obtained by the system GOx/glucose were slightly weaker than by the direct approach upon addition of H_2O_2. The measurements showed excellent reproducibility in both cases, resulting in only small signal variations.
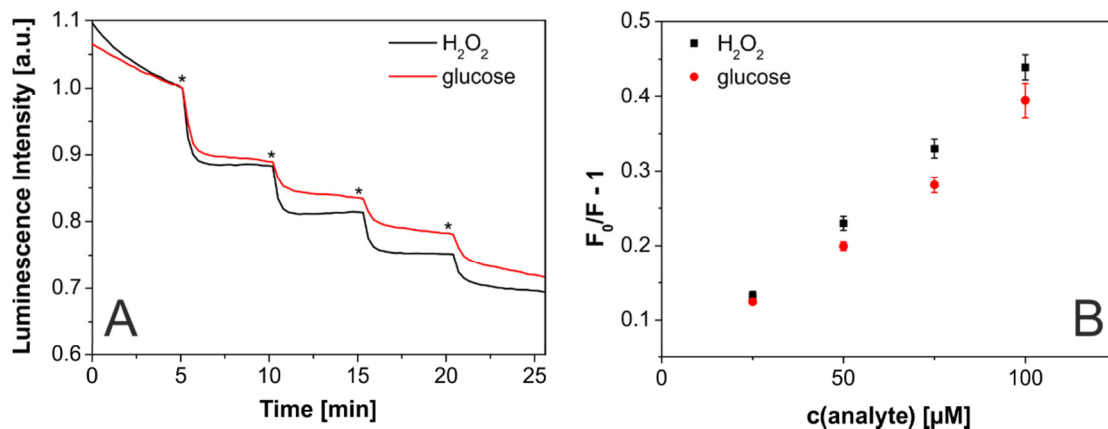
Figure 3.8 ‖ A) Time trace measurements of the luminescence (λ_{exc} = 298 nm, λ_{em} = 618 nm) of GdVO4(50%Eu) nanoparticles at pH 7.4. Every five minutes either 50 nmol H_2O_2(black) or glucose (red) were added to a dispersion of the particles as indicated by the asterisks. For the latter, a glucose oxidase concentration of 2.3 mg mL^{-1} was used. **B**) Stern-Volmer plots of the emission of GdVO4(50%Eu) nanoparticles in the presence of various concentrations of H_2O_2 and glucose.

Enzymatic determination of glucose in serum

The applicability of the GdVO$_4$:Eu nanoparticles for biological samples was proven by determination of glucose in (spiked) fetal bovine serum (www.sigmaaldrich.com/catalog/product/sigma/f0804?lang=de®ion=DE) following an established protocol using the standard addition method. A glucose concentration of 1.96 ± 0.23 mM was determined by the standard addition method (**Figure 3.9**). Control experiments were performed with a commercial glucose meter operating on an electrochemical basis in order to verify the results. The commercial device gave a value of 2.00 ± 0.04 mM, thereby well matching the results obtained with the nanoparticle based method.
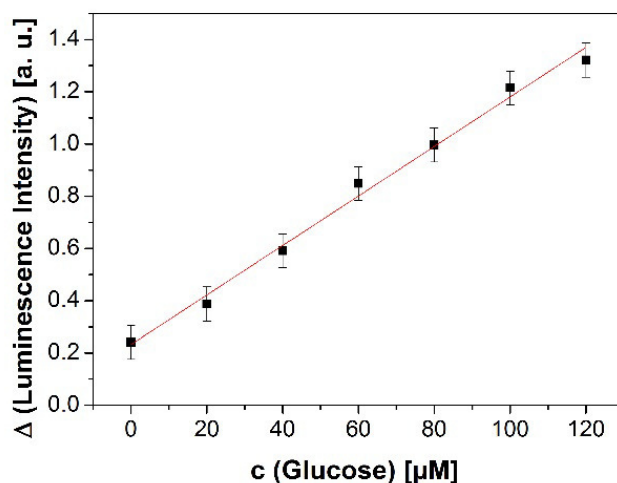
Figure 3.9‖ Determination of glucose concentration in fetal bovine serum by the standard addition method. The diluted serum sample was spiked with glucose in steps of 20 µM and the fluorescence emission (λ_{exc} = 298 nm, λ_{em} = 618 nm) was recorded after an incubation time of 5 min.

3.5 Conclusion

The particles described here possess attractive properties such as a very large *Stokes'* shift (315 nm), narrow emission bands, and relatively good quantum yields. Notably, their fluorescence is strongly quenched by H$_2$O$_2$ and this makes them a viable probe for H$_2$O$_2$. It excels by its low detection limit and its applicability to monitor the kinetics of the oxidation of glucose by glucose oxidases. There is no reason not to assume that the probe also works with other oxidases such as alcohol oxidase or cholesterol oxidase. Due to the sensitivity of the nanoprobe, the limits of detection for glucose are low enough to enable its determination even in interstitial and adipose tissue. Conceivably, the particles

may also be applied in future to monitor the consumption of H_2O_2, for example during oxidations catalyzed by peroxidases which are a widely used label in enzyme linked immuno assays. It is important to mention here that Eu^{3+} doped $GdVO_4$ nanoparticles are ideal candidates for the development of multifunctional materials because they are able to perform polyvalent functions. For example, these nanoparticles may be used for dual sensing since it has been shown that temperature can be measured from the luminescence of Eu^{3+} incorporated into $GdVO_4$.[39,40] In addition, when Gd^{3+} ions are constituents of the host matrix the material exhibits paramagnetic properties and it is able to sense magnetic fields. It has been shown that $GdVO_4$ nanoparticles can act as T1-positive contrast agents for magnetic resonance imaging (MRI), because Gd^{3+} ions possess unpaired electrons that efficiently alter the relaxation time of the surrounding water protons, and that they also provide luminescence imaging and controlled drug release functionalities.[5,6,41]

References

1   N. Duée, C. Ambard, F. Pereira, D. Portehault, B. Viana, K. Vallé, D. Autissier and C.Sanchez, New synthesis strategies for luminescent YVO_4:Eu and $EuVO_4$ nanoparticles with H_2O_2 selective sensing properties, *Chem. Mater.*, **2015**, 27, 5198–5205.

2   N. Shanta Singh, R.S. Ningthoujam, G. Phaomei, S. Singh, A. Dorendrajit and R. K. Vinu Vatsa, Redispersion and film formation of $GdVO_4$: $Ln^{3+}(Ln^{3+}= Dy^{3+}, Eu^{3+}, Sm^{3+}, Tm^{3+})$ nanoparticles: particle size and luminescence studies, *Dalton Trans.*, **2012**, 41, 4404–4412.

3   L. Zhang, C.-Y. Zhang, Z.-Y. Wei, Z.-G. Zhang, S. Strohmaier and H.J. Eichler, Characteristics of Nd:GdVO4 laser with different Nd-doping concentrations, *Chin. Phys. Lett.*, **2006**, 23, 2088–2090.

4   W.M. Yen, S. Shionoya and H. Yamamoto, Phosphor Handbook*, second ed., CRCPress, Boca Raton*, Fl, USA, **2007**.

5   X. Kang, D. Yang, Y. Dai, M. Shang, Z. Cheng, X. Zhang, H. Lian, P. Ma and J. Lin, Poly(acrylic acid) modified lanthanide-doped $GdVO_4$ hollow spheres for upconversion cell imaging, MRI and pH-dependent drug release, *Nanoscale*, **2013**, 5, 253–261.

6   T. V. Gavrilović, D. J. Jovanović, V. Lojpur and M. D. Dramićanin, Multifunctional Eu^{3+}- and Er^{3+}/Yb^{3+}-doped $GdVO_4$ nanoparticles synthesized by reverse micelle method, *Sci. Rep.*, **2014**, 4, 4209.

7   S. Chen, R. Yuan, Y. Chai and F. Hu, Electrochemical sensing of hydrogen peroxide using metal nanoparticles: a review, *Microchim. Acta*, **2013**, 180, 15–32.

8   L. Mei, P. Zhang, J. Chen, D. Chen, Y. Quan, N. Gu, G. Zhang and R. Cui, Non-enzymatic sensing of glucose and hydrogen peroxide using a glassy carbon electrode modified with a nanocomposite consisting of nanoporous copper, carbon black and nafion, *Microchim. Acta*, **2016**, 183, 1359–1365.

9   M. Schäferling, D. B. M. Grögel and S. Schreml, Luminescent probes for detection and imaging of hydrogen peroxide, *Microchim. Acta*, **2011**, 174, 1–18.

10   B. Zhu, H. Jiang, B. Guo, C. Shao, H. Wu, B. Du and Q. Wei, A highly selective ratiometric fluorescent probe for hydrogen peroxide displaying a large emission shift, *Sens. Actuators B Chem.*, **2013**, 186, 681–686.

11   Y. Wang, Z. Wang, Y. Rui and M. Li, Horseradish peroxidase immobilization on carbon nanodots/CoFe layered double hydroxides: direct electrochemistry and hydrogen peroxide sensing, *Biosens. Bioelectron.*, **2015**, 64, 57–62.

12   N. A. Burmistrova, R. J. Meier, S. Schreml and A. Duerkop, Reusable optical sensing microplate for hydrogen peroxide using a fluorescent photoinduced electron transfer probe (HP Green), *Sens. Actuators B Chem.*, **2014**, 193, 799–805.

13   X. Chen, G. Wu, Z. Cai, M. Oyama and X. Chen, Advances in enzyme-free electrochemical sensors for hydrogen peroxide glucose, and uric acid, *Microchim. Acta*, **2014**, 181, 689–705.

14   N. Shehata, E. Samir and S. Gaballah, New optical sensor for peroxides using neodymium doped-ceria nanoparticles via fluorescence quenching technique, *Sens. Actuators B Chem.*, **2016**, 231, 341–348.

15   Y. Li, J. Zheng, Q. Sheng and B. Wang, Synthesis of Ag@AgCl nanoboxes, and their application to electrochemical sensing of hydrogen peroxide at very low potential, *Microchim. Acta*, **2015**, 182, 61–68.

16   A.P. Demchenko, Nanoparticles and nanocomposites for fluorescence sensing and imaging, *Meth. Appl. Fluorescence*, **2013**, 1, 022001.

17   N. Burmistrova, O. Kolontaeva and A. Duerkop, New nanomaterials and luminescent optical sensors for detection of hydrogen peroxide, *Chemosensors*, **2015**, 3, 253–273.

18   A. P. Demchenko, M. O. Dekaliuk, Novel fluorescent carbonic nanomaterials for sensing and imaging, *Meth. Appl. Fluorescence*, **2013**, 1, 042001.

19   X. Li, X. Gao, W. Shi and H. Ma, Design strategies for water-soluble small molecular chromogenic and fluorogenic probes, *Chem. Rev.*, **2014**, 114, 590–659.

20   Z. Xiang, Y. Wang, P. Ju and D. Zhang, Optical determination of hydrogen peroxide by exploiting the peroxidase like activity of $AgVO_3$ nanobelts, *Microchim.Acta*, **2016**, 183, 457–463.

21   O.S. Wolfbeis, A. Dürkop, M. Wu and Z. Lin, A europium-ion-based luminescent sensing probe for hydrogen peroxide, *Angew. Chem. Int. Ed.*, **2002**, 41, 4495–4498.

22   F. Luo, J. Yin, F. Gao and L. Wang, A non-enzyme hydrogen peroxide sensor based on core/shell silica nanoparticles using synchronous fluorescence spectroscopy, *Microchim. Acta*, **2008**, 165, 23–28.

23   H. E. Posch and O.S. Wolfbeis, Optical sensor for hydrogen peroxide, *Microchim. Acta*, **1989**, 97, 41–50.

24   O.S. Wolfbeis, M. Schäferling and A. Dürkop, Reversible optical sensor membrane for hydrogen peroxide using an immobilized fluorescent probe, and ist application to a glucose biosensor, *Microchim. Acta*, **2003**, 143, 221–227.

25   B. del Rosal, A. Pérez-Delgado, M. Misiak, A. Bednarkiewicz, A. S. Vanetsev, Y.Orlovskii, D. J. Jovanovi´c, M. D. Drami´canin, U. Rocha, K. Upendra Kumar, C. Jacinto, E. Navarro, E. Martín Rodríguez, M. Pedroni, A. Speghini, G. A. Hirata, I. R. Martín and D. Jaque, Neodymium-doped nanoparticles for infrared fluorescence bioimaging: the role of the host, *J. Appl. Phys.*, **2015**, 118, 143104.

26   B. del Rosal, A. Pérez-Delgado, E. Carrasco, D. J. Jovanović, M. D. Dramićanin, G. Dražić de la Fuente, Ángeles Juarranz, F. Sanz-Rodriguez and D. Jaque, Neodymium-based stoichiometric ultra small nanoparticles for multifunctional deep-tissue photothermal therapy, *Adv. Opt. Mater.*, **2016**, 4, 782–789.

27   J. Zong, Y. Zhu, X. Yang, J. Shen and C. Li, Synthesis of photoluminescent carbogenic dots using mesoporous silica spheres as nanoreactors, *Chem.Commun.*, **2011**, 47, 764–766.

28   D. Magde, G. E. Rojas and P. G. Seybold, Solvent dependence of the fluorescence lifetimes of xanthene dyes, *Photochem. Photobiol.*, **1999**, 70, 737–744.

29   Q. Chang and H. Tang, Optical determination of glucose and hydrogen peroxide using a nanocomposite prepared from glucose oxidase and magnetite nanoparticles immobilized on graphene oxide, *Microchim. Acta*, **2014**, 181, 527–534.

30   Y.-C. Shiang, C.-C. Huang and H.-T. Chang, Gold nanodot-based luminescent sensor for the detection of hydrogen peroxide and glucose, *Chem. Commun.*, **2009**, 343, 7–343 (9).

31   Q. Zhao, S. Chen, H. Huang, L. Zhang, L. Wang, F. Liu, J. Chen, Y. Zeng and P. K. Chu, Colorimetric and ultra-sensitive fluorescence resonance energy transfer determination of H_2O_2 and glucose by multifunctional Au nanoclusters, *Analyst*, **2014**, 139, 1498–1503.

32   N. Wang, J. Sun, L. Chen, H. Fan and S. Ai, A $Cu_2(OH)_3Cl$-CeO_2 nanocomposite with peroxidase-like activity and its application to the determination of hydrogen peroxide, glucose and cholesterol, *Microchim. Acta*, **2015**, 182, 1733–1738.

33   M. Magyar, K. Hajdu, T. Szabó, B. Endrődi, K. Hernádi, E. Horváth, A. Magrez, L. Forró, C. Visy and L. Nagy, Sensing hydrogen peroxide by carbon nanotube/horseradish peroxidase bio-nanocomposite, *Phys. Status Solidi*, **2013**, 250, 2559–2563.

34   D. Sodzel, V. Khranovskyy, V. Beni, Anthony P. F. Turner, R. Viter, M. O. Eriksson, P.-O. Holtz, J.-M. Janot, M. Bechelany, S. Balme, V. Smyntyna, E. Kolesneva, L. Dubovskaya, I. Volotovski, A. Ubelis and R. Yakimova, Continuous sensing of hydrogen peroxide and glucose via quenching of the UV and visible luminescence of ZnO nanoparticles, *Microchim. Acta*, **2015**, 182, 1819–1826.

35   J. Liu, L. Lu, A. Li, J. Tang, S. Wang, S. Xu and L. Wang, Simultaneous detection of hydrogen peroxide and glucose in human serum with upconversion luminescence, *Biosens. Bioelectron.*, **2015**, 68, 204–209.

36   J. Wei, L. Qiang, J. Ren, X. Ren, F. Tang and X. Meng, Fluorescence turn-off detection of hydrogen peroxide and glucose directly using carbon nanodots as probes, *Anal. Methods*, **2014**, 6, 1922–1927.

37   H.-C. Chang and J.-A. A. Ho, Gold nanocluster-assisted fluorescent detection for hydrogen peroxide and cholesterol based on the inner filter effect of gold nanoparticles, *Anal. Chem.*, **2015**, 87, 10362–10367.

38   D.-M. Han, M. Zhang, Qiang and M. J. Serpe, Poly(N-isopropylacrylamide)-co-(acrylic acid) microgel/Ag nanoparticle hybrids for the colorimetric sensing of H_2O_2, *Nanoscale*, **2015**, 7, 2784–2789.

39   M. González-Béjar, J. Pérez-Prieto, Upconversion luminescent nanoparticles in physical sensing and in monitoring physical processes in biological samples, *Meth. Appl. Fluorescence*, **2015**, 3, 042002.

40   M. G. Nikolić, D.J. Jovanović and M. D. Dramićanin, Temperature dependence of emission and lifetime in Eu^{3+}- and Dy^{3+}-doped GdVO4, *Appl. Opt.*, **2013**, 52, 1716–1724.

41   N. O. Nunez, S. Rivera, D. Alcantara, J. M. de la Fuente, J. Garcia-Sevillano and M. Ocana, Surface modified Eu:GdVO4 nanocrystals for optical and MRI imaging, *Dalton Trans.*, **2013**, 42, 10725–10734.

4 FUNCTIONALIZATION ASPECTS OF WATER DISPERSIBLE UPCONVERSION NANOPARTICLES

4.1 Abstract

Inorganic nanocrystals such as upconversion nanoparticles (UCNPs) attract great interest in bioanalytical applications due to their unique optical properties. One challenge is the colloidal stability of such materials in aqueous solutions and the ability of further functionalization with DNA, dyes, and antibodies. The most efficient synthetic strategies of upconversion nanoparticles in terms of small size and narrow size distribution rely on methods, which result in particles capped by surfactants. Consequently, only organic solvents can be used to obtain colloidally stable dispersions necessitating surface modification to achieve water dispersibility and surface functionalization. Here, three main strategies, the ligand exchange method, silanization and the formation of an amphiphilic bilayer, have been established. There are many aspects, which need to be taken into account when choosing the best strategy to modify upconversion nanoparticles in order to disperse them in buffered aqueous solutions. Most critical are the colloidal stability and the probability of crosslinking during the modification steps. For many applications, cytotoxicity as well as photophysical properties are of great importance. This chapter will critically discuss the main strategies to tune the surface chemistry of upconversion nanoparticles for their use as luminescent probes in imaging, as sensor material or in bioanalytical assays.

This chapter has been published.

Author contributions

MB and VM did the literature research and wrote the manuscript. SH designed **Figure 4.1** and **4.2** and revised the manuscript. The work was supvervised and revised by TH (corresponding author).

4.2 Introduction
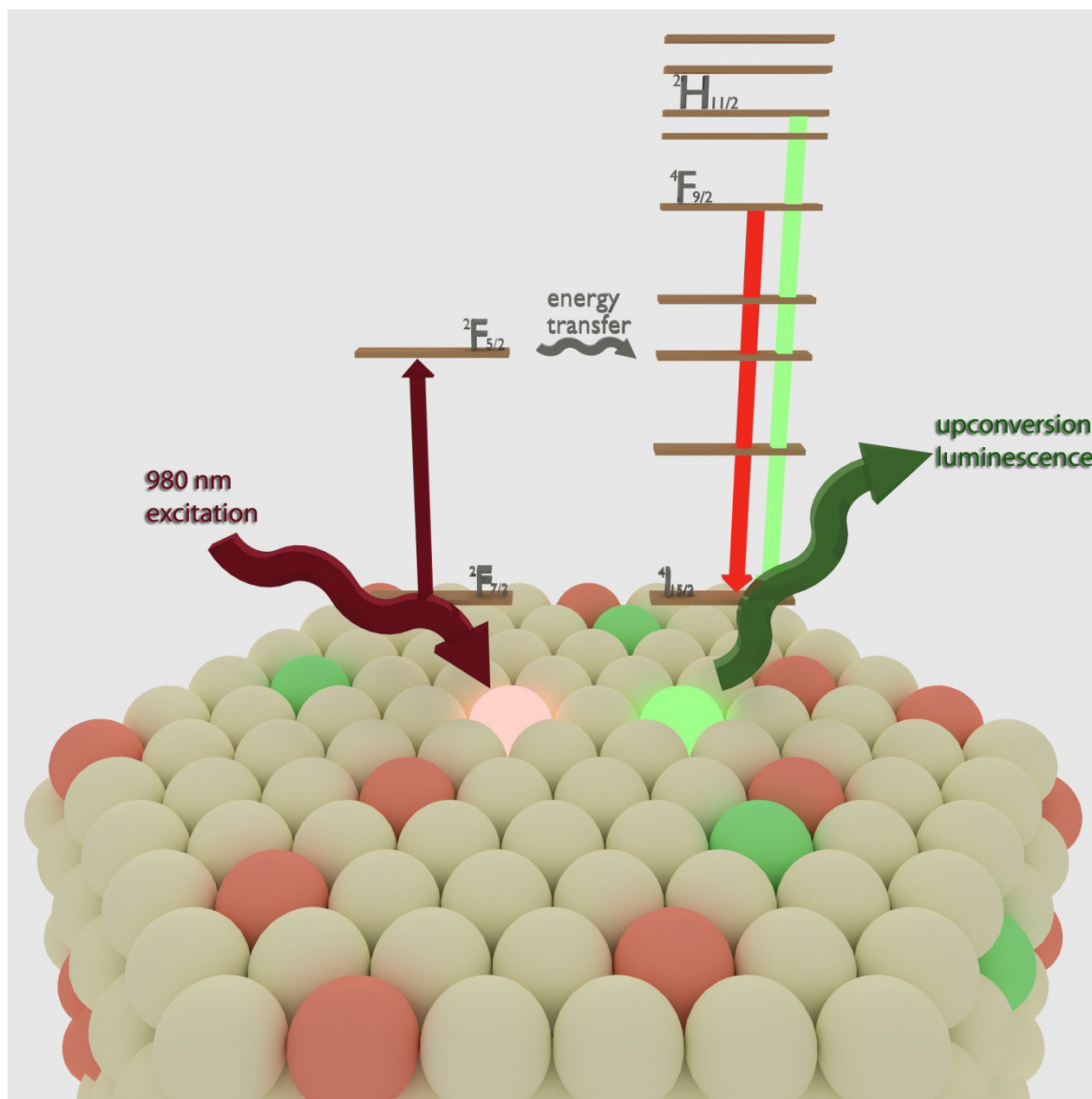
Figure 4.1 ‖ Hexagonal crystal lattice of NaYF$_4$ doped with 20% Yb ions and 2% Er ions. White spheres represent the Y^{3+} ions, red ones the Yb^{3+} and green ones the Er^{3+} ions. The Yb^{3+} ions are excited at 980 nm ($^2F_{7/2}$ → $^2F_{5/2}$) and transfer their energy to Er^{3+}, which can then either emit from the $^2H_{11/2}$ state (green emission) or the $^4F_{9/2}$ state after internal relaxation (red emission).

Upconversion nanoparticles (UCNPs)/nanomaterials have the unique property to absorb near-infrared (NIR) light which leads to an anti-Stokes emission from the ultraviolet (UV) over the visible to the NIR range.[1] The NIR light is absorbed by sensitizer ions (e.g., Yb^{3+} and Nd^{3+}), and then transferred to so-called activator ions (e.g., Tm^{3+}, Er^{3+}, and Ho^{3+}) via a nonradiative, resonant energy transfer process. The lanthanide ions are preferably embedded in host lattices with low phonon energy and similar ionic radii to reduce nonradiative deactivation processes.[2-4] Fluorides combine low phonon energies (~300–

38

400 cm^{-1}) with high chemical stability compared to other halide ions or oxide materials. The doping ratio of the sensitizer and activator ions is very critical, in order to generate highly fluorescent nanomaterials and to avoid self-quenching of the excited states. A NaYF$_4$ hexagonal host lattice doped with Yb^{3+} and Er^{3+} ions and a simplified overview of the energy transfers inside the crystal is depicted in **Figure 4.1**. The use of conventional fluorescent dyes in bioassays, biosensors, and imaging has been well established, but suffers from several drawbacks, such as high background fluorescence in biological matrices, photobleaching, small Stokes shifts, and short luminescence lifetimes. These disadvantages can be circumvented by the replacement of the dyes by UCNPs. The NIR excitation within the so-called optical window of biological material allows for deep tissue penetration without triggering autofluorescence of the matrix and reduced light scattering, leading to significantly higher signal-to-noise ratios. Beneficial properties, like high photostability, narrow emission bands, long luminescence lifetimes, and low cytotoxicity, additionally qualify UCNPs for their use in the design of biosensing applications. Both homogenous and heterogeneous assays have been developed, facing different challenges when dealing with the optimization of the surface modification process regarding stability, sensitivity, and selectivity. Nucleic acids, proteins, and fluorescent organic dyes represent the most popular signal molecules for detection schemes using UCNPs.

4.3 Synthesis of UCNPs

The three main strategies for the synthesis of UCNPs are the thermolysis, the Ostwald ripening, and the hydrothermal strategy.[5,6] The hydrothermal strategy is usually performed in autoclaves with Teflon inserts. The precursors are mixed with surfactants like ethylenediaminetetraacetic acid (EDTA) or polyethylenimine. Hydrothermal syntheses typically have reaction times from 5 up to 24 h under high-pressure and temperatures up to 200 °C.[7] The diameter of the nanoparticles is in the range of 100–500 nm. It is extremely difficult to obtain smaller particles, especially diameters of about 20 nm, which is important for biological applications. The size distribution of the synthesized particles has been improved over the last years, resulting in almost monodisperse UCNPs. Another drawback is that the progress of the reaction cannot be controlled and the synthesis of uniform core–shell particles has not been realized via the hydrothermal strategy so far. The main advantage of the hydrothermal synthesis is the preparation of directly water dispersible nanoparticles. In contrast, particles produced by thermal decomposition are not water dispersible after the synthesis.[8,9] The surface of the nanocrystal needs to be

stabilized with organic surfactants. The most commonly used organic surfactants are oleate, oleylamine, and trioctylphosphine oxide. However, this method is superior regarding particle-size distributions and crystallinity.

The Ostwald ripening strategy relies on the fact that the growth of larger particles is energetically favored compared to smaller nanoparticles.[10,11] The synthesis is carried out in high boiling solvents (e.g., oleic acid and octadecene). First, lanthanide–surfactant complexes are formed as precursors at room temperature. In the next step, the precursors are heated up to approximately 300 °C to grow the upconversion nanocrystals by Ostwald ripening. The advantages of the method are the narrow size distribution of the monodisperse nanoparticles, the purity in the crystal phase, and their enhanced optical properties. Wilhelm et al. (2015) showed that the progress of the reaction can be monitored by laser excitation allowing also a rough estimation of the size of the nanoparticles.[12] Furthermore, the synthesis of uniform core–shell nanoparticles can be achieved by the Ostwald ripening method. Wang and Liu (2014) summarized the synthesis of core–shell nanoparticles for multicolor imaging.[13] Moreover, Wang et al. (2010) showed that the luminescent properties of small nanoparticles (<20 nm) increase dramatically by the surface passivation effect when growing a non-doped shell consisting of $NaGdF_4$ around Yb^{3+} and Tm^{3+}-doped $NaGdF_4$ core particles.[14]

Jayakumar et al. (2014) reported new strategies to shift the excitation wavelength of the UCNPs from 980 to 808 nm by incorporating Nd^{3+} ions in core–shell nanoparticles.[15] In comparison with the excitation wavelength at 980 nm, water absorption is minimized under 808 nm laser excitation, yielding bright, luminescent nanoparticles in aqueous systems after successful surface modification. At the same time, the water heating effect caused by the 980 nm excitation is avoided, which is favorable for biological samples. One drawback of the Ostwald ripening method is the hydrophobic character of the nanoparticles, which requests further surface modification for bioanalytical applications.

4.4 Surface Modifications of Hydrophobic UCNPs

The development of increasingly advanced, reproducible, and controllable synthesis protocols for efficient UCNPs resulted in interesting possibilities for the investigation of novel, powerful biosensing applications. The most efficient way to synthesize small, monodisperse UCNPs up to date is the Ostwald ripening method.[16] As mentioned before, the particles are covered with surfactants like oleic acid or oleylamine. The polar headgroup of the surfactants points toward the surface of the nanoparticles and coordinates the metal ions at the surface of the nanoparticles. The hydrophobic tails point outwards and restrict the colloidal stability of the nanoparticles to organic solvents like chloroform or cyclohexane. Consequently, the need for effective surface modification strategies to transfer hydrophobic nanocrystals into aqueous media is increased. Over the years, a variety of methods to render the particles water dispersible have been developed. The most common and effective strategies can be categorized into three main groups: amphiphilic coatings, silica shell formation, and ligand exchange. These three methods are shown in **Figure 4.2** and are described as follows.
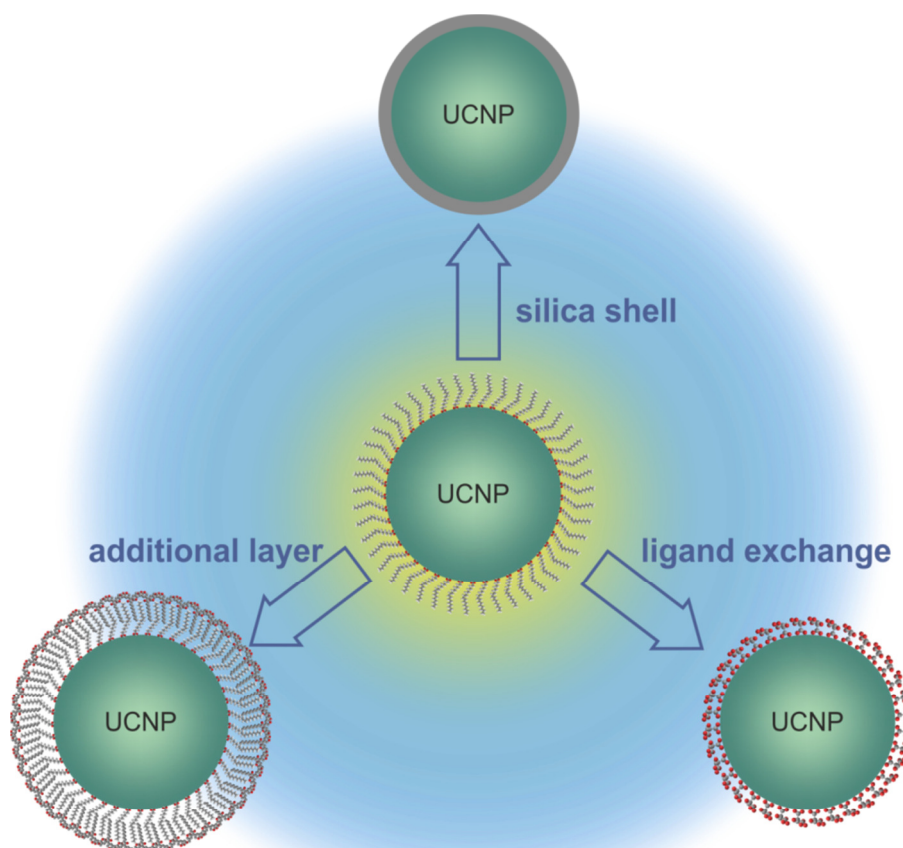

Figure 4.2‖ Overview of surface modification methods for transferring hydrophobic UCNPs into hydrophilic media by ligand exchange, additional layer deposition, and silica shell formation.

4.4.1 Amphiphilic Coatings

One straightforward and very powerful technique to warrant water dispersibility is the formation of an additional layer on top of oleate-capped UCNPs via the deposition of amphiphilic molecules. Their long alkyl chains are able to intercalate between the hydrophobic oleate molecules based on van-der-Waals (vdW) interactions, thus forming a bilayer around the particle surface. However, the maximum length of the alkyl chain leading to a successful surface coating is limited by the length of the oleate itself. If the chain length exceeds the length of the oleate, the vdW interaction becomes too weak to stabilize the bilayer. The hydrophilic head groups of the amphiphiles are directed toward the solvent, which consequently renders the particles dispersible in aqueous media. The choice of the head group provides a simple way to alter and adjust the resulting surface charge according to the desired application. This first charged layer on the particle surface also enables the possibility for layer-by-layer coatings, that is, the deposition of several layers with alternating charges. However, the head groups of the amphiphilic molecules do not only ensure water dispersibility. They also represent functional groups allowing for the coupling of the coated UCNPs to receptor molecules or the attachment of, for example, dyes and stabilizing molecules. In this context, phospholipids represent a group of frequently used amphiphiles for the surface modification of UCNPs. Phospholipids are commercially available with a great variety of different head groups, which ensures flexibility regarding the final surface coating. Particles modified with phospholipids are generally taken up by cells quite easily, and exhibit low cytotoxicity and biocompatibility, which is usually achieved by the addition of poly(ethylene glycol) (PEG) units (Nam et al. 2011; Park et al. 2009).[17,18]

However, phospholipids are quite challenging regarding their synthesis and consequently expensive. Therefore, surface modification using much less-expensive surfactants has also been investigated. For example, TWEEN- 80 (Ren et al. 2012) and several long-chain alkylammonium derived surfactants (Liang et al. 2012) have been successfully applied as amphiphilic surface coatings on UCNPs.[19,20] Nevertheless, the colloidal stability of the resulting particles in aqueous systems was not as good as of the phospholipid coated ones.

The use of amphiphilic polymers instead of small surfactants or phospholipids is one approach to further increase colloidal stability.[21] As these polymers contain a large number of hydrophobic alkyl chains per molecule, they are better stabilized against ligand detachment by a chelating effect. Poly(maleic anhydride-*alt*-1-octadecene) (PMAO) is the most widely used representative for the group of amphiphilic polymers.[22,23] UCNPs coated

with PMAO display excellent colloidal stability in buffers over a wide pH range and in cell culture media for weeks.[24]

4.4.2 Encapsulation with Silica

The deposition of a silica shell on UCNPs is one of the most common techniques to achieve water dispersibility and to introduce functional groups to the particle surface. Hydrophobic UCNPs can be coated with a uniform layer of silica based on a reverse microemulsion method, which involves the polymerization of silicate precursors in the presence of a surfactant that forms and stabilizes the reverse microemulsion. The precursor tetraethyl orthosilicate (TEOS) and the nonionic surfactant Igepal CO-520 are most often used. Usually, a small amount of ammonia is added in order to keep the concentration of silicic acid above the nucleation concentration, which leads to the steady growth of a uniform silica shell. The thickness of the resulting shell depends on the amount of both precursor material and surfactant present during the shell growth phase. Particles encapsulated within silica are dispersible in water, are taken up by cells fast, and display low cytotoxicity.[25]

Yet, the colloidal stability of such $UCNPs@SiO_2$ in aqueous dispersions is quite poor, which leads to their aggregation and consequently precipitation within hours.[26,27] This problem arises through the centrifugation of the particles during purification. After centrifugation, it is often completely impossible to redisperse the particles in water. One solution for this problem is the stabilization of the silica-coated UCNPs by an increased surface charge in order to reduce the aggregation tendency.[28] The desired high surface charge can be achieved by the introduction of negatively or positively charged functional groups on the silica surface. This can be done either by silanizing the already coated particles or by the addition of functional organosilanes during the polymerization process, for example, carboxyethylsilanetriol[29] or amino-propyltrimethoxysilane.[30] By optimizing the surface chemistry on $UCNPs@SiO_2$, it was possible to stabilize them in various kinds of buffers, including phosphate buffer and cell culture media. It is also possible to synthesize mesoporous silica shells around nanoparticles. They exhibit an extremely large surface area with tunable pore sizes. Molecules can be easily trapped inside the pores of this material. These properties make them especially interesting for applications in drug delivery.[31,32] Another possibility is to load the mesoporous shell with dyes or receptor molecules that otherwise would not be able to penetrate the cell membrane.[33]

4.4.3 Ligand Exchange

Surface modification by ligand exchange is a third possibility to obtain water dispersible UCNPs. Here, the original ligand, for example, oleate is replaced either by small hydrophilic molecules or polymers. In a typical one-step procedure, the hydrophobic UCNPs are treated with a solution containing an excess of the desired new surface ligand at elevated temperatures for several hours. Usually, the protocol has to be adjusted for every single ligand regarding optimum reaction conditions. Commonly used hydrophilic molecules for the modification of nanoparticles via ligand exchange are citrate, poly(acrylic acid) (PAA),[34] poly(vinylpyrrolidone),[35] and PEGylated compounds.[36] Other protocols for ligand exchange are based on two-step processes. The first step is the complete removal of the hydrophobic ligand oleate. One possibility to strip off the oleate is the addition of strong acids, for example, HCl.[37] The oleate is protonated by the acid and thus released from the particle surface, leading to the generation of more or less ligand free particles. Another way to remove the oleate is the treatment with nitrosyl tetrafluoroborate (NOBF$_4$).[38] In this case, BF$_4^-$ ions provide an electrostatic stabilization of the ligand free particles, consequently preventing particle aggregation during the exchange process, as it is usually the case for most one-step methods. In the second step, the desired new capping molecule is attached. After isolation and purification, the bare nanoparticles are stirred together with a solution containing the new surface ligand for passivation of the nanocrystal surface. Here, usually heating and protective gas are not required, and reaction times are considerably shorter compared to the more common one-step procedures.[39,40]

In general, ligand exchange is an extremely versatile technique, as there are almost no limitations to their applicability. The only requirement for the new ligand molecule is the presence of a functional group capable of coordinating to the surface of the UCNPs. Negatively charged groups, such as carboxylates, sulfonates, phosphonates, and readily available free electron pairs, like in amino groups, fulfill this requirement. Thus, almost every molecule containing at least one of the mentioned functional groups can be successfully applied for the ligand exchange process. In contrast to surface modification by amphiphilic coatings and silica shells, ligand exchange provides a way to attach the new ligand directly to the surface of the UCNPs. The distance between the particle and ligand is thus minimized, which is, for example, especially important for applications relying on energy transfer processes between UCNPs and organic dyes immobilized on their surface.

When working with multifunctional molecules, the concentration of the UCNPs and the desired ligand has to be carefully adjusted in order to prevent cross-linking between

several particles. Nevertheless, crosslinking and thus aggregation of the particles during the ligand exchange cannot be prevented completely. Another drawback of this method is the poor colloidal stability of the water dispersible UCNPs in solutions with high ionic strength and especially in phosphate buffer. Here, the use of strongly coordinating phosphates as new capping molecules provides increased stability in buffered.[41,42] Also, the application of water soluble polymers instead of small molecules as the new ligand, improves the temporal colloidal stability in these systems due to the higher stability of the polymer against its detachment from the particle surface. Additional to the water dispersibility, a great number of possible functions suitable for further coupling are provided at the surface, since not every single functional group of one polymer chain is directed toward the particle. The first charged polymer layer can also function as first charged layer for successive layer-by-layer coatings.[43]

To introduce biofunctionality to UCNPs, the surface of the water dispersible particles needs to be further engineered. The next chapters give an overview of strategies for coupling proteins, nucleic acids, and dyes to UCNPs as well as their bioanalytical applications.

4.5 Protein Conjugation

Antibodies, a special class of proteins and best known for their unique recognition ability, have been attached to UCNPs, for example, for the establishment of an immune sandwich assay of carcinoembryonic antigen (CEA).[44] The CEA in test samples was first captured with magnetic beads (MBs) coated with anti-CEA antibodies. After washing steps assisted by magnetic separation, the addition of PAA-capped UCNP with anti-CEA antibodies led to the formation of sandwich structures on the MBs connected by the CEA. Excess UCNP composites were removed and the luminescence emission of the UCNPs was recorded, resulting in a linear behavior for concentrations of the CEA between 0.05 and 20 ng·mL^{-1}. The anti-CEA coated UCNPs exhibited good stability in 4-(2-hydroxyethyl)-1-piperazineethanesulfonic acid (HEPES) buffer.

Ong et al. (2014) proved the high photostability of the UCNPs in comparison with the green fluorescent protein (GFP).[45] First, they performed a ligand exchange to remove oleate from the surface of the UCNPs and introduce citrate as a new ligand. As example, an anti-E. coli antibody was bound via classical 1-ethyl-3-(3-dimethylaminopropyl)-carbodiimide (EDC) chemistry to the citrate-coated nanoparticles. After binding to E. coli, the halftime of GFP was determined to 75 s by fluorescence imaging, while the signal of the UCNPs stayed nearly constant over 30 min. Special focus was put on the colloidal

stability and monodispersity of the nanoparticles. After the binding of the antibody, the hydrodynamic diameter of the particles increased about 200 nm with a low PdI of 0.162. Consequently, also with reference to the transmission electron microscopy (TEM) images, agglomeration was not critical. The binding of the particles to the E. coli cells showed only vulnerability against the growth medium lysogeny broth.

Binding of antibodies to silica-modified UCNPs generates conjugates of UCNPs and antibodies colloidally stable in phosphate buffer. Zhang et al. (2007) embedded a photosensitizer into silica shells around UCNPs and an anti-MUC1/episialin antibody was bound to the amino functionalized silica shell through cyanogen bromide.[46]

Qiao et al. presented a very elegant technique to bind antibodies to the surface of UCNPs.[47] They removed oleic acid from the core–shell $NaGdF_4$:Yb,Er@$NaGdF_4$ particles by heating to 50 °C and adding an asymmetric PEG containing a maleimide group at one end and a diphosphate on the other end. The disulfide groups of a monoclonal antibody were reduced with tris(2-carboxyethyl)phosphine hydrochloride and the obtained thiol groups were bound to the maleimide groups on the surface of the nanoparticles by click reaction. Due to the coordinating phosphate groups on the surface, the modified particles were even stable in phosphate buffered saline (PBS) and can be used for a large area of applications.

Wang et al. grew a silica shell around $NaYF_4$:Yb,Er nanoparticles using the classical *Stöber* synthesis.[30] In a second step, 3-aminopropyltrimethoxysilane was used to functionalize the surface of the nanoparticles with amino groups and a rabbit anti-CEA8 antibody was bound to the nanoparticles via EDC chemistry.

The unique recognition properties and the high catalytic activities of enzymes are commercially used in several bioassays and sensors. In combination with UCNPs, the most critical point is the crosslinking of the particles and enzymes after immobilization to the surface of the nanoparticles. Crosslinking and as a result changes in the tertiary structure lead to lower catalytic activities. Gao et al. immobilized a caged protein kinase (PKA) on the surface of UCNPs, which can be activated by NIR light inside cells.[48] $NaYF_4$:Yb,Tm nanoparticles were synthesized in high boiling solvents and a silica shell was formed by a reverse microemulsion method by adding Igepal CO-520 and TEOS. Considering the corresponding TEM images and dynamic light scattering (DLS) measurements, the particles were partially aggregated. The caged protein was bound to the surface of the silica-coated nanoparticles via electrostatic interactions. With the Bradford assay, the amount of the protein in the supernatant was calculated to roughly 4.5 nmol of PKA per 1 mg nanoparticle. The thiol groups of the enzymes were caged with o-nitrobenzyl bromide. After NIR excitation of the UCNPs, o-nitrobenzyl bromide was

cleaved from the active center as shown in **Figure 4.3** and the enzyme was used for the monitoring of intracellular signal transduction.
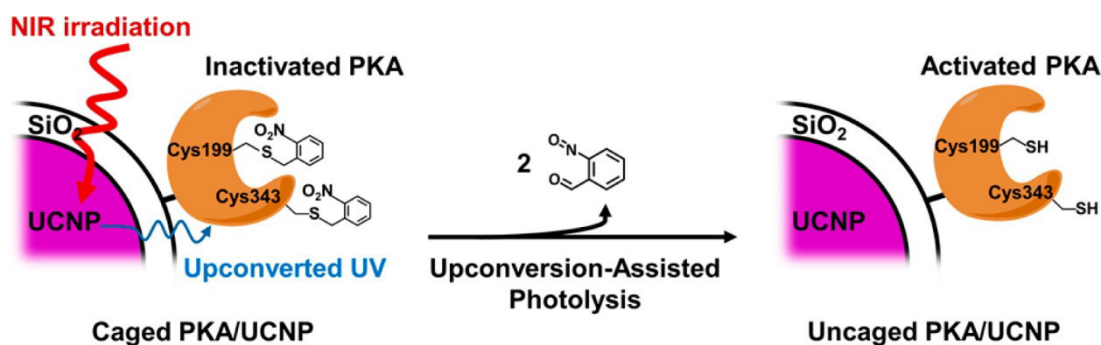

Figure 4.3 ‖ Caged PKA/UCNP complex design and the process of upconversion-assisted PKA uncaging. (Reprinted with permission from Gao, H.-D., P. Thanasekaran, C.-W. Chiang et al. 2015. Construction of a near-infrared-activatable enzyme platform to remotely trigger intracellular signal transduction using an upconversion nanoparticle. ACS Nano 9, 7041–7051. Copyright 2015 American Chemical Society.)

Chien et al. used a similar method to target cancer cells by creating a photoresponsive molecule with folic acid and o-nitrobenzyl bromide.[49] The photosensitive protecting group was cleaved from folic acid by NIR excitation. Wang et al. developed a successful detection method for hyaluronidase.[50] Hyaluronic acid-capped $NaYF_4$:Yb,Er UCNPs were bound with EDC chemistry to poly(m-phenylenediamine) nanospheres. Due to the electron rich properties of the nanospheres, the green emission of the UCNPs was fully quenched. In presence of hyaluronidase, the UCNPs were released from the surface and the green luminescence of the particles was recovered.

In relationship with UCNPs, enzymes are very often used in combination with organic molecules and dyes, which are able to absorb the emitted upconversion luminescence. Wilhelm et al. showed that they could monitor the production of nicotinamide adenine dinucleotide (NADH) and flavin adenine dinucleotide (FAD) due to the spectral overlap with Yb^{3+}, Tm^{3+}-doped core–shell $NaYF_4$ nanoparticles.[51] Wilhelm et al. presented a general approach for biomodification of silica-coated UCNPs with proteins.[52] First, a silica shell was formed by the reverse microemulsion method. Subsequently, the silica surface was modified with a silane-PEG2000-N-hydroxysuccinimide (NHS) for biocompatibility and reactivity toward amino groups. The functionalized particles were conjugated to streptavidin-coated MBs demonstrating the high reactivity toward proteins.

Min et al. used photoactivation through UCNPs to release a platinum antitumor drug.[53] An amino functionalized silica shell was formed around $NaYF_4$:Yb,Tm particles, using TEOS and (3-aminopropyl)triethoxysilane. Mal-dPEG$^{TM}_6$-NHS was used as a linker to bind trans, trans, trans- $[Pt(N_3)_2(OH)_2(py)_2]$ to a thiol group of a peptide linker to the silica surface of the particles. By NIR excitation, the cell toxic Pt(IV) complex was cleaved from the peptide

linker by the blue Tm^{3+} emission. The triggered cell death was monitored by an energy transfer of Tm^{3+}-doped particles to Cy5TM, also attached to the surface of the UCNPs. The energy transfer was first blocked by the quencher Qsy21, which was cleaved from the surface of the nanoparticles by caspase-3 by entering apoptosis.

4.6 Conjugation to Nucleic Acids

Nucleic acids play an irreplaceable role in the detection of pathogens and toxins. Countless DNA hybridization assays and aptasensors have been developed for quantification and imaging purposes in vitro and in vivo. While common colorimetric and fluorescence-based techniques usually suffer from high background signals, photobleaching or cytotoxicity, the application of UCNPs as fluorescent labels circumvents these drawbacks due to their NIR excitation, large anti-Stokes shifted emission, and exceptional photostability. The conjugation of nucleotides to the surface of UCNPs is the most critical step during the design of a sensor or imaging platform. Extensive crosslinking due to multifunctional ligands, control over the amount of receptors on the particle surface, and the stability of the modified UCNPs in buffers and cell culture media represent the most important factors to consider when facing the decision on the type of surface modification strategy.

Ligand exchange is by far the most popular technique to functionalize UCNPs with nucleic acids due to its abundant versatility and simplicity. Either the oligonucleotide itself is used for the ligand replacement and is directly bound to the particle surface, or water-soluble molecules or polymers containing functional groups are used as new surface ligands to which subsequently the nucleotides can be coupled. The direct attachment of the nucleic acids represents the most straightforward approach, as it does not require any precedent chemical modification of the DNA for coupling chemistry. The nucleotides are hereby efficiently bound to the surface of the UCNPs via their strongly coordinating phosphate moieties. Due to the high binding affinity of those phosphate groups on the particle surface, the DNA-coated UCNPs exhibit excellent colloidal stability in phosphate buffer and cell culture media.

For example, DNA was directly attached to NaYF$_4$:Yb,Tm@NaYF$_4$ nanoparticles aimed to determine S1 endonuclease activity.[54] The UCNPs were first modified with DNA by stirring the oligonucleotide together with oleate-capped particles in a two-phase system consisting of water and cyclohexane. The oleate was completely replaced by the ssDNA and the UCNPs were transferred into the aqueous phase. These DNA-modified UCNPs were able to adsorb to the surface of graphene oxide due to π-stacking interactions. Graphene oxide

is capable of quenching the luminescence of the UCNPs adsorbed on its surface. When the DNA on the UCNPs was cleaved by the addition of the endonuclease, the particles were released from the graphene oxide. Consequently, the quenching effect decreased, leading to stronger emission intensities of the UCNPs. By monitoring the increase of the luminescence intensity, S1 nuclease activity of $1 \cdot 10^{-4}$ units·mL^{-1} was detected selectively. The same group used the identical modification strategy with DNA via direct exchange at the liquid–liquid interface for the development of a detection scheme for Hg^{2+} ions based on nonradiative electron/hole recombination annihilation through an effective electron transfer process.[55] The Hg^{2+} ions could be selectively detected in a dynamic range between 10 nM and 10 µM.

In another example, the oleate ligand of NaYF$_4$:Yb,Er UCNPs was directly replaced by ssDNA by vigorous stirring in a water–chloroform mixture, leading to the formation of water dispersible DNA-coated particles.[56] The UCNP–DNA conjugate showed stability against ligand detachment after hybridization with the complementary DNA strand labeled with gold nanoparticles (AuNPs), illustrating their potential for applications in hybridization assays as shown in **Figure 4.4**.

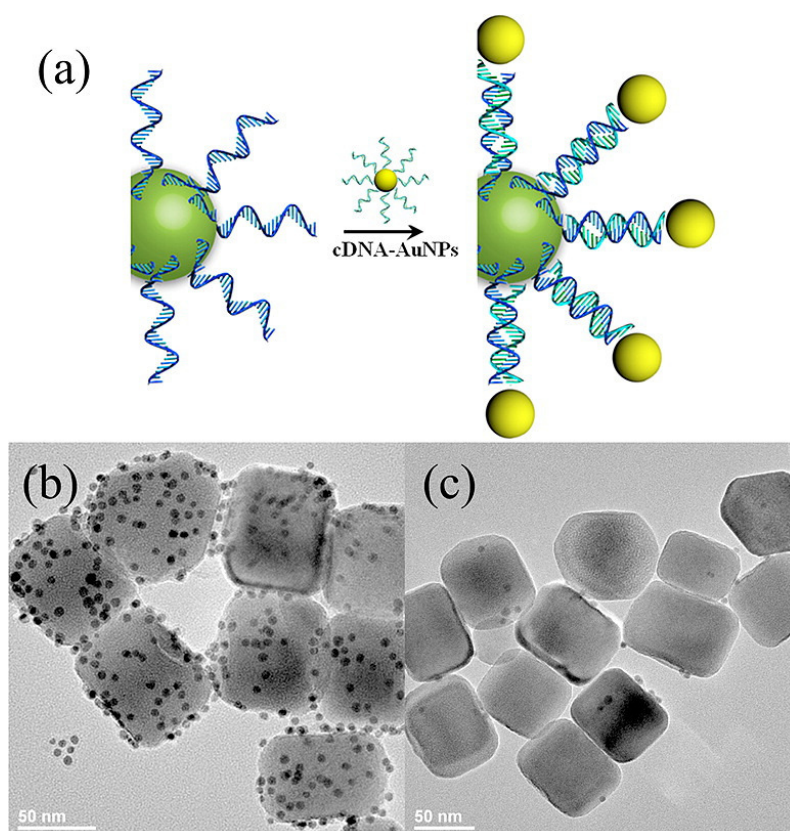**Figure 4.4‖ a**) DNA-directed assembly of UCNPs and AuNPs. TEM images of T30-UCNPs assembled with AuNPs bearing (**b**) complementary DNA and (**c**) noncomplementary DNA. (Reprinted with permission from Li et al. 2013. Copyright 2013 American Chemical Society.)

The possibility for cell imaging and cancer cell targeting was also demonstrated by the hybridization of the UCNP–DNA conjugates with Cy3 labeled complementary DNA or the immobilization of a nucleolin-specific aptamer on the UCNPs, respectively. The DNA-modified UCNPs showed exceptional transfection capabilities, making them an excellent material of choice for targeted bioimaging and gene delivery. Despite its simplicity, the direct attachment of the nucleotides is prone to several problems. Although the high binding affinity of the phosphate groups to the surface of the UCNPs leads to colloidal stability, the odds are that several UCNPs are crosslinked due the presence of multiple phosphate functionalities on one DNA strand. This can cause the formation of large networks and aggregates that are no longer colloidally stable in dispersion and precipitate. There is also the risk that the DNA strands wrap themselves around the particle. The nucleotides are then no longer available for any hybridization with the target DNA, which then leads to reduced detection sensitivities. This can be prevented by the use of linker molecules, which are first bound to the UCNPs by ligand exchange, followed by the coupling of nucleic acids in a second step. These linker molecules have to carry both, a functional group with high binding affinity to the surface of the UCNPs and carboxyl or amino moieties, for binding to correspondingly functionalized nucleic acids.

Small bifunctional molecules such as dimercaptosuccinic acid and aminoethanephosphonic acid have been successfully used as linkers for the conjugation of DNA to UCNPs.[57,58] After ligand exchange, the carboxyl and amino groups were activated with EDC/NHS or glutaraldehyde, respectively, in order to couple amino-functionalized DNA or avidin for subsequent attachment of biotin-modified DNA. Both conjugates were used for the design of energy transfer-based sensors for the detection of either microRNA or adenosine triphosphate (ATP).

Ligands containing single binding sites, like in the two examples mentioned above, are prone to detachment from the particle surface, particularly in buffers containing phosphate ions and high ionic strength in general. In contrast to that, the use of polymers comprising multiple binding sites provides better stabilization against ligand detachment and functional groups for subsequent bioconjugation. The most frequently applied polymer is PAA. In order to conjugate hydrophobic $NaYF_4$:Yb,Er,Mn to ssDNA for the detection of staphylococcal enterotoxin B (SEB), the oleate was first replaced by PAA in a one-step ligand exchange process in diethylene glycol.[59] The ssDNA was then attached to the PAA-coated particles via carbodiimide chemistry and afterwards hybridized with the complementary DNA strand labeled with the dark quencher BHQ3. After the hybridization, no red luminescence from the Mn^{2+}-doped UCNPs occurred. The degradation of the DNA by treatment with SEB led to the release of the quencher and consequently an increase of the UCNP luminescence intensity proportional to the SEB concentration. The detection

limit for SEB was determined to be as low as 0.3 pg·mL^{-1} with high reproducibility and specificity.

A similar approach was used for the development of a method for the simultaneous detection of three pathogenic bacteria.[60] Three different kinds of UCNPs were synthesized, each exhibiting a different emission wavelength in the blue (Tm), green (Ho), or red (Er, Mn) region. After exchanging the oleate with PAA in a one-step procedure in diethylene glycol, three different amino-functionalized DNA strands (aptamers) were attached to the carboxyl groups on the particle surface by activation with EDC/NHS. Magnetic nanoparticles (MNPs) were modified equally with the complementary DNA, and both particle types were connected by hybridization. When the target bacteria were present, the UCNP-aptamer conjugates preferably bound to the specific binding sites on the bacteria. The luminescence signal of the remaining UCNP–MNPs conjugates was evaluated after magnetic separation from the UCNPs bound to the bacteria. The more bacteria present, the lower was the residual upconversion luminescence intensity. The whole assay principle is displayed in **Figure 4.5**. The limits of detection for the three target bacteria were found to be between 10 and 25 cfu·mL^{-1}.

Ligand exchange is also popular for the design of heterogeneous immunoassays and aptasensors. Ulrich Krull et al. have especially performed pioneering research in the area of solid phase-based assay formats. They performed a hybridization assay based on energy transfer on cellulose paper.[61] The UCNPs were first coated with citrate via a two-step ligand exchange assisted by HCl, conjugated to streptavidin by carbodiimide activation, and suspended in borate buffer. The modified UCNPs were immobilized on cellulose paper in small spots and biotin-tagged probe DNA was bound to the particles on the paper. After treatment with the Cy3- labeled target DNA solution, the luminescence intensity of the UCNPs was read out using an epifluorescence microscope. The more target DNA was added, the lower was the remaining luminescence intensity due to a more efficient energy transfer from the UCNPs to the bound Cy3, achieving an limit of detection (LOD) of 34 fmol of target DNA. With this assay format, it was even possible to reliably discriminate between the complementary DNA and one base pair mismatch targets. In another approach, UCNPs bound on cover slips have been used for the detection of thrombin.[62] NaYF$_4$:Yb,Tm@NaYF$_4$ UCNPs were first modified with o-phosphorylethanolamine (PEA) by ligand exchange.
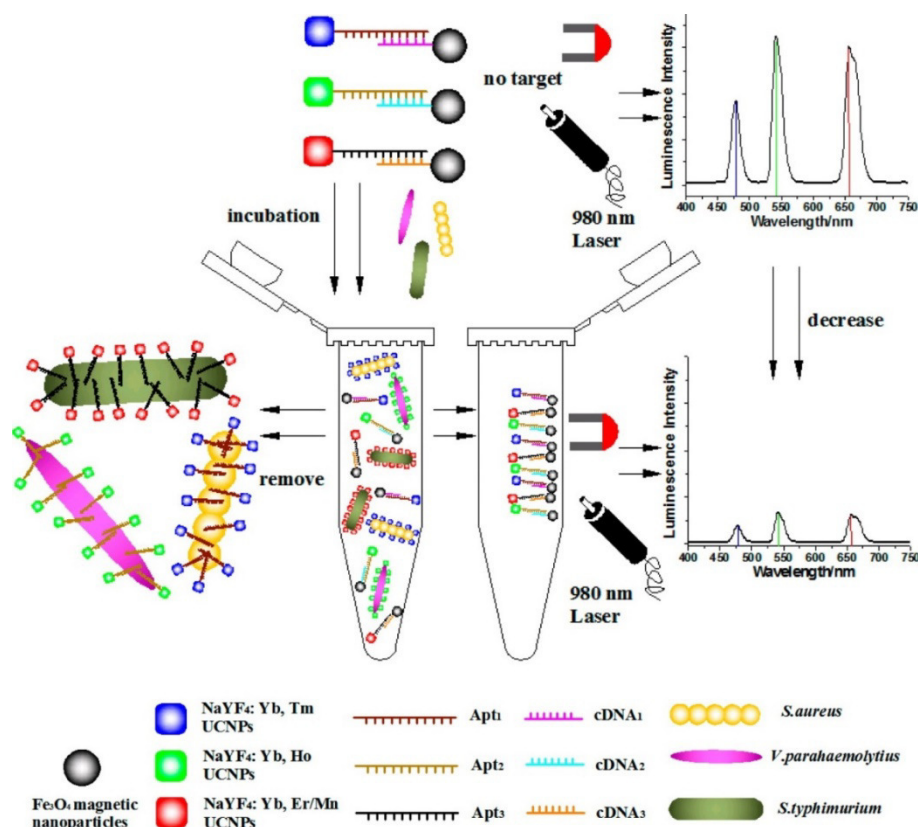
Figure 4.5‖ Schematic illustration of the multiplexed luminescence bioassay based on aptamer-modified UCNPs for the simultaneous detection of various pathogenic bacteria. (Reprinted with permission from Wu et al. 2014. Copyright 2013 American Chemical Society.)

These particles were then immobilized on aldehyde-functionalized cover slips forming a densely packed layer on the glass surface. The immobilized nanoparticles showed stability against washing at three different pH values of 5.5, 7.4, and 8.5; no leakage was observed. Next, a thrombin-specific aptamer was conjugated to the UCNPs on the cover slips. After thrombin was captured, quantum dots (QDs) also tagged with a thrombin-specific aptamer were added. The resulting conjugate is depicted in **Figure 4.6**. The overlap of the UCNP emission and the QD absorption led to a reduction of the observed upconversion luminescence intensity of the UCNPs and to an increase of the luminescence of the QDs. It was possible to detect down to 230 fmol thrombin by evaluation of the intensity ratios of all involved emission peaks.

Figure 4.6‖ Schematic showing immobilization of PEA-UCNP on aldehyde-functionalized cover slip and use in the detection of thrombin using two different thrombin-specific aptamers. (Reprinted with permission from Doughan, S., Y. Han, U. Uddayasankar, and U. J. Krull. 2014. Solid-phase covalent immobilization of upconverting nanoparticles for biosensing by luminescence resonance energy transfer. ACS Appl. Mater. Inter. 6, 14061–14068. Copyright 2014 American Chemical Society.)
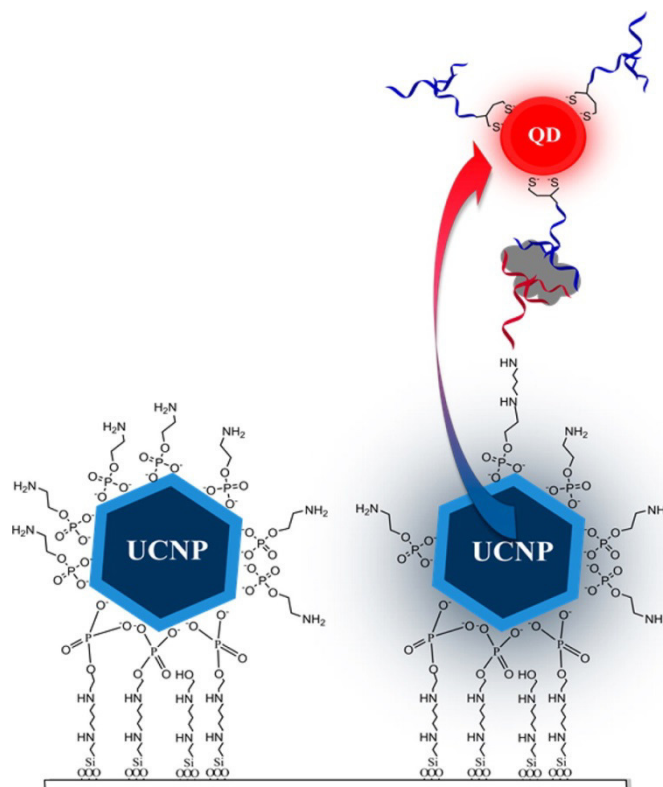
Generally, UCNP–DNA conjugates obtained via ligand replacement are prone to aggregation during the exchange process caused by crosslinking between multiple particles and control over the loading capacity of the nucleic acids on the particle surface is rather difficult. The formation of a bilayer on top of oleate-coated UCNPs with the help of amphiphilic molecules is much less commonly used to prepare particles for conjugation to nucleic acids, but does not suffer from the same drawbacks as the ligand exchange strategy mentioned earlier. In one example, such UCNPs were used for the determination of human immunodeficiency virus (HIV) antibodies.[63] Here, the particles were simultaneously modified with two different phospholipids in order to control the receptor density on the particle surface. One lipid carried a PEG chain imparting increased colloidal stability and biocompatibility, the other one an HIV specific aptamer. The luminescence of these water dispersible UCNPs was completely quenched by GOx due to π-stacking interactions. In the presence of HIV, the aptamer immobilized on the particles specifically bound to the target virus, which prevented the adsorption to the GOx and led to linearly increasing luminescence intensity for HIV concentrations between 5 and 150 nM in diluted human blood serum.

Coating with phospholipids enables efficient control over surface loading with the DNA probe in one step by adjusting the ratio of two or more different phospholipids used for the surface modification, while at the same time imparting excellent colloidal stability in a variety of buffers. However, phospholipids are expensive and their synthesis and purification is fairly elaborate. A second scarcely employed strategy for the immobilization of nucleotides to UCNPs is the prevenient growth of a functional silica shell suitable for bioconjugation.
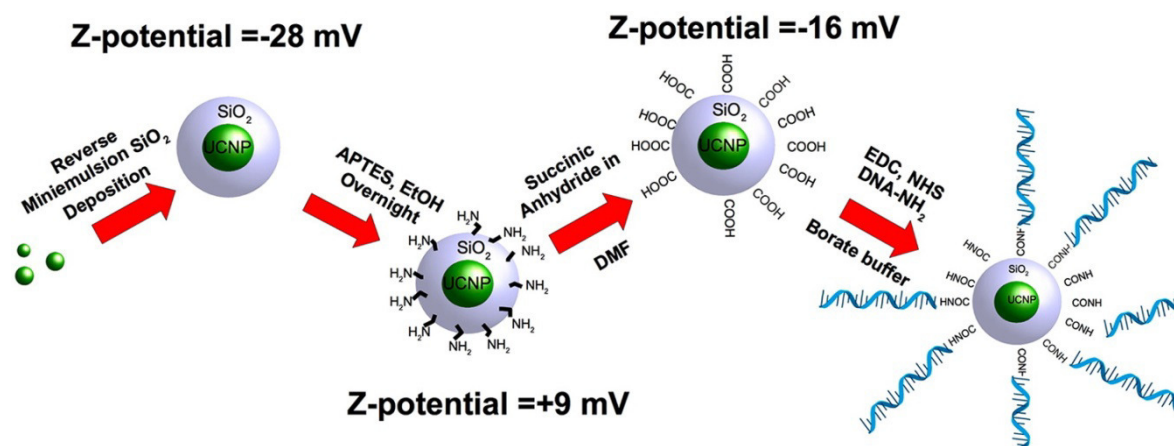
Figure 4.7‖ Schematic illustration of the chemical route for the functionalization of UCNPs@SiO2 nanoparticles. (Reprinted with permission from Alonso-Cristobal, P., P. Vilela, A. El-Sagheer et al. 2015. Highly sensitive DNA sensor based on upconversion nanoparticles and graphene oxide. ACS Appl. Mater. Inter. 7, 12422–12429. Copyright 2015 American Chemical Society.).

For the design of a DNA sensor, the polymerization of TEOS around the particles in a reverse microemulsion was followed by silanization with 3-aminopropyl triethoxysilane, resulting in amino-functionalized $NaYF_4$:Yb,Er@SiO_2.[64] The amino groups were then reacted with succinic anhydride and the resulting carboxyl moieties were used for the attachment of amino-functionalized ssDNA via carbodiimide coupling, as illustrated in **Figure 4.7**. Due to electrostatic repulsion between the charged functional groups, the reaction steps did not cause aggregation, precipitation of the particles, and no crosslinking was observed. The hybridization of the target DNA to the modified UCNPs was monitored by the evaluation of the quenching efficiency of GOx caused by π–π interactions with the remaining ssDNA on the particles. The LOD of this sensor setup was calculated to be 5 nM.

4.7 Conjugation to Dyes

Fluorescent dyes are the most important tools for cellular imaging, sensing of intracellular parameters, and bioassays. Yet, many applications are limited by photobleaching and low signal-to-noise ratios caused by strong scattering of UV light, high autofluorescence, and unspecific binding. NIR excitable UCNPs can act as nanocarriers for those established dyes and eliminate these shortcomings by the design of conjugates relying on energy transfer mechanisms between the particles and the respective dyes. All applications share the necessity to select dyes that feature an overlap of their absorption spectrum with any emission band of the UCNPs. With this requirement in mind, numerous sensing schemes based on Förster resonance energy transfer (FRET) and inner filter effects have been reported. Almost as many different surface modification strategies for the attachment of fluorescent dyes to the particles have been described, all of which vary regarding stability, surface loading, distance between donor and acceptor, and sensitivity. All these parameters have to be carefully evaluated in respect to the final application before choosing one method.

Ligand exchange facilitates the attachment of dyes directly to the surface of UCNPs, which is especially favorable for efficient FRET processes due to the minimization of the distance between the donor–acceptor pair. In respect to applications in biological systems, this method only works for dyes which are water soluble and carry at least one functional group capable of binding to the surface of the UCNPs. Consequently, the colloidal stability in aqueous media solely depends on the binding affinity and stabilizing properties of the dye. The direct immobilization of the dye by ligand exchange was used for the in vivo detection of hydroxyl radicals.[65] The oleate was first removed from the surface of hydrophobic $NaYF_4$:Yb,Tm@$NaYF_4$ UCNPs by the addition of HCl.
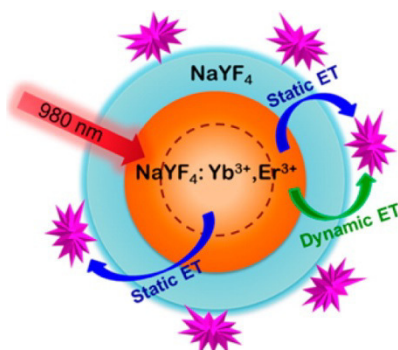

Figure 4.8‖ Energy transfer model from Er^{3+} in core–shell $NaYF_4$:Yb^{3+},Er^{3+}@$NaYF_4$ UCNPs to surface-bound acceptor rose bengal. (Reprinted with permission from Ding et al. 2015. Copyright 2015 American Chemical Society.)

Subsequently, the surface of the obtained ligand free particles was passivated with a carboxyl-modified azo dye that absorbed the blue luminescence around 475 nm of the UCNPs and efficiently quenched the intensity of the affected UCNP emission. Hydroxyl radicals oxidized the azo dye, thus altering its absorption properties and preventing the energy transfer from the UCNPs. This process was monitored by the corresponding increase of the luminescence intensity of the blue UCNP emission. The colloidal stability of the nanoprobes under physiological conditions was sufficient for the successful performance of in vivo measurements.

If the active dye does not possess any functional groups or only weakly coordinating ones, a linker molecule can be first attached to the UCNPs by ligand replacement. This first layer can then be used to immobilize the respective dyes covalently or electrostatically. Suitable linkers in these cases are hydrophilic polymers, like PAA and poly(allyl amine) (PAAm). They simultaneously impart water dispersibility, a high surface charge for electrostatic adsorption, and functional groups for covalent attachment of the dyes. This strategy was used for the development of a UCNP nanocarrier for the photosensitizer rose bengal.[66] First, the oleate was exchanged with PAAm assisted by the addition of HCl. Afterwards, rose bengal was coupled to the amino groups by carbodiimide activation. **Figure 4.8** shows the modified core–shell nanoparticles with the covalently bound dye molecules. The resulting system was used to determine the effect of the distance between UCNP and dye on the energy transfer efficiency. In another example, PAA was introduced as the first polymer layer after the ligand exchange.[67] A positively charged Zn^{2+} sensitive dye was adsorbed to the polymer-coated UCNPs via electrostatic interactions. In the absence of Zn^{2+} ions, the absorption of the dye nicely overlaps with the blue emission of $NaYF_4$:Yb,Tm. Increasing Zn^{2+} concentrations cause a blue shift of the dye absorption and the recovery of the UCNP emission. The modified particles were stable in cell culture media and were successfully applied for in vivo detection of Zn^{2+} in zebrafish. Protease activities have also been monitored based on energy transfer between UCNPs and the fluorescent dye carboxytetramethylrhodamine (TAMRA) (Zeng et al. 2015). The C-terminus of an oligopeptide was modified with TAMRA and the peptide was immobilized on the surface of UCNPs by ligand exchange, resulting in a reduction of the luminescence intensity of the green upconversion emission. Cleavage of the peptide by trypsin and caspase-3 released the TAMRA dye from the particle surface and the emission intensity gradually increased. The particles displayed great colloidal stability when transferred into water under high peptide concentrations to ensure sufficient surface coverage and charge. They were used for the sensitive determination of protease activities and tumor cell imaging.

Hydrophobic, not water-soluble dyes cannot be attached to the UCNPs via ligand exchange for use in bioapplications, as they do not render the particles water dispersible. One alternative is the coating of oleate-capped UCNPs with amphiphilic molecules. This technique can be used to trap small dyes (and other molecules) inside the hydrophobic bilayer. At the same time, the particles are transferred into the aqueous phase and the choice of the amphiphilic molecule provides additional possibilities for further conjugation steps. Modifications with amphiphilic molecules generally display low aggregation tendencies during the coating process and lead to excellent colloidal stability in various buffers and cell culture media. The photosensitizer merocyanine 540 was loaded into the bilayer formed by the addition of various phospholipids or amphiphilic polymers, such as the triblock copolymer Pluronic®F-127 to oleate-capped UCNPs.[69,70] Furthermore, the particles were decorated with targeting moieties for tumor cells.
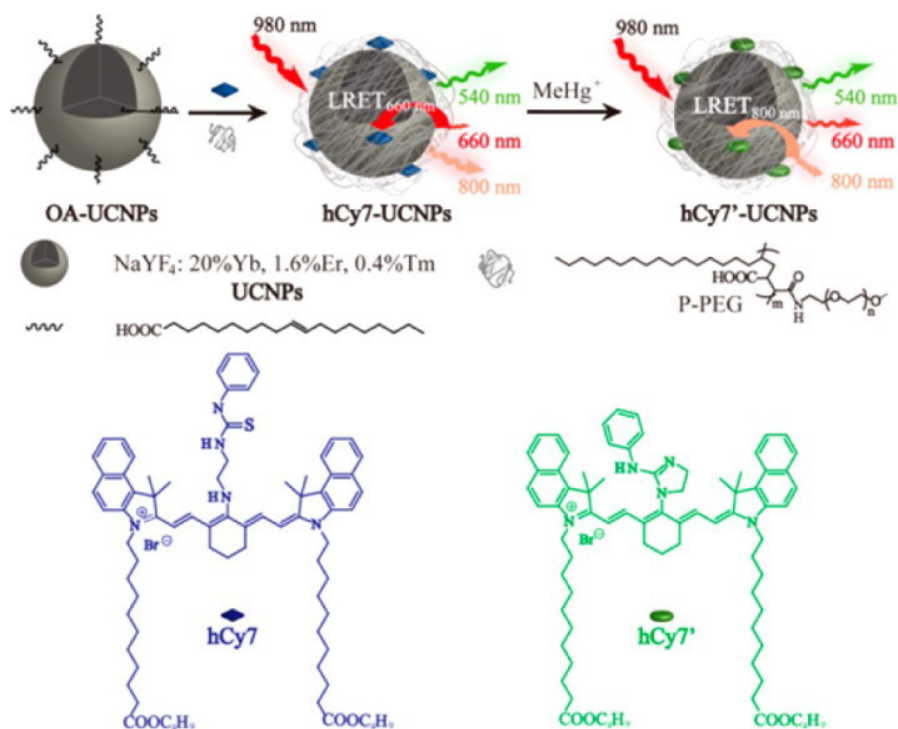
Figure 4.9 ‖ Schematic illustration of the synthesis of UCNPs-hCy7 and its sensing principle to MeHg$^+$ with a change in upconversion emission. (Reprinted with permission from Liu et al. 2013. Copyright 2013 American Chemical Society.)

The successful entrapment of the photosensitizer within the hydrophobic bilayer was demonstrated by the efficient production of singlet oxygen upon NIR excitation of the UCNPs and energy transfer to the MC540 inside breast cancer cells.

Molecules inside the hydrophobic bilayer were shown to retain their responsive properties. For example, the methylmercury sensitive cyanine dye hCy7 was immobilized within a bilayer formed by the amphiphilic blockpolymer PMAO–PEG and the oleate ligands.[71] In absence of methylmercury, the red emission at 660 nm of the UCNPs was quenched due to an efficient energy transfer to the dye. The addition of methylmercury induced a shift of the hCy7 absorption and the upconversion luminescence was recovered. **Figure 4.9** shows the surface modification and the detection principle of the nanoparticles against MeHg$^+$. The sensor did not show cross sensitivity to numerous metal ions while methylmercury could be monitored in vivo with a detection limit of about 0.8 ppb.

The same group used a very similar technique to detect hypochlorite.[72] They incorporated the cyanine dye hCy3 with long alkyl side chains inside the bilayer formed by an amphiphilic polymer around oleate capped NaYF$_4$:Yb,Nd,Er@NaYF$_4$:Nd nanoparticles. The hCy3 dye was able to absorb the green emission of the UCNPs. The fluorescent dye reacted irreversibly with ClO$^-$ leading to an increase of the luminescence intensity of the

upconversion nanocrystals. Hypochlorite pretreated HeLa cells were incubated with the 808 nm excitable nanoparticles to detect the pathogen using confocal microscopy. Aside from entrapment within the surfactant bilayer, the dyes can also be covalently attached to the hydrophilic part of the amphiphilic molecules. This is required if the dyes are too hydrophilic for efficient vdW interactions with the alkyl chains or too large for stable incorporation in the bilayer in order to prevent leakage. With this strategy, UCNPs coated with both a porphyrin-functionalized phospholipid and a PEG–phospholipid suitable for multimodal imaging were obtained.[73] Despite only two imaging components were used, the UCNP itself and the porphyrin, the particles were active in six different imaging modalities, including positron emission tomography, X-ray computed tomography, and photoacoustic imaging. This was demonstrated by in vivo lymphatic imaging in mice and revealed significant contrast enhancement.

High stability against leaching of the dyes from the surface of the UCNPs is provided by silica coating with subsequent covalent attachment of the dye. The conjugation can be performed by either surface silanization with silane modified dyes or by coupling to functional groups on the silica surface. The former method was used for the design of core–shell nanocomposites for NIR imaging and photothermal therapy.[74] $NaYF_4$:Yb,Er UCNPs were encapsulated inside a silica shell by the polymerization of TEOS via the reverse microemulsion method. Secondly, the silane-modified NIR canine dye CyTE-777-triethoxysilane was covalently bound to the silica shell. These dye carrying nanoparticles were colloidally stable in water for over 1 year. Incubation of macrophage cells with the nanocomposites enabled upconversion imaging upon excitation at 980 nm. Excitation of the organic dye loaded on the surface of the UCNPs led to efficient cell death and a cell viability of only 50% after 1 h, proving the photothermal treatment capabilities of the particles. Functional groups can be integrated into the silica shell by the addition of functional organosilanes during the growth period of the silica shell.
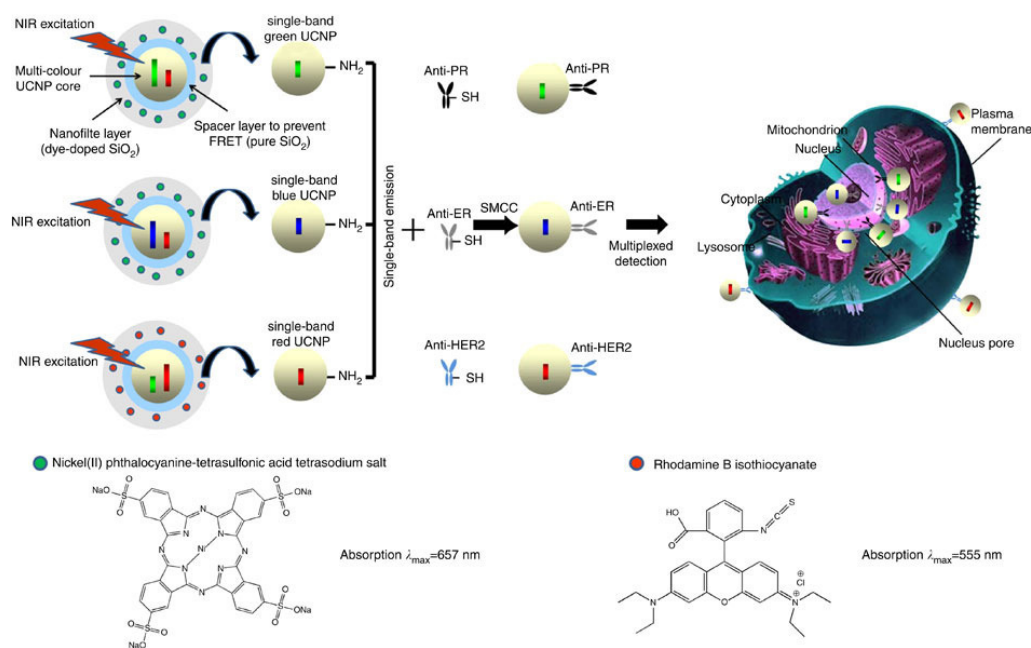
Figure 4.10 ‖ Surface amino modifications of the multilayer structure of green, blue, and red single-band emitting UCNPs and conjugates with antibodies for multiplexed *in situ* molecular mapping of breast cancer biomarkers. (Reprinted with permission from Zhou, L., R. Wang, C. Yao et al. 2015. Single-band upconversion nanoprobes for multiplexed simultaneous *in situ* molecular mapping of cancer biomarkers. *Nat. Commun.* 6, 6938, distributed under a Creative Commons CC-BY license.).

Amino groups were generated by the application of, for example, (N-(3-trimethoxysilyl)propyl)ethylene diamine and 3-(triethoxysilyl)propyl isocyanate in the polymerization phase.[75,76] Afterwards, pH-sensitive organic dyes, pHrodo™ Red and xylene orange, displaying a spectral overlap with one emission band of the UCNPs were coupled to those amino groups via EDC/NHS chemistry. The ratiometric readout of pH-induced changes in the emission intensities caused by shifts in the absorption spectra of the dyes revealed a resolution of 0.3 pH units. Furthermore, as the UCNP–dye composites were colloidally stable under physiological conditions, they were used for the imaging of intracellular pH values inside HeLa cells.

Dyes can also be directly and covalently integrated into the silica shell.[77] In one example, first a silica shell was formed around UCNPs with three different dopants by the polymerization of TEOS. Then, either aminopropyl triethoxysilane-modified rhodamine B isothiocyanate or nickel (II) phthalocyanine-tetrasulfonic acid was added and polymerized on top of the previous silica shell. This dye-containing layer served as an emission filter to generate single-band emitting UCNPs and provided dispersibility and stability in physiological buffers. This way, single green, red, and blue emitting UCNPs were obtained by filtering either the red or the green emission in Yb,Er- and Yb,Tm-doped particles, respectively, with the dye layer. The conjugation to specific antibodies was performed by coupling to the amino groups of the dye-doped silica shell. The surface engineering

leading to these single-band emitting conjugates is shown in **Figure 4.10**. The excellent properties of the modified UCNPs were demonstrated by multiplexed imaging of cancer biomarkers.

Although intentional in the last example, the downside of the modification with a silica shell regarding energy transfer efficiency is the significant increase of the distance between the donor UCNPs and the acceptor dyes. Mesoporous or rattle-structured silica at least partly bypasses this problem, since the attachment of the dye does not only occur at the outer surface of the silica shell, but also within the whole shell itself.[78,79] This also significantly increases the loading capacity of the whole system due to a greatly enlarged surface area available for the immobilization.

Mesoporous silica (mSiO$_2$) is usually synthesized by removing the template for the porous structure after the polymerization of the silicate precursors. In a first step, the silica shell is completely formed around UCNPs coated with surfactants, such as hexadecyl trimethylammonium bromide (CTAB). Subsequently, the surfactant can be removed by ion exchange, resulting in the formation of disordered, wormhole-like structures inside the silica shell.[80] Particles covered with mSiO$_2$ displayed colloidal stability in PBS. The pores were, for example, loaded with a merocyanine (MC) dye, which is reactive against hydrogen sulfide. Its oxidized form possesses a spectral overlap with the green UCNP emission, while the reduced structure formed in presence of HS$^-$ does not, as illustrated in **Figure 4.11**. This allowed the ratiometric evaluation of the luminescence intensities with a detection limit of 0.58 μM.
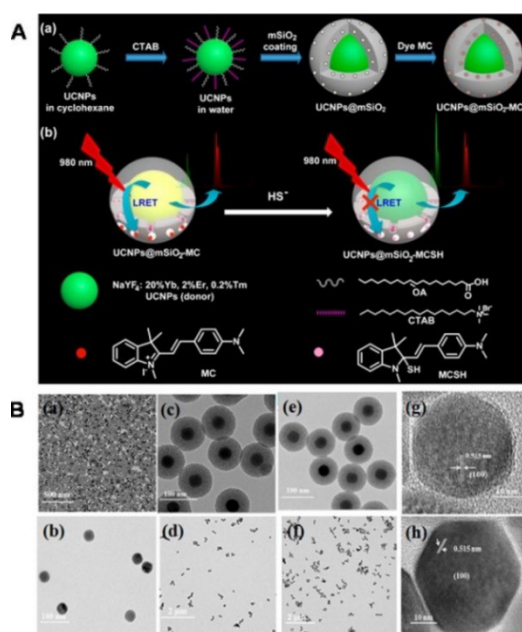

Figure 4.11‖ A) Design strategy and synthetic route of nanoprobe UCNPs@SiO$_2$-MC. **B**) Sensing mechanism and energy transfer process of UCNPs@SiO$_2$-MC toward HS$^-$. (Adapted with permission from Liu et al. 2014. Copyright 2014 American Chemical Society.).

4.8 Conclusion

The most common surface modifications of hydrophobic UCNPs are the ligand exchange method and the encapsulation with silica to obtain water stable dispersions. For the ligand exchange strategy, PAA is the most popular hydrophilic ligand, due to its high binding affinity to the surface of the nanoparticles utilizing the chelate effect. Direct attachment of the signal molecules is also a frequently performed method requiring only functional groups capable of coordinating to the lanthanide ions on the surface. Encapsulation with inorganic silica shells creates colloidally stable particles in aqueous media. One drawback of the silica coating is the tendency for agglomeration, especially after centrifugation, which can be avoided by smart surface engineering. The modified nanoparticles are often colloidally stable in HEPES and tris(hydroxymethyl)aminomethane (TRIS) buffer; however, they suffer from agglomeration in phosphate-buffered solutions. To achieve stability in PBS, coating with phospholipids and ligand exchange with phosphonic acid groups have proven their applicability in biological samples. For further (bio)modification, almost exclusively classical EDC chemistry or maleimide chemistry are used to bind DNA, dyes, and proteins to the surface of the particles. The overall well-established click chemistry is scarcely applied for bioconjugation of UCNPs.[81,82] Very often the aspects of crosslinking and agglomeration are not further discussed. **Table 4.1** gives a general overview of aspects to consider when choosing the appropriate surface modification method for different applications.

Table 4.1‖ Suitability of surface modification strategies regarding the final application.

Application	Surface Modification Strategy	Advantages
Sensors (via energy transfer)	Ligand exchange, mesoporous silica shell	Minimum distance between donor and acceptor
Electrophoresis	Amphiphilic polymers, silica coating	Stability against ligand detachment
Cellular imaging	Silica coating, amphiphilic polymers	Stability in cell culture media
Bioconjugation	Amphiphilic molecules, silica coating, ligand exchange	Variety of head groups available, stability in buffers
Cellular uptake	Amphiphilic polymers, silica shell	Mimicking of biological systems, tunable surface charge

One general issue of all surface modifications is the difficulty to compare individual methods and the absence of a standard for the surface characterization. The amount of surface ligands and signal molecules is often not characterized resulting in a low reproducibility of the techniques. For example, the amount of dye molecules loaded onto the surface of UCNPs nanoparticles is rarely specified or proofed. Due to the high dye loading capacities of the UCNPs, absorbance and fluorescence measurements are only conditionally suitable. Therefore, inductively coupled plasma measurements, nuclear magnetic resonance spectroscopy, and thermogravimetric analysis should be generally established to characterize the surface of the modified UCNPs. Despite the challenges in characterization and control of the surface properties of functionalized UCNPs, numerous bioapplications of UCNPs clearly demonstrate the outstanding advantage of almost background free measurements upon NIR excitation. Nevertheless, the strong water absorption at the typical excitation wavelength of 980 nm causes heating of biological samples and low upconversion efficiency. This drawback has recently been overcome by the design of core–shell architectures with additional Nd^{3+} ions as sensitizers, shifting the excitation wavelength to 808 nm. It is expected that this class of UCNPs will gain further interest in upconversion technologies, especially for bioanalytical applications.

References

1   F. Zhang, Photon upconversion nanomaterials. *Nan. Sci. Tec.* New York: Springer, **2014**.

2   F. Wang and X. Liu, Recent advances in the chemistry of lanthanide-doped upconversion nanocrystals, *Chem. Soc. Rev.*, **2009**, 38, 976–989.

3   M. Haase and H. Schäfer, Upconverting Nanoparticles, *Angew. Chem. Int.*, **2011**, 50, 5808–5829.

4   J. F. Suyver, J. Grimm, M. K. van Veen, D. Biner, K. W. Krämer and H. U. Güdel, Upconversion spectroscopy and properties of $NaYF_4$ doped with Er^{3+}, Tm^{3+} and/or Yb^{3+}, *J. Lumin.*, **2006**, 117, 1–12.

5   G. Chen, H. Qiu, P. N. Prasad and X. Chen, Upconversion nanoparticles: design, nanochemistry, and applications in theranostics, *Chem. Rev.*, **2014**, 114, 5161–5214.

6   J. Zhou, Z. Liu and F. Li, Upconversion nanophosphors for small-animal imaging, *Chem. Soc. Rev.*, **2012**, 41, 1323–1349.

7   L. Wang, W. Qin, Z. Liu, D. Zhao, G. Qin, W. Di and C. He, Improved 800 nm emission of Tm^{3+} sensitized by Yb^{3+} and Ho^{3+} in β-$NaYF_4$ nanocrystals under 980 nm excitation, *Opt. Express*, **2012**, 20, 7602–7607.

8   J.-C. Boyer, F. Vetrone, L. A. Cuccia and J. A. Capobianco, Synthesis of colloidal upconverting NaYF$_4$ nanocrystals doped with Er^{3+}, Yb^{3+} and Tm^{3+}, Yb^{3+} via thermal decomposition of lanthanide trifluoroacetate precursors, *J. Am. Chem. Soc.*, **2006**, 128, 7444–7445.

9   J.-C. Boyer, L. A. Cuccia and J. A. Capobianco, Synthesis of colloidal upconverting NaYF$_4$: Er^{3+}/Yb^{3+} and Tm^{3+}/Yb^{3+} monodisperse nanocrystals, *Nano. Lett.*, **2007**, 7, 847–852.

10   N. J. J. Johnson, A. Korinek, C. Dong and van Veggel, Frank C J M, Self-focusing by Ostwald ripening: a strategy for layer-by-layer epitaxial growth on upconverting nanocrystals, *J. Am. Chem. Soc.*, **2012**, 134, 11068–11071.

11   T. Rinkel, J. Nordmann, A. N. Raj and M. Haase, Ostwald-ripening and particle size focussing of sub-10 nm NaYF$_4$ upconversion nanocrystals, *Nanoscale*, **2014**, 6, 14523–14530.

12   S. Wilhelm, M. Kaiser, C. Würth, J. Heiland, C. Carrillo-Carrion, V. Muhr, O. S. Wolfbeis, W. J. Parak, U. Resch-Genger and T. Hirsch, Water dispersible upconverting nanoparticles: effects of surface modification on their luminescence and colloidal stability, *Nanoscale*, **2015**, 7, 1403–1410.

13   F. Wang and X. Liu, Multicolor tuning of lanthanide-doped nanoparticles by single wavelength excitation, *Acc. Chem. Res.*, **2014**, 47, 1378–1385.

14   F. Wang, J. Wang and X. Liu, Direct evidence of a surface quenching effect on size-dependent luminescence of upconversion nanoparticles, *Angew. Chem. In. Ed.*, **2010**, 49, 7456–7460.

15   M. K. G. Jayakumar, N. M. Idris, K. Huang and Y. Zhang, A paradigm shift in the excitation wavelength of upconversion nanoparticles, *Nanoscale*, **2014**, 6, 8441–8443.

16   V. Muhr, S. Wilhelm, T. Hirsch and O. S. Wolfbeis, Upconversion nanoparticles: from hydrophobic to hydrophilic surfaces, *Acc. Chem. Res.*, **2014**, 47, 3481–3493.

17   Y. I. Park, J. H. Kim, K. T. Lee, K.-S. Jeon, H. B. Na, J. H. Yu, H. M. Kim, N. Lee, S. H. Choi, S.-I. Baik, H. Kim, S. P. Park, B.-J. Park, Y. W. Kim, S. H. Lee, S.-Y. Yoon, I. C. Song, W. K. Moon, Y. D. Suh and T. Hyeon, Nonblinking and Nonbleaching Upconverting Nanoparticles as an Optical Imaging Nanoprobe and T1 Magnetic Resonance Imaging Contrast Agent, *Adv. Mater.*, **2009**, 21, 4467–4471.

18   S. H. Nam, Y. M. Bae, Y. I. Park, J. H. Kim, H. M. Kim, J. S. Choi, K. T. Lee, T. Hyeon and Y. D. Suh, Long-term real-time tracking of lanthanide ion doped upconverting nanoparticles in living cells, *Angew. Chem.*, **2011**, 50, 6093–6097.

19   W. Ren, G. Tian, S. Jian, Z. Gu, L. Zhou, L. Yan, S. Jin, W. Yin and Y. Zhao, TWEEN coated NaYF$_4$: Yb,Er/NaYF$_4$ core/shell upconversion nanoparticles for bioimaging and drug delivery., *RSC Adv.*, **2012**, 2, 7037.

20   S. Liang, X. Zhang, Z. Wu, Y. Liu, H. Zhang, H. Sun, H. Sun and B. Yang, Decoration of up-converting NaYF$_4$ Yb,Er(Tm) nanoparticles with surfactant bilayer. A versatile strategy to perform oil-to-water phase transfer and subsequently surface silication., *Cryst. Eng. Comm.*, **2012**, 14, 3484.

21   T. Pellegrino, L. Manna, S. Kudera, T. Liedl, D. Koktysh, A. L. Rogach, S. Keller, J. Rädler, G. Natile and W. J. Parak, Hydrophobic Nanocrystals Coated with an Amphiphilic Polymer Shell: A general route to water soluble nanocrystals, *Nano. Lett.*, **2004**, 4, 703–707.

22   C. Wang, H. Tao, L. Cheng and Z. Liu, Near-infrared light induced in vivo photodynamic therapy of cancer based on upconversion nanoparticles, *Biomaterials*, **2011**, 32, 6145–6154.

23   X. Li, Y. Wu, Y. Liu, X. Zou, L. Yao, F. Li and W. Feng, Cyclometallated ruthenium complex-modified upconversion nanophosphors for selective detection of Hg^{2+} ions in water, *Nanoscale*, **2014**, 6, 1020–1028.

24   G. Jiang, J. Pichaandi, N. J. J. Johnson, R. D. Burke and van Veggel, Frank C J M, An effective polymer cross-linking strategy to obtain stable dispersions of upconverting NaYF$_4$ nanoparticles in buffers and biological growth media for biolabeling applications, *Langmuir*, **2012**, 28, 3239–3247.

25   R. Abdul Jalil and Y. Zhang, Biocompatibility of silica coated NaYF$_4$ upconversion fluorescent nanocrystals, *Biomaterials*, **2008**, 29, 4122–4128.

26   M. Wang, C. Mi, Y. Zhang, J. Liu, F. Li, C. Mao and S. Xu, NIR-responsive silica-coated NaYbF$_4$:Er/Tm/Ho upconversion fluorescent nanoparticles with tunable emission colors and their applications in immunolabeling and fluorescent imaging of cancer cells, *J. Phys. Chem. C*, **2009**, 113, 19021–19027.

27   N. M. Idris, M. K. Gnanasammandhan, J. Zhang, P. C. Ho, R. Mahendran and Y. Zhang, In vivo photodynamic therapy using upconversion nanoparticles as remote-controlled nanotransducers, *Nat. Med.*, **2012**, 18, 1580–1585.

28   R. P. Bagwe, L. R. Hilliard and W. Tan, Surface modification of silica nanoparticles to reduce aggregation and nonspecific binding, *Langmuir*, **2006**, 22, 4357–4362.

29   F. Liu, Q. Zhao, H. You and Z. Wang, Synthesis of stable carboxy-terminated NaYF$_4$:Yb^{3+},Er^{3+}@SiO$_2$ nanoparticles with ultrathin shell for biolabeling applications, *Nanoscale*, **2013**, 5, 1047–1053.

30   M. Wang, C.-C. Mi, W.-X. Wang, C.-H. Liu, Y.-F. Wu, Z.-R. Xu, C.-B. Mao and S.-K. Xu, Immunolabeling and NIR-excited fluorescent imaging of HeLa cells by using NaYF$_4$:Yb,Er upconversion nanoparticles, *ACS Nano*, **2009**, 3, 1580–1586.

31   J. Liu, W. Bu, L. Pan and J. Shi, NIR-triggered anticancer drug delivery by upconverting nanoparticles with integrated azobenzene-modified mesoporous silica, *Angew. Chem. Int. Ed.*, **2013**, 52, 4375–4379.

32   K. Li, Q. Su, W. Yuan, B. Tian, B. Shen, Y. Li, W. Feng and F. Li, Ratiometric monitoring of intracellular drug release by an upconversion drug delivery nanosystem, *ACS Appl. Mater. Interfaces*, **2015**, 7, 12278–12286.

33   C. Li, Z. Hou, Y. Dai, D. Yang, Z. Cheng, P.'a. Ma and J. Lin, A facile fabrication of upconversion luminescent and mesoporous core–shell structured β-NaYF$_4$: Yb^{3+} Er^{3+}@mSiO$_2$ nanocomposite spheres for anti-cancer drug delivery and cell imaging., *Biomater. Sci.*, **2013**, 1, 213–223.

34   J. Wang, T. Wei, X. Li, B. Zhang, J. Wang, C. Huang and Q. Yuan, Near-infrared-light-mediated imaging of latent fingerprints based on molecular recognition, *Angew. Chem. Inter.l Ed.*, **2014**, 53, 1616–1620.

35   N. J. J. Johnson, N. M. Sangeetha, J.-C. Boyer and van Veggel, Frank C J M, Facile ligand-exchange with polyvinylpyrrolidone and subsequent silica coating of hydrophobic upconverting beta-NaYF$_4$:Yb^{3+}/Er^{3+} nanoparticles, *Nanoscale*, **2010**, 2, 771–777.

36   L. Tong, E. Lu, J. Pichaandi, P. Cao, M. Nitz and M. A. Winnik, Quantification of surface ligands on NaYF$_4$ nanoparticles by three independent analytical techniques, *Chem. Mater.*, **2015**, 27, 4899–4910.

37   N. Bogdan, F. Vetrone, G. A. Ozin and J. A. Capobianco, Synthesis of ligand-free colloidally stable water dispersible brightly luminescent lanthanide-doped upconverting nanoparticles, *Nano Lett.*, **2011**, 11, 835–840.

38   A. Dong, X. Ye, J. Chen, Y. Kang, T. Gordon, J. M. Kikkawa and C. B. Murray, A generalized ligand-exchange strategy enabling sequential surface functionalization of colloidal nanocrystals, *J. Am. Chem. Soc.*, **2011**, 133, 998–1006.

39   D. Ni, J. Zhang, W. Bu, H. Xing, F. Han, Q. Xiao, Z. Yao, F. Chen, Q. He, J. Liu, S. Zhang, W. Fan, L. Zhou, W. Peng and J. Shi, Dual-targeting upconversion nanoprobes across the blood-brain barrier for magnetic resonance/fluorescence imaging of intracranial glioblastoma, *ACS Nano*, **2014**, 8, 1231–1242.

40   Y.-F. Wang, G.-Y. Liu, L.-D. Sun, J.-W. Xiao, J.-C. Zhou and C.-H. Yan, Nd^{3+}-sensitized upconversion nanophosphors: efficient in vivo bioimaging probes with minimized heating effect, *ACS Nano*, **2013**, 7, 7200–7206.

41   G. Zhao, L. Tong, P. Cao, M. Nitz and M. A. Winnik, Functional PEG-PAMAM-tetraphosphonate capped NaLnF$_4$ nanoparticles and their colloidal stability in phosphate buffer, *Langmuir*, **2014**, 30, 6980–6989.

42   T. Ma, Y. Ma, S. Liu, L. Zhang, T. Yang, H.-R. Yang, W. Lv, Q. Yu, W. Xu, Q. Zhao and W. Huang, Dye-conjugated upconversion nanoparticles for ratiometric imaging of intracellular pH values, *J. Mater. Chem. C*, **2015**, 3, 6616–6620.

43   C. Wang, L. Cheng, Y. Liu, X. Wang, X. Ma, Z. Deng, Y. Li and Z. Liu, Imaging-guided pH-sensitive photodynamic therapy using charge reversible upconversion nanoparticles under near-infrared light, *Adv. Funct. Mater.*, **2013**, 23, 3077–3086.

44   Y. Li, Z. Wu and Z. Liu, An immune sandwich assay of carcinoembryonic antigen based on the joint use of upconversion phosphors and magnetic beads, *Analyst*, **2015**, 140, 4083–4088.

45   L. C. Ong, L. Y. Ang, S. Alonso and Y. Zhang, Bacterial imaging with photostable upconversion fluorescent nanoparticles, *Biomaterials*, **2014**, 35, 2987–2998.

46   P. Zhang, W. Steelant, M. Kumar and M. Scholfield, Versatile photosensitizers for photodynamic therapy at infrared excitation, *J. Am. Chem. Soc.*, **2007**, 129, 4526–4527.

47   R. Qiao, C. Liu, M. Liu, H. Hu, C. Liu, Y. Hou, K. Wu, Y. Lin, J. Liang and M. Gao, Ultrasensitive in vivo detection of primary gastric tumor and lymphatic metastasis using upconversion nanoparticles, *ACS Nano*, **2015**, 9, 2120–2129.

48   H.-D. Gao, P. Thanasekaran, C.-W. Chiang, J.-L. Hong, Y.-C. Liu, Y.-H. Chang and H.-M. Lee, Construction of a near-infrared-activatable enzyme platform to remotely trigger intracellular signal transduction using an upconversion nanoparticle, *ACS Nano*, **2015**, 9, 7041–7051.

49   Y.-H. Chien, Y.-L. Chou, S.-W. Wang, S.-T. Hung, M.-C. Liau, Y.-J. Chao, C.-H. Su and C.-S. Yeh, Near-infrared light photocontrolled targeting, bioimaging, and chemotherapy with caged upconversion nanoparticles in vitro and in vivo, *ACS Nano*, **2013**, 7, 8516–8528.

50   Z. Wang, X. Li, Y. Song, L. Li, W. Shi and H. Ma, An upconversion luminescence nanoprobe for the ultrasensitive detection of hyaluronidase, *Anal. Chem.*, **2015**, 87, 5816–5823.

51   S. Wilhelm, M. del Barrio, J. Heiland, S. F. Himmelstoß, J. Galbán, O. S. Wolfbeis and T. Hirsch, Spectrally matched upconverting luminescent nanoparticles for monitoring enzymatic reactions, *ACS Appl. Mater. Interfaces*, **2014**, 6, 15427–15433.

52   S. Wilhelm, T. Hirsch, W. M. Patterson, E. Scheucher, T. Mayr and O. S. Wolfbeis, Multicolor upconversion nanoparticles for protein conjugation, *Theranostics*, **2013**, 3, 239–248.

53   Y. Min, J. Li, F. Liu, E. K. L. Yeow and B. Xing, Near-infrared light-mediated photoactivation of a platinum antitumor prodrug and simultaneous cellular apoptosis imaging by upconversion-luminescent nanoparticles, *Angew. Chem. Inter. Ed.*, **2014**, 53, 1012–1016.

54   L.-J. Huang, X. Tian, J.-T. Yi, R.-Q. Yu and X. Chu, A turn-on upconversion fluorescence resonance energy transfer biosensor for ultrasensitive endonuclease detection, *Anal. Methods*, **2015**, 7, 7474–7479.

55   L.-J. Huang, R.-Q. Yu and X. Chu, DNA-functionalized upconversion nanoparticles as biosensors for rapid, sensitive, and selective detection of Hg^{2+} in complex matrices, *Analyst*, **2015**, 140, 4987–4990.

56   L.-L. Li, P. Wu, K. Hwang and Y. Lu, An exceptionally simple strategy for DNA-functionalized up-conversion nanoparticles as biocompatible agents for nanoassembly, DNA delivery, and imaging, *J. Am. Chem. Soc.*, **2013**, 135, 2411–2414.

57   J. Lan, F. Wen, F. Fu, X. Zhang, S. Cai, Z. Liu, D. Wu, C. Li, J. Chen and C. Wang, A photoluminescent biosensor based on long-range self-assembled DNA cascades and upconversion nanoparticles for the detection of breast cancer-associated circulating microRNA in serum samples, *RSC Adv.*, **2015**, 5, 18008–18012.

58   K. Song, X. Kong, X. Liu, Y. Zhang, Q. Zeng, L. Tu, Z. Shi and H. Zhang, Aptamer optical biosensor without bio-breakage using upconversion nanoparticles as donors, *Chem. Commun.*, **2012**, 48, 1156–1158.

59   S. Wu, N. Duan, X. Ma, Y. Xia, H. Wang and Z. Wang, A highly sensitive fluorescence resonance energy transfer aptasensor for staphylococcal enterotoxin B detection based on exonuclease-catalyzed target recycling strategy, *Anal. Chim. Acta*, **2013**, 782, 59–66.

60   S. Wu, N. Duan, Z. Shi, C. Fang and Z. Wang, Simultaneous aptasensor for multiplex pathogenic bacteria detection based on multicolor upconversion nanoparticles labels, *Anal. Chem.*, **2014**, 86, 3100–3107.

61   F. Zhou, M. O. Noor and U. J. Krull, Luminescence resonance energy transfer-based nucleic acid hybridization assay on cellulose paper with upconverting phosphor as donors, *Anal. Chem.*, **2014**, 86, 2719–2726.

62   S. Doughan, Y. Han, U. Uddayasankar and U. J. Krull, Solid-phase covalent immobilization of upconverting nanoparticles for biosensing by luminescence resonance energy transfer, *ACS Appl. Mater. Interfaces*, **2014**, 6, 14061–14068.

63   Y.-M. Wu, Y. Cen, L.-J. Huang, R.-Q. Yu and X. Chu, Upconversion fluorescence resonance energy transfer biosensor for sensitive detection of human immunodeficiency virus antibodies in human serum, *Chem. Commun.*, **2014**, 50, 4759–4762.

64   P. Alonso-Cristobal, P. Vilela, A. El-Sagheer, E. Lopez-Cabarcos, T. Brown, O. L. Muskens, J. Rubio-Retama and A. G. Kanaras, Highly sensitive DNA sensor based on upconversion nanoparticles and graphene oxide, *ACS Appl. Mater. Interfaces*, **2015**, 7, 12422–12429.

65   Z. Li, T. Liang, S. Lv, Q. Zhuang and Z. Liu, A rationally designed upconversion nanoprobe for in vivo detection of hydroxyl radical, *J. Am. Chem. Soc.*, **2015**, 137, 11179–11185.

66   Y. Ding, F. Wu, Y. Zhang, X. Liu, de Jong, Elinore M L D, T. Gregorkiewicz, X. Hong, Y. Liu, M. C. G. Aalders, W. J. Buma and H. Zhang, Interplay between Static and Dynamic Energy Transfer in Biofunctional Upconversion Nanoplatforms, J. Phys. Chem. Lett., **2015**, 6, 2518–2523.

68

67   J. Peng, W. Xu, C. L. Teoh, S. Han, B. Kim, A. Samanta, J. C. Er, L. Wang, L. Yuan, X. Liu and Y.-T. Chang, High-efficiency in vitro and in vivo detection of Zn^{2+} by dye-assembled upconversion nanoparticles, *J. Am. Chem. Soc.*, **2015**, 137, 2336–2342.

68   T. Zeng, T. Zhang, W. Wei, Z. Li, D. Wu, L. Wang, J. Guo, X. He and N. Ma, Compact, programmable, and stable biofunctionalized upconversion nanoparticles prepared through peptide-mediated phase transfer for high-sensitive protease sensing and in vivo apoptosis imaging, *ACS Appl. Mater. Interfaces*, **2015**, 7, 11849–11856.

69   H. Wang, Z. Liu, S. Wang, C. Dong, X. Gong, P. Zhao and J. Chang, MC540 and upconverting nanocrystal coloaded polymeric liposome for near-infrared light-triggered photodynamic therapy and cell fluorescent imaging, *ACS Appl. Mater. Interfaces*, **2014**, 6, 3219–3225.

70   H. Ding, Y. Lv, D. Ni, J. Wang, Z. Tian, W. Wei and G. Ma, Erythrocyte membrane-coated NIR-triggered biomimetic nanovectors with programmed delivery for photodynamic therapy of cancer, *Nanoscale*, **2015**, 7, 9806–9815.

71   Y. Liu, M. Chen, T. Cao, Y. Sun, C. Li, Q. Liu, T. Yang, L. Yao, W. Feng and F. Li, A cyanine-modified nanosystem for in vivo upconversion luminescence bioimaging of methylmercury, *J. Am. Chem. Soc.*, **2013**, 135, 9869–9876.

72   X. Zou, Y. Liu, X. Zhu, M. Chen, L. Yao, W. Feng and F. Li, An Nd^{3+}-sensitized upconversion nanophosphor modified with a cyanine dye for the ratiometric upconversion luminescence bioimaging of hypochlorite, *Nanoscale*, **2015**, 7, 4105–4113.

73   J. Rieffel, F. Chen, J. Kim, G. Chen, W. Shao, S. Shao, U. Chitgupi, R. Hernandez, S. A. Graves, R. J. Nickles, P. N. Prasad, C. Kim, W. Cai and J. F. Lovell, Hexamodal imaging with porphyrin-phospholipid-coated upconversion nanoparticles, *Adv. Mater.*, **2015**, 27, 1785–1790.

74   G. Shan, R. Weissleder and S. A. Hilderbrand, Upconverting organic dye doped core-shell nano-composites for dual-modality NIR imaging and photo-thermal therapy, Theranostics, **2013**, 3, 267–274.

75   R. Arppe, T. Näreoja, S. Nylund, L. Mattsson, S. Koho, J. M. Rosenholm, T. Soukka and M. Schäferling, Photon upconversion sensitized nanoprobes for sensing and imaging of pH, *Nanoscale*, **2014**, 6, 6837–6843.

76   T. Ma, Y. Ma, S. Liu, L. Zhang, T. Yang, H.-R. Yang, W. Lv, Q. Yu, W. Xu, Q. Zhao and W. Huang, Dye-conjugated upconversion nanoparticles for ratiometric imaging of intracellular pH values, *J. Mater. Chem. C*, **2015**, 3, 6616–6620.

77   L. Zhou, R. Wang, C. Yao, X. Li, C. Wang, X. Zhang, C. Xu, A. Zeng, D. Zhao and F. Zhang, Single-band upconversion nanoprobes for multiplexed simultaneous in situ molecular mapping of cancer biomarkers, *Nat. Commun.*, **2015**, 6, 6938.

78   J. Liu, Y. Liu, W. Bu, J. Bu, Y. Sun, J. Du and J. Shi, Ultrasensitive nanosensors based on upconversion nanoparticles for selective hypoxia imaging in vivo upon near-infrared excitation, *J. Am. Chem. Soc.*, **2014**, 136, 9701–9709.

79   S. Lu, D. Tu, P. Hu, J. Xu, R. Li, M. Wang, Z. Chen, M. Huang and X. Chen, Multifunctional nano-bioprobes based on rattle-structured upconverting luminescent nanoparticles, *Angew. Chem. Int. Ed.*, **2015**, 54, 7915–7919.

80   S. Liu, L. Zhang, T. Yang, H. Yang, K. Y. Zhang, X. Zhao, W. Lv, Q. Yu, X. Zhang, Q. Zhao, X. Liu and W. Huang, Development of upconversion luminescent probe for ratiometric sensing and bioimaging of hydrogen sulfide, *ACS Appl. Mater. Interfaces*, **2014**, 6, 11013–11017.

81   T. Wu, M. Barker, K. M. Arafeh, J.-C. Boyer, C.-J. Carling and N. R. Branda, A UV-blocking polymer shell prevents one-photon photoreactions while allowing multi-photon processes in encapsulated upconverting nanoparticles, *Angew. Chem. Int. Ed.*, **2013**, 52, 11106–11109.

82   C. Liu, W. Ma, Z. Gao, J. Huang, Y. Hou, C. Xu, W. Yang and M. Gao, Upconversion luminescence nanoparticles-based lateral flow immunochromatographic assay for cephalexin detection, *J. Mater. Chem. C*, **2014**, 2, 9637–9642.

5 PHOTOSENSITISER FUNCTIONALIZED LUMINESCENT UPCONVERTING NANOPARTICLES FOR EFFICIENT PHOTODYNAMIC THERAPY OF BREAST CANCER CELLS

5.1 Abstract

Photodynamic therapy (PDT) is a well-established treatment of cancer that involves the production of cell toxic reactive oxygen species, including singlet oxygen ($^1O_2$), by a photosensitiser drug following irradiation of a specific wavelength. Visible light is commonly used as the excitation source in PDT, although these wavelengths do have limited tissue penetration. In the research presented here, upconverting nanoparticles (UCNPs) functionalised with the photosensitiser Rose Bengal (RB) have been designed and synthesised for PDT of breast cancer cells. The use of UCNPs shifts the required excitation wavelength for the production of $^1O_2$ to near infrared light (NIR, 980 nm) thus allowing deeper tissue penetration. Highly luminescent $NaYF_4$:Yb,Er,Gd@$NaYF_4$ core-shell UCNPs were synthesised that exhibited two main anti-Stokes emission bands at 541 and 652 nm following 980 nm irradiation. RB was chosen as the photosensitiser since its absorption band overlaps with the green emission (541 nm) of the UCNPs. To achieve a high energy transfer from the nanoparticles to the photosensitiser, the functionalised UCNPs were designed to include a short l-lysine linker to attach the RB to the luminescent core yielding water dispersible RB-lysine functionalised UCNPs. The short distance between the UCNPs core and the RB allowed for an efficient Förster resonance energy transfer (FRET) from the UCNPs to the RB, which was confirmed by luminescence lifetime measurements. The light emitted by the UCNPs at 541 nm, following excitation at 980 nm, generates the $^1O_2$ via the RB photosensitiser, as confirmed using the $^1O_2$ probe 9,10-anthracenediyl-bis(methylene)dimalonic acid. Multi-photon microscopy and confocal laser scanning microscopy confirmed the internalisation of the RB-lysine functionalised UCNPs by SK-BR-3 breast cancer cells. Cell viability studies revealed that the RB-lysine functionalised nanoparticles induced low dark toxicity in SK-BR-3 cells prior to PDT treatment. However, following irradiation with NIR at 980 nm, high levels of cell death were observed in SK-BR-3 breast cancer cells loaded with the RB-lysine functionalised UCNPs. Cell death following PDT treatment was also confirmed using propidium iodide

and confocal laser scanning microscopy. The high drug loading capacity (160 RB / nanoparticle) of the UCNPs, the efficient FRET from the UCNPs to the RB photosensitiser, the high level of accumulation inside the cells and their PDT cell kill suggests that the water stable RB-lysine UCNPs are a promising alternative for PDT based cancer treatment.
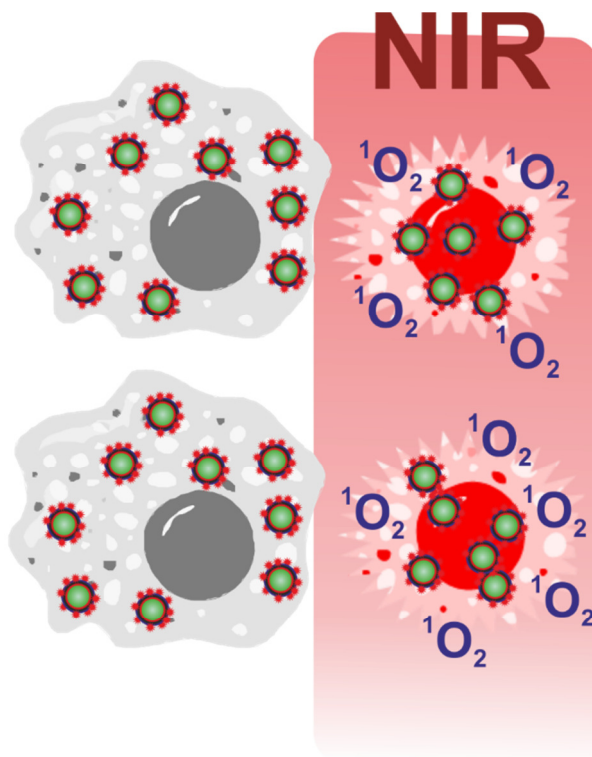

Figure 5.1‖ Scheme of upconverting nanoparticles modified with rose bengal uptaken in breast cancer cells. Following NIR excitation the modified particles produce singlet oxygen, which leads to cytotoxicity. After cell death the functionalized particles accumulate in the cell nuclei.

This chapter has been submitted.

Markus Buchner*, Paula García Calavia*, Verena Muhr, Antje Baeumner, Thomas Hirsch, María J. Marín and David A. Russell. *Submitted to Nanoscale.*

Author contributions

MB synthezised and characterized the nanoparticles. MB, PC and MM performed the cellular experiments. VM helped with preliminary tests for singulet oxygen production. MB and PC wrote the manuscript. The work was designed and supervised by AB, TH, DR. and MM. MM and TH are corresponding authors.

5.2 Introduction

Photodynamic therapy (PDT) is a treatment for cancer that involves the production of reactive oxygen species which leads to cell death. Reactive oxygen species, including singlet oxygen ($^1O_2$), are generated by the activation of a photosensitiser drug with light, typically of visible wavelengths.[1] Particularly effective photosensitisers are hydrophobic in nature, since they can be efficiently internalised by the cells through interaction with the lipid layers of the cell membrane.[2,3] However, such hydrophobicity restricts the delivery and transportation of the photosensitisers through the body.[2,4] Another issue with photosensitisers that are activated with visible light is the difficulty to treat deep-lying tumours.[5] Therefore, improvements for the extended use of PDT in the clinical environment include the development of photosensitiser delivery systems that can provide aqueous solubility, as well as the use of excitation wavelengths in the near-infrared (NIR) region that can increase tissue penetration.

Upconverting nanoparticles (UCNPs) have attracted considerable interest as delivery vehicles for photodynamic therapy.[5] UCNPs convert NIR light to ultraviolet (UV) and visible light, which can then be used for the excitation of photosensitisers placed near the surface of the UCNPs.[5] The use of NIR light has several advantages over UV and visible light, including deeper penetration into biological tissue,

reduced photodamage upon long-term irradiation, increased photostability and low autofluorescence.[5-8] UCNPs are commonly prepared with lanthanide ions, which are embedded in a crystalline host lattice.[9] Such a host lattice is physically and chemically stable and requires low phonon energies,[10] so that non-radiative loss can be minimised while the upconverted emission is maximised.[7,9,11] The lanthanide dopants typically consist of ytterbium (Yb^{3+}) ions as sensitiser ions, which can absorb the NIR light and transfer two or more photons to the so-called emitting ions (e.g. erbium (Er^{3+}), holmium (Ho^{3+}) and thulium (Tm^{3+}) ions), yielding anti-Stokes emissions.[7,9,11]

Thermolysis, Ostwald ripening and a hydrothermal strategy are the three main synthetic methods for UCNPs.[6] Depending on the performed synthesis, several surface modifications are necessary either to enhance the colloidal stability of the nanoparticles or to provide functional groups on the surface of the particles for coupling with other ligands such as biomolecules and/or photosensitisers.[6,12,13] The most important consideration when using UCNPs for PDT is the overlap between the luminescence emission of the UCNPs and the absorption of the photosensitiser, enabling an activation of the photosensitiser by the NIR light.[5] Therefore, the surface modification and functionalisation of the UCNPs with the photosensitiser is critical to achieve efficient photodynamic

therapy.[14] Several surface modifications and functionalisation methods have been explored. The first reports of UCNPs for PDT involved the coating of the UCNPs with an amorphous silica layer, to which the photosensitiser was embedded.[15,16] Despite the promising results obtained, the silica coating was found to present various limitations, including the low loading of the photosensitiser due to its weak interaction with the silica, the low stability of silica in aqueous solutions and the restricted site of action of singlet oxygen, which is unable to be efficiently released from the silica layer.[17,18] These limitations could be improved by covalent conjugation of the photosensitiser to the silica layer,[17] or by the use of mesoporous silica ($mSiO_2$), which further improves the aqueous solubility of the system and increases the PDT efficacy due to an improved release of $^1O_2$.[18,19] The addition of an extra outer layer made of a cross-linked lipid to the $mSiO_2$-UCNPs is a further advantage to avoid the leaking of the photosensitiser from the silica layer.[20]

The use of hydrophilic and amphiphilic polymers have also been widely studied. Polyethylene glycol (PEG) is one such polymer that can induce water solubility and biocompatibility with good results in NIR-PDT, either used by itself,[21] or as a copolymer.[22-24] The addition of PEG has also been reported to increase the stability in a system where the photosensitiser was deposited as a layer around the UCNPs.[25] An additional advantage of PEG is its use as a linker for targeting molecules, such as folic acid.[26] Other polymers that have been used to modify the surface of UCNPs in PDT include polyethyleneimine,[27] chitosan,[28,29] and a polymeric liposome made of three amphiphilic polymers.[30] The modification of oleate-capped UCNPs with a cyclic oligosaccharide, α-cyclodextrin, yielded water stable and biocompatible UCNPs useful for PDT.[31] A new synthetic approach applying nucleotides to render water dispersible UCNPs without the need of ligand exchange surface modification has been reported by Zhou *et al.*.[32]

A significant problem with the current functionalisation methods is the increase in the distance between the emitting ions in the UCNPs and the photosensitisers, due to the inclusion of the extra layer of either silica or polymers between the two.[33] The distance between the surface of the UCNPs and the photosensitiser needs to be considered as an important parameter, since the energy transfer efficiency is distance-dependent; it decreases proportionally to the sixth power of the distance between the donor and the acceptor species.[33,34] As a result, the efficiency of $^1O_2$ production and thus photodynamic therapy is reduced.

Here, we report the synthesis of a novel nanoplatform that includes small and bright UCNPs modified with a short biocompatible linker molecule, lysine, to which the photosensitiser Rose Bengal (RB) was covalently attached (**Figure 5.2**). The constructed nanoparticles exhibit structural advantages including: 1) high drug loading on the surface of the nanoparticles; 2) short distance between the nanoparticle and the photosensitiser; and 3) colloidal stability. The reported Rose Bengal (RB)-lysine functionalised UCNPs generated singlet oxygen *via* efficient Förster resonance energy transfer (FRET) between the UCNP and the photosensitiser.
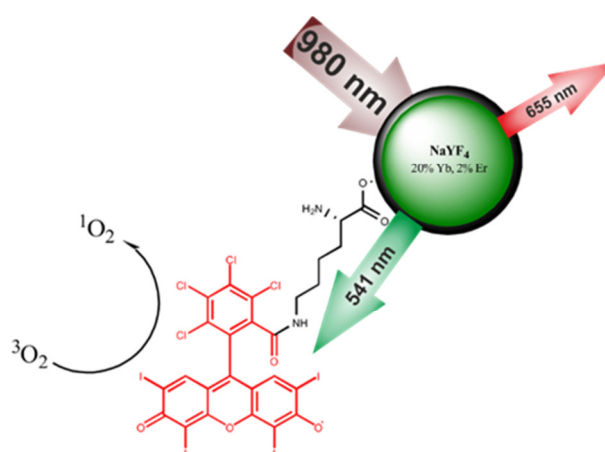

Figure 5.2║ Schematic representation of the Rose Bengal – lysine functionalised UCNPs used for photodynamic therapy of breast cancer cells. The UCNPs (green) were excited at 980 nm to produce luminescence emission at 541 nm that was used by Rose Bengal (red molecule) to produce singlet oxygen ($^1O_2$), toxic for cancer cells.

The use of the UCNPs for photodynamic therapy of cancer was investigated *in vitro* using SK-BR-3 human breast cancer cells. The RB-lysine functionalised UCNPs were internalised by the SK-BR-3 cells as demonstrated using confocal laser scanning microscopy and multi-photon microscopy. Furthermore, cell viability and cytotoxicity studies performed before and after PDT treatment confirmed the high efficiency of the RB-lysine functionalised UCNPs for PDT of cancer.

5.3 Experimental

Materials

All of the reagents were of analytical grade, purchased from Sigma-Aldrich (UK), unless otherwise stated, and used as received. Sodium dihydrogen orthophosphate dihydrate ($NaH_2PO_4 \cdot 2H_2O$), sodium chloride (NaCl), phosphate buffered saline (PBS) tablets, foetal bovine serum, 75 cm^2 Nunc Easy tissue culture flasks with porous caps, Nunc multidishes, Nunc Nunclon™ Δ Surface 96-well white-bottom microplates and 18 mm diameter glass coverslips were purchased from Thermo Fisher Scientific, UK. Trypsin 0.25% (1x) with ethylenediaminetetraacetic acid (EDTA) and McCOY's 5A phenol red free medium containing L-glutamine were purchased from Invitrogen, UK. CellTiter-Blue® cell viability assay was purchased from Promega, UK. Millex GP syringe driven filter units (0.22 μm) were purchased from Millipore Corporation, USA. Sodium hydrogen carbonate ($NaHCO_3$) was purchased from BDH Laboratory Supplies Poole, UK. SK-BR-3 human breast adenocarcinoma cells were purchased from LGC Standards. The SK-BR-3 cell line was kindly provided by Prof Dylan R. Edwards (Norwich Medical School, University of East Anglia, UK). Ammonium fluoride (≥98%), Rose Bengal (95%), erbium(III) chloride hexahydrate (99.9%), N-hydroxysuccinimide (NHS, 98%), N-(3-dimethylaminopropyl)-N′-ethylcarbodiimide hydrochloride (EDC, 98%) and nitrosyl tetrafluoroborate (95%) were purchased from Sigma Aldrich. 1-Octadecene (90%) and oleic acid (90%) were bought from Alfar Aesar. Sodium hydroxide (98-100%) and dimethyl sulfoxide (DMSO, 99.9%) were purchased from Merck. Cyclohexane (99.5%), dimethylformamide (DMF, 99.5%), and chloroform (99.8%) were obtained from Acros Organics. Yttrium chloride hexahydrate (99.99%), ytterbium(III) chloride hexahydrate (99.99%) and gadolinium chloride hexahydrate (99.99%) were bought from Treibacher Industrie AG (www.treibacher.at). L-lysine (98.5-101.5%) was purchased from SERVA.

Instrumental

The size of the nanoparticles was investigated with dynamic light scattering (DLS) and transmission electron microscopy (TEM). DLS-measurements were performed on a Zetasizer Nano ZS (Malvern) in semi-micro disposable Poly(methyl methacrylate) (PMMA) cuvettes. For particles dispersed in DMF and DMSO precision cells made of quartz glass Suprasil from Hellma were used. A 120 kV Philips CM12 microscope (MicroCal) was used to generate TEM images. They were analysed with ImageJ/Origin 8. Lifetime measurements were performed with 980 nm (cw, 200 mW) laser module and an optical chopper (MC2000 with two-slot chopper blade MC1F2) from Thorlabs. The signal was

amplified by a photomultiplier tube and analysed by a digital storage oscilloscope (DSO 8204) from Voltcraft. Optical bandpass filters (FF01-535/150-25 and FF01-665/150-25) from Semrock were used for measuring luminescence decay times for the green (541 nm) and the red emission (656 nm). Fourier transform infrared spectroscopy (FTIR) measurements were performed on a Carry 630 FTIR spectrometer (Agilent Technologies). The luminescence spectra were recorded on a luminescence Aminco Bowman Series 2 spectrometer (Thermo Electron Corporation) coupled with a cw laser (980 nm, 200 mW). Inductively coupled plasma optical emission spectrometer (ICP-OES) measurements were performed on an inductively coupled plasma optical emission spectrometer from Spectro.

Multi-photon microscopy was achieved using a TriM Scope II multi-photon microscope (LaVision BioTec, Bielefeld, Germany). The images were acquired with a 63x/1.4 NA PlanApochromat objective lens (Carl Zeiss Ltd., Cambridge, UK) and processed using ImspectorPro and ImageJ/Fiji software. Laser scanning confocal microscopy images of SK-BR-3 cells were obtained using a Carl Zeiss LSM 510 META microscope. The images were acquired with a plan-apochromat 63x/1.4 Oil DIC objective and processed using the Zeiss LSM Image Browser software. To perform the cell viability assays, the samples were excited at 561 nm and the fluorescence emission was measured at 594 nm using a CLARIOstar® (BMG Labtech) microplate reader.

Methods

Synthesis of β-NaYF$_4$:Yb,Er,Gd core nanoparticles. The synthesis of Ln^{3+} doped NaYF$_4$ (20% Yb, 20% Gd, 2% Er) upconversion nanoparticles is based on a reported procedure.[35] The following description is for a 5 mmol approach of total lanthanide and rare earth chlorides. The synthesis was performed in a 250 mL three-neck round bottom flask under nitrogen flow. 387.5 mg YbCl$_3$·6H$_2$O (1 mmol), 371.7 mg GdCl$_3$·6H$_2$O (1 mmol), and 38.2 mg ErCl$_3$·6H$_2$O (0.1 mmol) were dissolved in 20 mL of methanol together with 879.7 mg YCl$_3$·6H$_2$O (2.9 mmol). 40 mL of oleic acid and 75 mL of octadecene were added and the cloudy solution was heated up to 160 °C using a heating mantle with temperature control. The reaction mixture was stirred for 30 min in vacuo at 160 °C to obtain a clear solution of the oleate precursors and then was cooled down to room temperature. Afterwards, a solution of 0.740 g NH$_4$F (20.0 mmol) and 0.5 g of NaOH (12.5 mmol) in 20 mL of methanol was added. The white suspension was heated up to 120 °C for 30 min to remove the methanol. The clear solution was heated to reflux (about 320 °C) to induce the growth of the nanoparticles. As soon as the temperature reached 300 °C, a timer was started and the occurring luminescence of the upconversion nanoparticles was controlled with 980 nm laser module (200 mW, cw). After the first

luminescence was visible (10 min) the nanoparticles were stirred for another 10 min for growth and self-focusing (Ostwald ripening). The dispersion was cooled down to room temperature and the particles were precipitated by addition of ethanol (ca. 200 mL). The white particles were collected by centrifugation (1,000 g, 5 min). The precipitate was dispersed twice in 20 mL chloroform and precipitated again with ethanol (ca. 200 mL). This washing step was repeated with cyclohexane and acetone three times until a clear dispersion of the nanoparticles in cyclohexane was obtained. In a last step the particles were dissolved in 20 mL cyclohexane and salt/aggregates were separated by centrifugation (1,000 g, 3 min). The supernatant containing the β-NaYF$_4$:Yb,Er,Gd core nanoparticles is stored at 4 °C for further usage.

Synthesis of α-NaYF$_4$ nanoparticles. The synthesis was performed in a three-neck round bottom flask under nitrogen flow. 1516.8 mg YCl$_3$·6H$_2$O (5 mmol) was dissolved in 10 mL methanol. 40 mL of oleic acid and 75 mL of octadecene were added and the cloudy solution was heated up to 160 °C by a heating mantle with temperature control. The reaction mixture was stirred for 30 min in vacuo at 160 °C in order to obtain a clear solution of the oleate coordinated particles. Afterwards, a solution of 0.740 g NH$_4$F (20.0 mmol) and 0.5 g of NaOH (12.5 mmol) in 20 mL methanol was added at room temperature. The white suspension was heated up to 120 °C for 30 min to remove the methanol. The solution was heated to 240 °C to induce the growth of the nanoparticles. After 30 min the dispersion was cooled down to room temperature and the particles were purified as described for the β-NaYF$_4$:Yb,Er,Gd core nanoparticles.

Synthesis of NaYF$_4$:Yb,Er,Gd@NaYF$_4$ core-shell nanoparticles. The synthesis was performed in three-neck round bottom flasks under nitrogen flow. In the first flask 2 mmol of the β-NaYF$_4$:Yb,Er,Gd core particles were heated together with 5 mL oleic acid and 5 mL octadecene to 120 °C. The second one contains 0.5 mmol of the α-NaYF$_4$ shell-material dispersed in cyclohexane and was heated with 2.5 mL oleic acid and 2.5 mL octadecene also to 120 °C. Both dispersions were stirred for 30 min in vacuo at 160 °C to remove the cyclohexane. While the mixture of the β-NaYF$_4$:Yb,Er,Gd core particles was heated up to 325 °C under reflux cooling, the shell material, α-NaYF$_4$ nanoparticles, was kept at 120 °C. The shell material was injected stepwise (0.5, 1, 1.5 and 2 mL) through a septum to the core particles. The time interval between each injection was 10 min. During the injection of the shell material the temperature should be above 300 °C to obtain a homogeneous shell growth. After the last injection, the NaYF$_4$:Yb,Er,Gd@NaYF$_4$ core-shell nanoparticles were stirred for another 10 min at reflux and then cooled down to room temperature. The core-shell nanoparticles were purified as described for the β-NaYF$_4$:Yb,Er,Gd core nanoparticle.

Preparation of uncapped core-shell nanoparticles (BF$_4^-$ capped nanoparticles). For the preparation of uncapped NaYF$_4$ nanoparticles, a ligand exchange method was used. Equal volumes of cyclohexane, containing the oleate capped upconversion nanoparticles and DMF were stirred at 30 °C. Nitrosyltetrafluoroborate (NOBF$_4$) was added directly into the stirring solution (1 mg NOBF$_4$ for 1 mg nanoparticle). After 15 min of stirring at 30 °C, the upper phase (cyclohexane) was removed and the DMF phase was washed with an excess of chloroform (20 mL). After being centrifuged (1,000 g, 5 min), the jelly-like precipitate was dispersed in 2-3 mL DMF and washed with chloroform (20 mL). Finally, the BF$_4^-$ capped nanoparticles were dispersed in 2-3 mL of DMF and the aggregates were separated by centrifugation (1,000 g, 3 min).

Preparation of L-lysine capped core-shell nanoparticles. 6 mg L-lysine was solved in 2 mL double distilled water and was heated up to 30 °C. 20 mg of BF$_4^-$ capped nanoparticles were added to the solution and the dispersion was stirred for 15 min. The particles were centrifuged (21,000 g, 30 min) and redispersed in water under sonication twice. The particles were dispersed in 2 mL double distilled water.

Preparation of Rose Bengal (RB) modified core-shell nanoparticles. 8 mg Rose Bengal (RB, 8 µmol) was activated with 10 mg EDC (50 µmol) and 10 mg NHS ester (87 µmol) in 2 mL MES (pH 5.5, 50 mM) buffer for 2 h at room temperature. 20 mg of lysine modified core-shell nanoparticles were added and stirred for another 2 h. The RB modified core-shell nanoparticles were purified via centrifugation (21,000 g, 30 min) three times until the supernatant was clear. The particles were dispersed in 4 mL DMSO.

ICP-OES measurements. A known amount of lanthanide doped NaYF$_4$ nanoparticles (approximately 0.3 mg) were dried at 70 °C in the oven. The dry sample was dissolved in 417 µL of sulfuric acid (96%) supported by 15 min of sonication. The solution was first diluted with double distilled water to 7.5 mL and afterwards with 1 M nitric acid to 15 mL. The emission wavelengths for the lanthanide ions were 363.312 nm for yttrium, 342.247 nm for gadolinium, 349.910 nm for erbium and 401.225 nm for ytterbium.

Estimation of the dye-loading. The dye loading on the Rose Bengal modified core-shell nanoparticlesparticles was estimated using UV-Vis absorption spectroscopy ($\varepsilon_{RB} = 90,400 \cdot M^{-1} cm^{-1}$). The number of dye molecules was divided by the number of nanoparticles calculated by ICP-OES measurements and the density of NaYF$_4$ (3.87 g·cm^{-3}).[36]

Monitoring of singlet oxygen production. The generation of singlet oxygen was monitored with 9,10-anthracenediyl-bis(methylene)dimalonic acid (ABMA, 1 µM), a molecular probe for singlet oxygen. The mass concentration of the nanoparticles was 0.55 mg·mL^{-1} dispersed in either DMSO or in McCOY's 5A phenol red-free cell culture medium. The nanoparticles were mixed with ABMA and the solution was placed in a stoppered quartz cuvette. The sample was irradiated with a 980 nm NIR laser (cw, 200 mW) for 40 min. The fluorescence emission intensity of ABMA was monitored every 5 min between 390 – 550 nm (λ_{exc} = 380 nm).

Biological experiments

Imaging medium. The imaging medium based on Hank's balanced salt solution (HBSS) was prepared in water containing NaCl (120 mM), KCl (5 mM), $CaCl_2 \cdot 2H_2O$ (2 mM), $MgCl_2 \cdot 6H_2O$ (1 mM), $NaH_2PO_4 \cdot 2H_2O$ (1 mM), $NaHCO_3$ (1 mM) and 4-(2-hydroxyethyl)piperazine-4-ethanesulfonic acid (HEPES, 25 mM); and supplemented with bovine serum albumin (1 mg·mL^{-1}) and glucose (11 mM). The pH of the imaging medium was adjusted to 7.2 using aqueous solutions of NaOH (1 M) and HCl (0.6 M). Prior to use, the imaging medium was sterilised by filtration through a 0.22 µm filter unit.

Phosphate buffer saline (PBS). The phosphate buffered saline solution used for the cell-based experiments was prepared by dissolving 10 PBS tablets in water (1 L). The solution was sterilised by autoclaving at 110 °C for 10 min. The as-prepared PBS solution contained Na_2HPO_4 (8 mM), KH_2PO_4 (1 mM), NaCl (160 mM) and KCl (3 mM); and had a pH value of 7.3.

Propidium iodide solution in PBS. A solution of propidium iodide (1 mg·mL^{-1}) was prepared in PBS. The PBS buffer (10 mM) used to dissolve the propidium iodide was prepared using $NaH_2PO_4 \cdot 2H_2O$ and Na_2HPO_4 stock solutions (200 mM). The as-prepared PBS solution contained NaCl (150 mM) and calcium chloride dihydrate (100 µM). The pH of the PBS was adjusted to 7.4 using aqueous solutions of NaOH (1 M) and HCl (0.6 M). The propidium iodide solution was sterilised by filtration through a 0.22 µm filter unit.

SK-BR-3 cell culture. SK-BR-3 human breast adenocarcinoma cells were cultured in McCOY's 5A phenol red free medium supplemented with 10% foetal bovine serum. The cells were routinely cultured at 37 °C in a 5% CO_2 atmosphere in 75 cm^3 Nunc Easy tissue culture flasks with porous caps. Subcultures (1:4) were made every 5 days by washing the cells with PBS and dislodging the cells from the flask surface using trypsin 0.25% (1x) EDTA.

Culture of SK-BR-3 cells onto coverslips. The SK-BR-3 cells were cultured at 37 °C in a 5% CO_2 atmosphere in a 75 cm^3 tissue culture flask until they reached near confluence. Following incubation, the cells were washed with PBS and harvested from the flask using trypsin as described previously. A sterile 18 mm diameter glass coverslip was placed in each well of a 6-well Nunc multidish. An aliquot of SK-BR-3 cells (3 mL, $2 \cdot 10^4$ cells·mL^{-1}) was added to each well covering the coverslip. The cells were incubated at 37 °C in a 5% CO_2 atmosphere for ca. 48 h.

CellTiter-Blue® cell viability assay. For the viability assays, SK-BR-3 cells were seeded on two 96-well white-bottom microplates ca. 48 h prior to treating the cells. The cells were cultured at 37 °C in a 5% CO_2 atmosphere in a 75 cm^3 tissue culture flask until they reached near confluence. At this point, the cells were washed with PBS and harvested from the flask using trypsin 0.25% (1x) EDTA as described previously. The cells were counted with a Neubauer haemocytometer and seeded at a density of $20 \cdot 10^4$ cells/mL (100 µL/well). The cells were incubated at 37 °C in a 5% CO_2 atmosphere for ca. 48 h. Following incubation, the cells were washed once with PBS (100 µL). The functionalised UCNPs (50 µL), at concentrations ranging between 10 – 20 µg·mL^{-1}, in McCOY's 5A phenol red free medium containing 0.25% DMSO were added to the wells. Cells without nanoparticles loaded were used as a control. A positive control for cytotoxicity, consisting of a solution of staurosporine (1 mM in DMSO) dispersed in McCOY's 5A phenol red free medium (50 µL; 20 µM), was also used. A control for the effect of DMSO was also performed by treating the cells on the well with McCOY's 5A phenol red free medium containing 0.25% DMSO. The cells were incubated with the UCNPs or the corresponding controls for 3 h at 37 °C in a 5% CO_2 atmosphere. Following incubation, the cells were washed three times with PBS (100 µL) and kept in McCOY's 5A phenol red free medium supplemented with 10% foetal bovine serum (100 µL). One of the 96-well microplates was irradiated using the 980 nm NIR laser (200 mW, Picotronic) for 6 min per well. The laser was located 50 mm above the 96-well microplate. The other 96 well microplate, which was not irradiated, was covered in aluminium foil in the dark. Following irradiation, the cells were further incubated for ca. 48 h at 37 °C in a 5% CO_2 atmosphere. CellTiter-Blue® reagent (20 µL) was added to each well and incubated with the cells for 4 h at 37 °C in a 5% CO_2 atmosphere. The fluorescence emission of the CellTiter-Blue® reagent was then measured at 594 nm following excitation at 561 nm using a CLARIOstar® (BMG Labtech) microplate reader. Background fluorescence was corrected by subtracting fluorescence emission from McCOY's 5A phenol red free medium. Cell viability was calculated as a percentage of non-treated, non-irradiated cells. All samples were analysed in triplicates.

Treatment of SK-BR-3 cells to study cellular internalisation of the Rose Bengal functionalised UCNPs. The SK-BR-3 cells on the coverslip were washed once with PBS (1 mL). For cells treated with the modified UCNPs, a solution of the functionalised UCNPs (1 mL, 25 μg·mL^{-1}) in McCOY's 5A phenol red free medium containing 0.25% DMSO was added to the coverslip. For control cells, 1 mL of McCOY's 5A phenol red free medium was added to the coverslip. The cells were incubated for 3 h at 37 °C in a 5% CO_2 atmosphere. Following incubation, the cells were washed three times with PBS (1 mL) and kept in McCOY's 5A phenol red free medium supplemented with 10% foetal bovine serum (2 mL). Subsequently, the cells were imaged using the multi-photon and the laser scanning confocal microscopes.

Treatment of SK-BR-3 cells to evaluate the PDT effect. The SK-BR-3 cells on the coverslip were washed once with PBS (1 mL). For cells treated with the functionalised UCNPs, a solution of the functionalised UCNPs (1 mL, 15 μg·mL-1) in McCOY's 5A phenol red free medium containing 0.25% DMSO was added to the coverslip. For control cells, 1 mL of the McCOY's 5A phenol red free medium containing 0.25% DMSO was added to the coverslip. The cells were incubated for 3 h at 37 °C in a 5% CO_2 atmosphere. Following incubation, the cells were washed three times with PBS (1 mL) and kept in McCOY's 5A phenol red free medium supplemented with 10% foetal bovine serum (2 mL). The 'irradiated cells' were irradiated for 6 min per coverslip using a 980 nm near infrared (NIR) laser (200 mW, Picotronic) placed 50 mm above the lid of the 6-well Nunc multidish. A NIR detector card was placed under the well containing the coverslip during the irradiation of the sample to be able to place the laser light at the centre of the treated coverslip. Both the irradiated and the non-irradiated SK-BR-3 cells were further incubated at 37 °C in a 5% CO_2 atmosphere for ca. 24 h until the sample was imaged using the laser scanning confocal microscope.

Incubation of SK-BR-3 cells with propidium iodide. Propidium iodide (5 μL, 1 mg·mL^{-1} in PBS) was mixed with HBSS-based imaging medium (1 mL). The solution was directly added to the coverslip that had been previously placed in a Ludin chamber for imaging (Life Imaging Service, Olten, Switzerland) and incubated at 37 °C in the dark on a heating stage of a Carl Zeiss LSM 510 META microscope for ca. 5 min.

Imaging of treated SK-BR-3 cells using a multi-photon microscope. For imaging, 18 mm coverslips containing the SK-BR-3 cells of interest were placed in a Ludin chamber, which was securely tightened. Each coverslip was washed three times with HBSS-based imaging medium and the Ludin chamber was mounted on a heating stage at 37 °C in a TriM Scope II multi-photon microscope. The samples were excited with an

880 nm laser using a Vision II Ti: Sapphire laser (Coherent Ltd., Ely, UK) to collect the emission of the RB (green channel, 550 ± 42.5 nm) and the differential interference contrast (DIC). To collect the luminescence of the UCNPs the sample was excited at 980 nm using the Vision II Ti:Sapphire laser with the emission collected with two non-descanned GaAsP detectors. The luminescence was measured in the green (550 ± 42.5 nm) and red (655 ± 20 nm) channels.

Imaging of treated SK-BR-3 cells using a laser scanning confocal microscope. For imaging, 18 mm coverslips containing the SK-BR-3 cells of interest were placed in a Ludin chamber, which was securely tightened. Each coverslip was washed three times with HBSS-based imaging medium and the Ludin chamber was mounted on a heating stage at 37 °C in a Carl Zeiss LSM 510 META microscope. A 543 nm HeNe laser was used to excite either the RB on the surface of the UCNPs or the propidium iodide with the emission collected between 560 – 615 nm in the red channel. DIC images were collected together with fluorescence images. DIC images were recorded with transmitted light at 488 nm using an argon-ion laser.

5.4 Results

5.4.1 Synthesis and characterisation of oleate-capped NaYF$_4$:Yb,Er,Gd@NaYF$_4$ core-shell upconverting nanoparticles

The aim was to synthesise small, highly luminescent nanoparticles that could be readily uptaken by cells for PDT of cancer. Here, monodisperse β-NaYF$_4$ nanoparticles doped with Yb^{3+}, Gd^{3+} and Er^{3+} (β-NaYF$_4$:Yb,Er,Gd core upconverting nanoparticles) were synthesised as the core material in high temperature boiling solvents following an Ostwald ripening strategy.[6] The size of the core-nanoparticles was determined by TEM. Analysis of the TEM images indicated that the synthesised core UCNPs had a uniform shape and an average diameter of 16.2 ± 0.6 nm (**Figure 5.3A-B**).
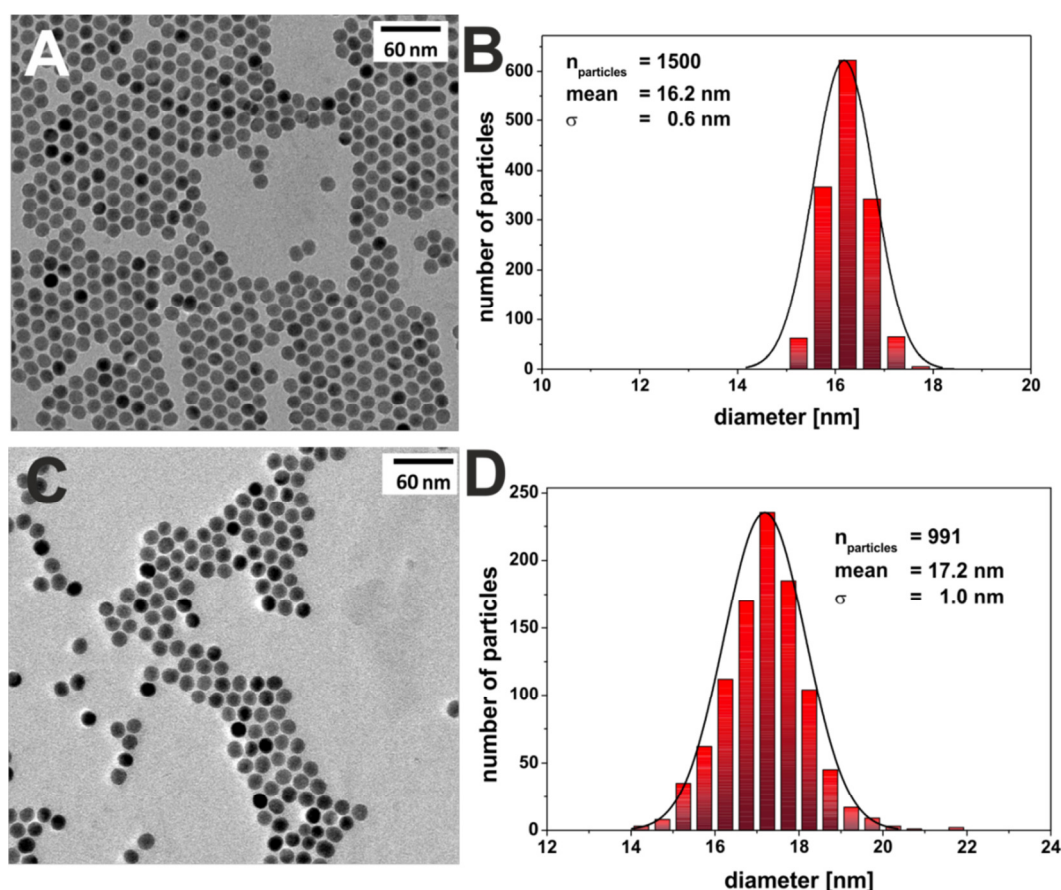

Figure 5.3 ‖ The size of the β-NaYF$_4$:Yb,Er,Gd core nanoparticles was determined to be 16.2 nm considering the TEM image (**A**) and the corresponding histogram (**B**) of the particle-size-distribution with a standard-deviation of the particles of 0.6 nm (n = 1500). **C**) TEM-image of a sample of oleate-capped NaYF$_4$:Yb,Er,Gd@NaYF$_4$ core-shell nanoparticles. **D**) Histogram of the particle-size distribution of oleate-capped NaYF$_4$:Yb,Er,Gd@NaYF$_4$ core-shell nanoparticles with an average size of 17.2 ± 1.0 nm (n = 991). Scale bar for the TEM images was 60 nm.

To achieve upconverting nanoparticles with an enhanced luminescence intensity, an inert shell was grown around the core nanoparticles. Cubic α-NaYF$_4$ upconverting nanoparticles with a size of 2 – 3 nm (**Figure 5.4**) were synthesised and used as shell precursors. The α-NaYF$_4$ upconverting nanoparticles were injected stepwise to a solution of β-NaYF$_4$:Yb,Er,Gd core UCNPs that was kept at 325 °C. After injection to the core particles, the cubic α-NaYF$_4$ UCNPs dissolved and deposited in a hexagonal crystal lattice on the core UCNPs resulting in the oleate-capped NaYF$_4$:Yb,Er,Gd@NaYF$_4$ core-shell UCNPs.[37]
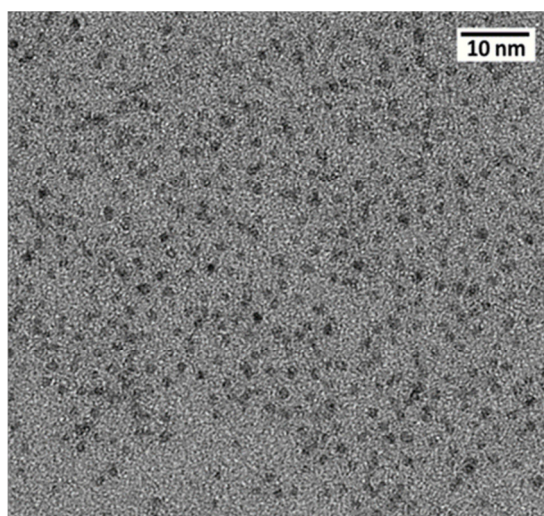

Figure 5.4‖ The size of the α-NaYF$_4$ nanoparticles was estimated to 2 – 3 nm according TEM images. The particles were dispersed in cyclohexane.

As expected, following addition of the shell material to the core nanoparticles, the size of the nanoparticles increased, as shown by the TEM images, from 16.2 ± 0.6 nm (β-NaYF$_4$:Yb,Er,Gd core UCNPs) to 17.2 ± 1.0 nm (**Figure 5.3C-D**, NaYF$_4$:Yb,Er,Gd@NaYF$_4$ core-shell UCNPs). DLS measurements of both core and core-shell UCNPs also indicated an increase in the solvodynamic diameter, from 17.8 ± 2.6 nm to 21.1 ± 3.1 nm, following formation of the shell (**Figure 5.5**).
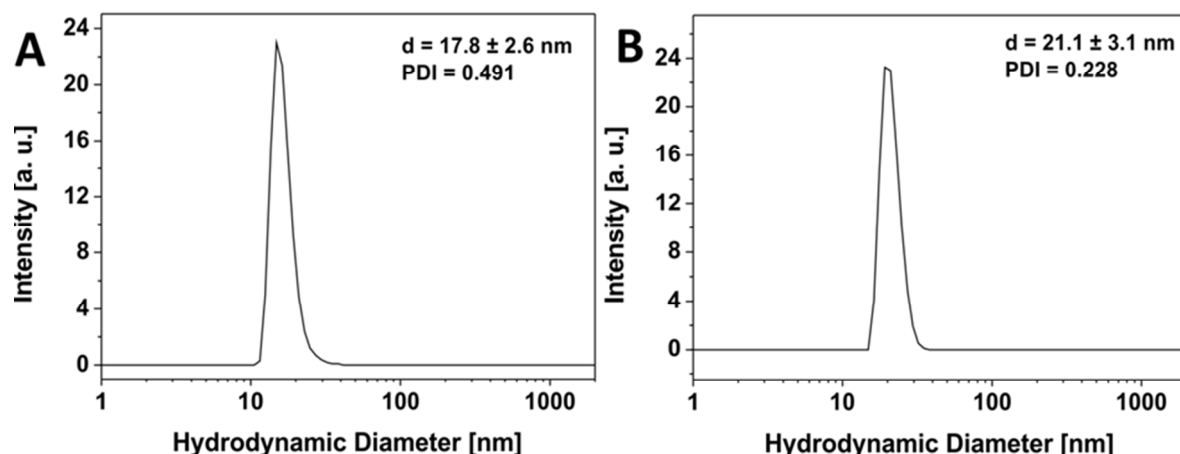
Figure 5.5‖ DLS measurements of the core, β-NaYF$_4$:Yb,Er,Gd, (**A**) and the core-shell, β-NaYF$_4$:Yb,Er,Gd@NaYF$_4$, nanoparticles (**B**) were performed in cyclohexane. The curve shows the DLS signal weighted for number with a solvodynamic diameter of 17.8 ± 2.6 nm (**A**) and 21.1 ± 3.1 nm (**B**). The polydispersity index (PDI) was 0.491 for the core particles and 0.228 for the core-shell nanoparticles.

The analysis of the composition of the core and core-shell nanoparticles by ICP-OES showed an increase in the Y^{3+} content concomitant with a decrease of the other Ln^{3+} ions from core to core-shell nanoparticles (**Table 5.1**).

Table 5.1‖ The concentration and the composition of the β-NaYF$_4$:Yb,Er,Gd (16.2 nm) core and of the NaYF$_4$:Yb,Er,Gd@NaYF$_4$ (17.2 nm) core-shell nanoparticles were determined by ICP-measurements (N = 3).

Composition [%]	Y^{3+}	Gd^{3+}	Er^{3+}	Yb^{3+}
Core particles	59.0	20.3	1.0	19.7
Core-Shell particles	68.1	16.4	0.9	14.4

The luminescence spectrum of the β-NaYF$_4$:Yb,Er,Gd core UCNPs recorded following NIR excitation at 980 nm exhibited two main anti-Stokes emission bands subsequently referred to as the green emission ($^4S_{3/2} \rightarrow {}^4I_{15/2}$) at 541 nm and the red emission ($^4F_{9/2} \rightarrow {}^4I_{15/2}$) at 652 nm (**Figure 5.6A**). The luminescence spectrum of the oleate-capped NaYF$_4$:Yb,Er,Gd@NaYF$_4$ core-shell UCNPs following excitation at 980 nm exhibited also the green and red emission bands at 541 nm and 652 nm, respectively. A comparison of the luminescence intensities of the core and core-shell nanoparticles following NIR irradiation at 980 nm shows an increase by a factor of 10 when the shell was present. The inactive inert shell minimises surface defects and solvent quenching effects.[34,38] To achieve high-energy transfer efficiency, a short distance should separate the emitting ions in the UCNPs from the photosensitiser. The short separation distance was achieved by depositing a lysine shell of small *ca.* 1 nm thickness.
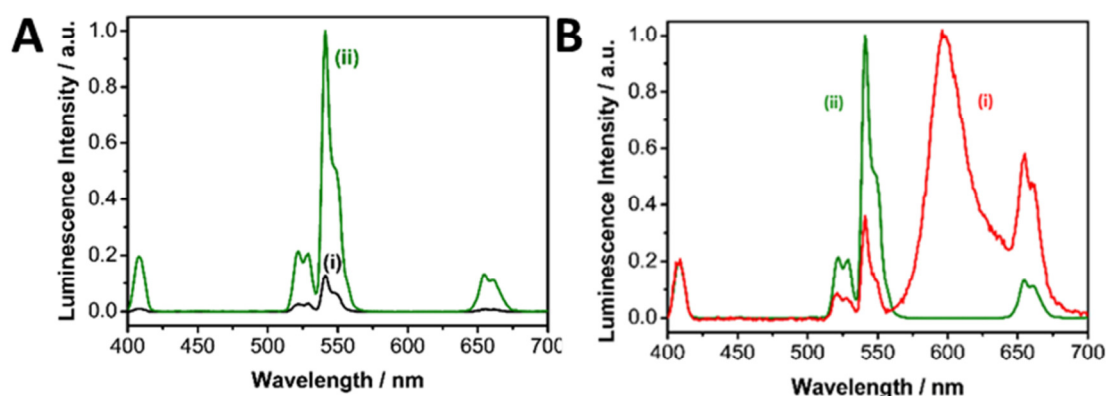
Figure 5.6‖ Luminescence spectrum of the a)(i) oleate capped β-NaYF$_4$:Yb,Er,Gd core nanoparticles, **A**)(ii) and **B**)(ii) NaYF$_4$:Yb,Er,Gd@NaYF$_4$ core-shell nanoparticles and **B**)(i) RB@lysine functionalised NaYF$_4$:Yb,Er,Gd@NaYF$_4$ core-shell nanoparticles. The spectra were recorded in cyclohexane (**A** and **B**(ii)) and DMSO (B(i)) following excitation at 980 nm (cw 200 mW). In **A**) the spectra were normalized to a Yb^{3+} concentration of 5 mM (determined by ICP-OES).

5.4.2 Synthesis and characterisation of the RB–lysine functionalised NaYF$_4$:Yb,Er,Gd@NaYF$_4$ core-shell upconverting nanoparticles

Once the highly luminescent oleate-capped NaYF$_4$:Yb,Er,Gd@NaYF$_4$ core-shell UCNPs had been synthesised, the next step was their functionalisation with a photosensitiser to yield a platform that could be used for PDT of breast cancer cells. Rose Bengal (RB) was the chosen photosensitiser since its absorption spectrum overlaps the green luminescence emission band of the UCNPs at 541 nm. Thus, it was expected that, following excitation at 980 nm, the Rose Bengal would be activated *via* a FRET process to produce singlet oxygen.

Before incorporation of the RB, the surface of the oleate-capped NaYF$_4$:Yb,Er,Gd@NaYF$_4$ core-shell UCNPs was modified *via* a two-step ligand exchange method as indicated in **Figure 5.7**. In the first step, NOBF$_4$ was inserted in a two-phase system to remove oleate from the surface of the nanoparticles and to stabilise the uncoated particles. This first step resulted in BF$_4^-$-capped NaYF$_4$:Yb,Er,Gd@NaYF$_4$ core-shell UCNPs. In a second step, the ligand l-lysine was bound to the surface of the nanoparticles yielding lysine-capped NaYF$_4$:Yb,Er,Gd@NaYF$_4$ core-shell UCNPs. Water dispersibility of the nanoparticles was achieved following the incorporation of the lysine ligand.
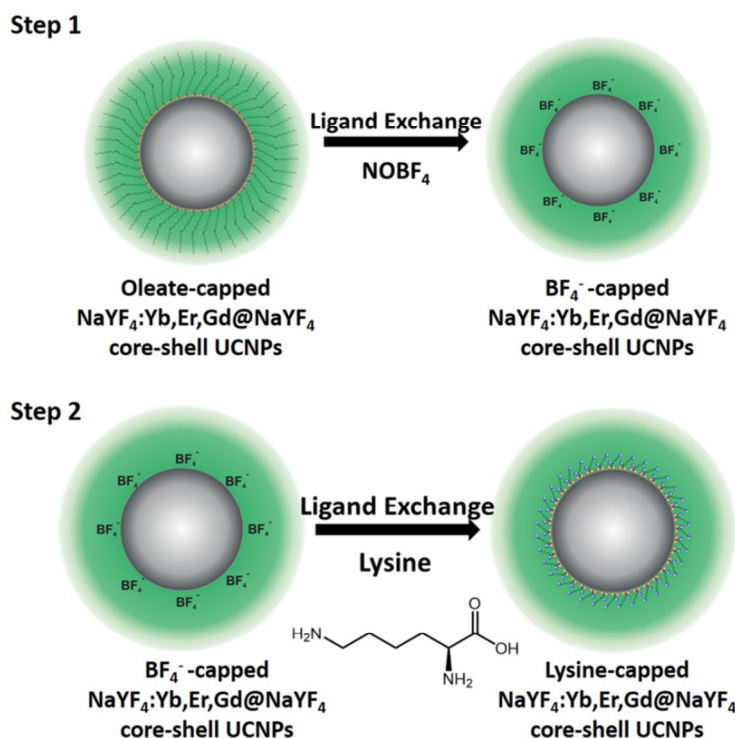
Figure 5.7 ‖ Schematic representation of the two ligand exchange steps followed to obtain lysine-capped NaYF$_4$:Yb,Er,Gd@NaYF$_4$ core-shell UCNPs from the oleate-capped NaYF$_4$:Yb,Er,Gd@NaYF$_4$ core-shell UCNPs.

The photosensitiser RB was bound to the free amine groups of the lysine-capped NaYF$_4$:Yb,Er,Gd@NaYF$_4$ core-shell UCNPs *via* classical EDC/NHS chemistry yielding RB-lysine functionalised NaYF$_4$:Yb,Er,Gd@NaYF$_4$ core-shell UCNPs. During the surface modification, the nanoparticles show no tendency of agglomeration, as confirmed by the DLS measurements (**Figure 5.8**). A decrease in the solvodynamic diameter of the nanoparticles was observed when the oleate ligand was replaced by BF$_4^-$ (from *ca.* 21 to *ca.* 14 nm). As expected, the solvodynamic diameter increased to 23.7 ± 8.4 nm following incorporation of the Rose Bengal to the lysine-capped NaYF$_4$:Yb,Er,Gd@NaYF$_4$ nanoparticles.
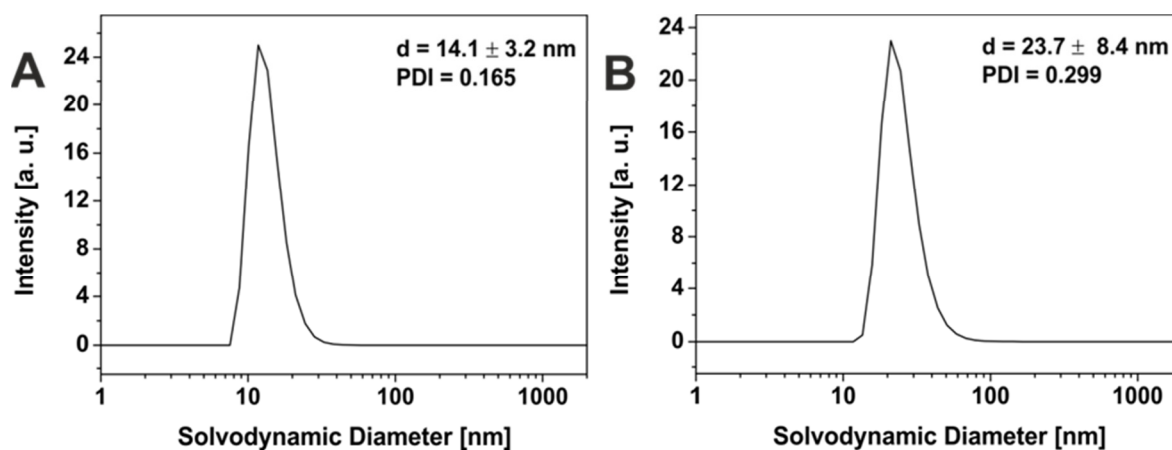
Figure 5.8‖ DLS measurements of the BF_4^- (**A**) and of the lysine@RB coated nanoparticles (**B**) were performed in DMF (**A**) and DMSO (**B**). The curve shows the DLS signal weighted for Number with a solvodynamic diameter of 14.1 ± 3.2 nm (**A**) and 23.7 ± 8.4 nm (**B**).

The Rose Bengal loading was estimated to be 160 RB molecules per nanoparticle, which is quite similar of the numbers of emitters in the nanoparticle. The RB-lysine functionalised $NaYF_4$:Yb,Er,Gd@$NaYF_4$ core-shell UCNPs exhibited colloidal stability in DMSO and water, and were stable in phosphate buffer and cell medium which enabled assessment of the nanoparticle performance for intracellular experiments.

The surface architecture of the different types of functionalised nanoparticles was validated by FTIR measurements (**Figure 5.9**). The FTIR spectrum of the oleate-capped $NaYF_4$:Yb,Er,Gd@$NaYF_4$ core-shell UCNPs exhibited strong C-H stretching at 2,926 and 2,851 cm^{-1} that disappeared, as expected, following ligand exchange with l-lysine. In addition to the C=O stretching (at 1,558 and 1,457 cm^{-1}), a strong absorption band at 1,655 cm^{-1} attributed to the C-N bending was observed in the FTIR spectrum of the lysine-capped UCNPs. Following incorporation of the Rose Bengal, the band due to the amine bending was reduced and new absorption bands occurred at 1,543, 1,457 and 1,342 cm^{-1} that were attributed to the amide stretching and the C=C stretching of the aromatic rings of the photosensitiser. The C-H bending of the aromatic ring and the C-I bending were visible at 954 cm^{-1} and 700 cm^{-1}, respectively.
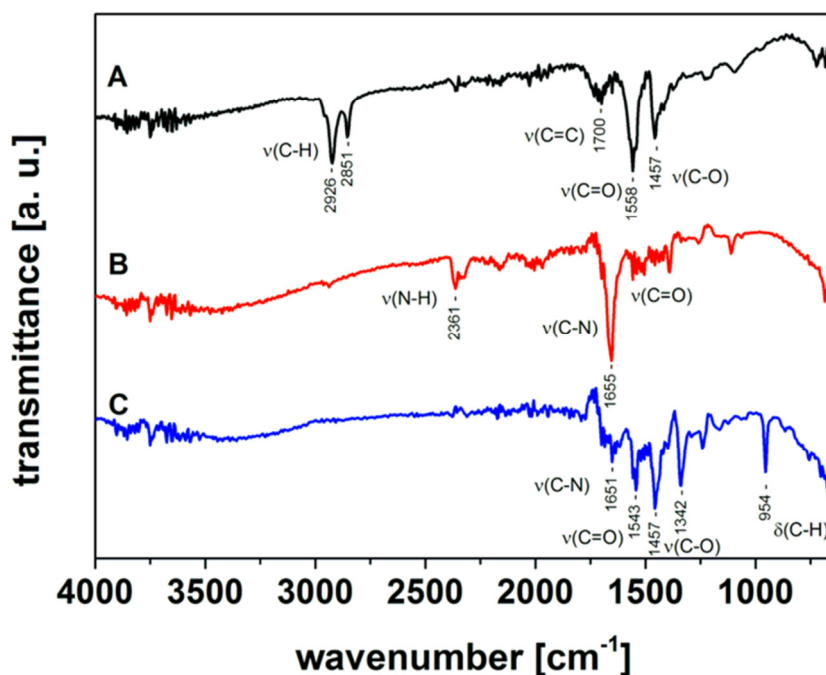
Figure 5.9 ‖ FTIR spectra of UCNPs coated with **A**) oleate, **B**) L-lysine and **C**) L-lysine modified with Rose Bengal (RB).

5.4.3 Optical properties of the RB–lysine functionalised NaYF$_4$:Yb,Er,Gd@NaYF$_4$ core-shell upconverting nanoparticles

Surface modification affects the luminescence characteristics of the UCNPs upon NIR excitation. The spectrum of the RB-lysine functionalised UCNPs shows the emission of the RB overlapping the typical upconversion luminescence (**Figure 5.6**), accompanied by changing the predominately visible colour of the excited particles from green to red. The green (541 nm) to red (652 nm) ratio of the luminescence emission intensities of the oleate-capped core-shell UCNPs was 7.7:1 (**Figure 5.6B – ii**) following 980 nm irradiation. The green to red ratio, under the same irradiation conditions, decreased to 0.6:1 for the RB-lysine functionalised core-shell UCNPs (**Figure 5.6B – i**) due to the presence of the photosensitiser Rose Bengal, which absorbs light in the region of *ca.* 550 nm. The appearance of the emission of RB can be assigned to two effects: a) the so-called inner filter effect and b) Förster resonance energy transfer (FRET). Time-resolved spectroscopy revealed the FRET mechanism by comparing the lifetime of the two main emission peaks of the UCNPs before and after the attachment of the photosensitiser (**Figure 5.10** and **Table 5.2**).

The lifetime of the green donor emission decreased from 216 to 161 µs, yielding in a
FRET efficiency of 25%. The lifetime of the red emission measured at 656 ± 50 nm,
containing the long luminescence lifetime of the UCNPs and the short lifetime of RB,
decreased from 342 to 266 µs. The acceptor luminescent lifetime of the RB is in the same
range compared to the donor lifetime of the green emission. This demonstrates, by
introducing l-lysine as short linker molecule, that the weak binding affinity of RB to the
surface of the UCNPs was overcome and the distance of the acceptor and donor system
was kept as short as possible to enable efficient FRET.
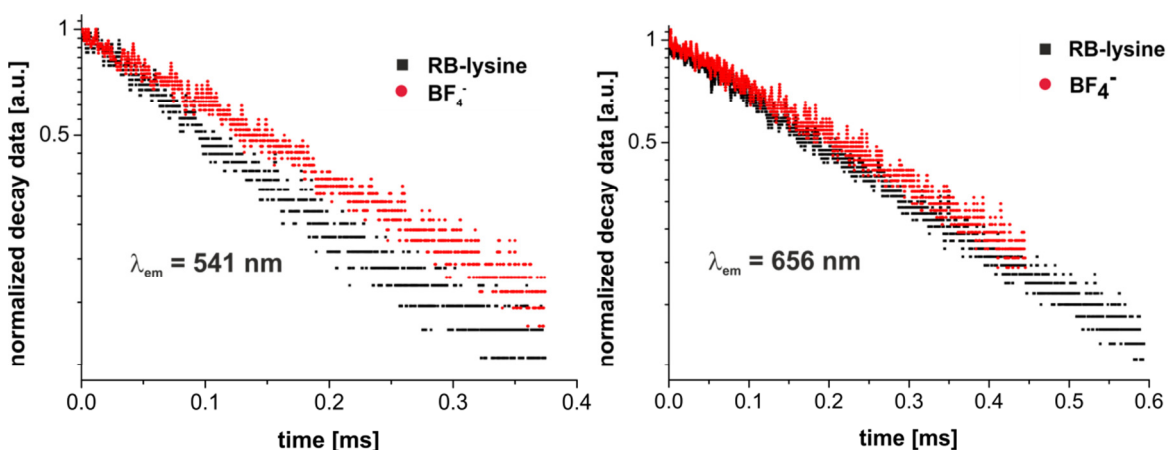
Figure 5.10‖ Cut and normalized decay data of UCNPs before and after attachment of Rose Bengal (RB)
dispersed in DMSO. Particles were excited at 980 nm and the luminescence decay of the green and red
upconversion emission was recorded. A reduction of the green upconversion luminescence lifetime was
observed upon binding the dye RB to the surface of the nanoparticles.

Table 5.2‖ Luminescence lifetimes of the green and red UCNP emission were measured before and after the
attachment of RB. The particles were dispersed in DMSO (N = 3).

	NaYF$_4$@lysine@RB	NaYF$_4$@BF$_4^-$
τ_{Green} [µs]	161 ± 5	215 ± 6
τ_{Red} [µs]	266 ± 3	342 ± 20

5.4.4 Singlet oxygen production by the RB-lysine functionalised NaYF$_4$:Yb,Er,Gd@NaYF$_4$ core-shell UCNPs

The ability of the RB-lysine functionalised UCNPs to produce singlet oxygen ($^1O_2$) following NIR excitation at 980 nm was investigated using the singlet oxygen probe 9,10-anthracenediyl-bis(methylene) dimalonic acid (ABMA). ABMA is photobleached in the presence of $^1O_2$ and thus the fluorescence emission of the probe is quenched upon reaction with $^1O_2$. The production of $^1O_2$ by the RB-lysine functionalised UCNPs was investigated in two different media: DMSO and McCOY's 5A cell culture medium (**Figure 5.11**).

In DMSO, the fluorescence emission intensity of ABMA was readily quenched over time confirming the production of singlet oxygen by the RB photosensitiser on the surface of the UCNPs following NIR excitation at 980 nm. These results confirm the energy transfer between the UCNPs and the photosensitiser and the subsequent production of singlet oxygen. In cell culture medium, the production of singlet oxygen following irradiation of the RB-lysine UCNPs at 980 nm was significantly reduced (**Figure 5.11B – red**) due to the quenching of the $^1O_2$ and the absorption of the 980 nm light in the aqueous based medium.
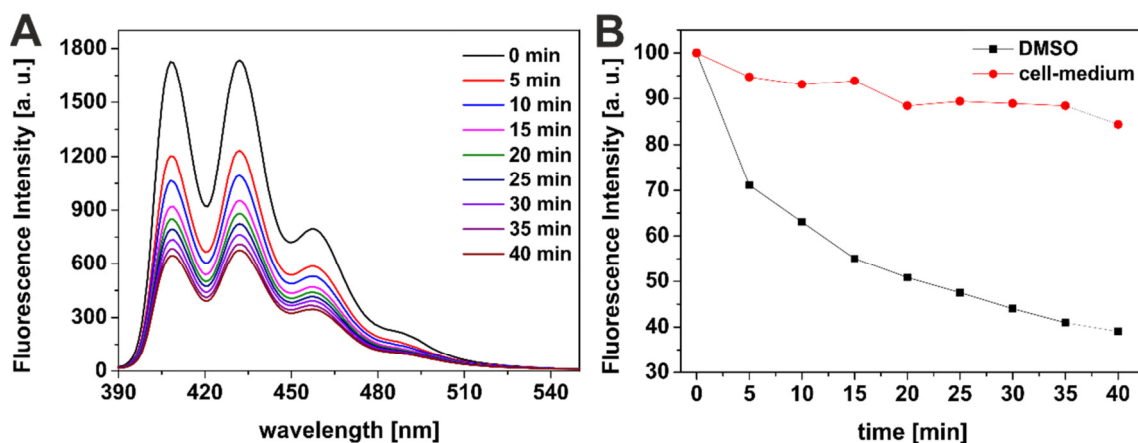
Figure 5.11 ‖ A) Time-dependent decay of the fluorescence emission spectrum of the singlet oxygen probe 9,10-anthracenediyl-bis(methylene)dimalonic acid (ABMA, λ_{exc} = 380 nm) upon irradiation of the RB@lysine functionalised UCNPs with the NIR-laser (980 nm, cw, 200 mW, DMSO). **B)** Normalised decay of the fluorescence emission intensity of ABMA at 410 nm at different laser irradiation time of RB@lysine functionalised UCNPs in DMSO (black) and in McCOY's 5A phenol red free cell culture medium (red).

5.4.5 Cellular uptake of the RB-lysine functionalised NaYF$_4$:Yb,Er,Gd@NaYF$_4$ core-shell UCNPs

The suitability of the RB-lysine functionalised UCNPs to act as PDT agents was studied intracellularly. The first step was to confirm the cellular uptake of the functionalised nanoparticles by SK-BR-3 human breast adenocarcinoma cells. SK-BR-3 cells were incubated with the RB-lysine modified UCNPs for 3 h and the internalisation of the nanoparticles by the cells was investigated using two imaging techniques, *viz*, multi-photon and laser scanning confocal microscopy. To confirm the internalisation of the RB-lysine functionalised UCNPs within the breast cancer SK-BR-3 cells using a multi-photon microscope, the samples were excited using two-photon excitation at two wavelengths: 1) 880 nm to excite the RB on the functionalised UCNPs and to collect the differential interference contrast (DIC) images (**Figure 5.12a – c** and **g – i**); and 2) 980 nm to excite the UCNPs directly (**Figure 5.12d – f** and **j – l**). Following two-photon excitation at 880 nm, the fluorescence emission due to the RB on the UCNPs was observed in the green channel (550 ± 42.5 nm; **Figure 5.12b**). This emission was not observed in control cells without the RB-lysine functionalised UCNPs loaded (**Figure 5.12h**), confirming the presence of the photosensitiser within the SK-BR-3 cells treated with the RB-lysine functionalised UCNPs. No fluorescence emission was observed in the red channel (655 ± 20 nm) following 880 nm irradiation for the cells treated with the functionalised UCNPs (**Figure 5.12c**) or for the control cells without UCNPs (**Figure 5.12i**). This indicates that the fluorescence observed in the green channel for cells treated with the RB-lysine functionalised UCNPs was due to the RB on the particles. Following 980 nm irradiation, the direct luminescence from the functionalised UCNPs was observed in both the green and in the red channels **(Figure 5.12e** and **f**, respectively) as expected from the luminescence spectrum of the UCNPs. This result confirms the uptake of the RB functionalised UCNPs by the SK-BR-3 cells. The upconversion luminescence images of the RB-lysine functionalised UCNPs within the SK-BR-3 cells (**Figure 5.12e** and **f**) appeared to be 'blurred' and of poor resolution. Low resolution images of UCNPs obtained using two-photon laser scanning microscopy have been previously reported and are associated with the presence of axial interferences from out-of-focus light together with lateral interferences from scattering within the focal plane. The quality of the upconversion luminescence images could be improved using a microscope equipped with a confocal pinhole, which would eliminate both the axial and lateral interferences.[39] Despite the blurred images (**Figure 5.12e** and **f**), it is clear that the RB-lysine functionalised UCNPs are successfully emitting upconversion luminescence from within the cancer cells. No upconversion luminescence was observed when control cells with no RB-lysine

functionalised UCNPs were imaged following irradiation using the 980 nm NIR laser under
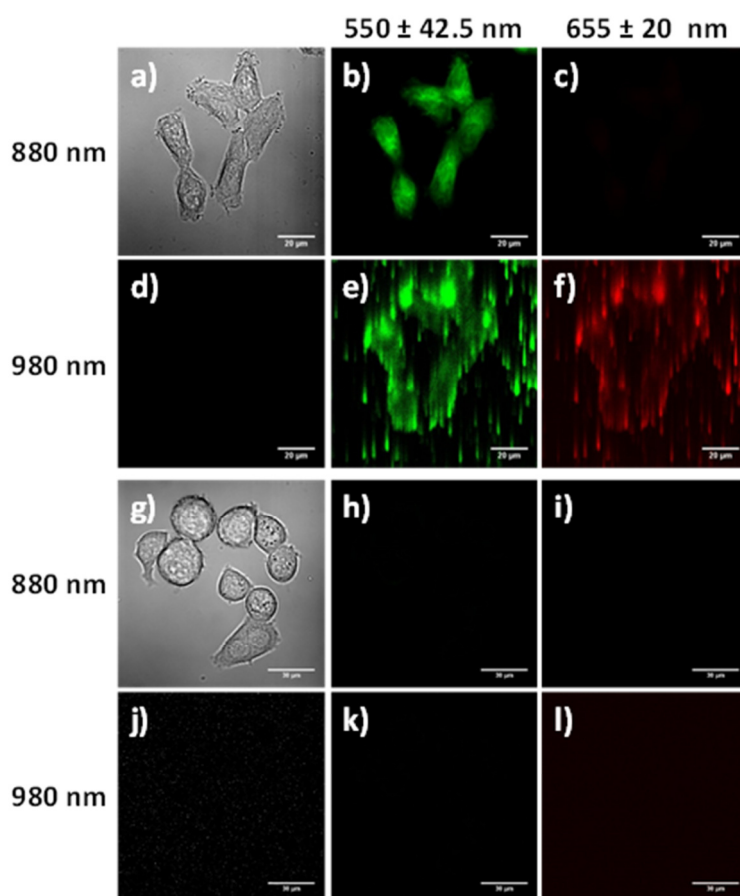the same conditions (**Figure 5.12k** and **l**).

Figure 5.12‖ Multi-photon microscopy images of SK-BR-3 cells: **a** – **f**) incubated with RB functionalised
UCNPs (25 μg·mL^{-1}) and **g** – **l**) control cells without functionalised UCNPs. DIC images were obtained using a
880 nm laser (**a** and **g**). The emission was collected in the green (550 ± 42.5 nm; **b**, **e**, **h** and **k**) and red
(655 ± 20 nm; **c**, **f**, i and **l**) channels following excitation at 880 and 980 nm. Scale bars: **a** – **f**) 20 μm and **g** - **l**)
30 μm.

The experiments performed using the confocal microscope also confirmed the
internalisation of the RB functionalised UCNPs within the SK-BR-3 cells. The cells were
incubated with the RB-lysine functionalised UCNPs for 3 h and the emission due to the
RB on the nanoparticles was collected in the red channel (560 – 615 nm) following
excitation with a 543 nm HeNe laser (**Figure 5.13a - c**). The morphology of the treated
cells was observed in the DIC images obtained with transmitted light at 488 nm. Laser
scanning confocal microscopy images of the treated cells (**Figure 5.13a – c**) show an
intense red emission due to the RB of the functionalised UCNPs within the cells that was
not observed in control cells (**Figure 5.13d – f**). Morphological changes were not
observed for either of the cell samples suggesting that the RB-lysine UCNPs were not
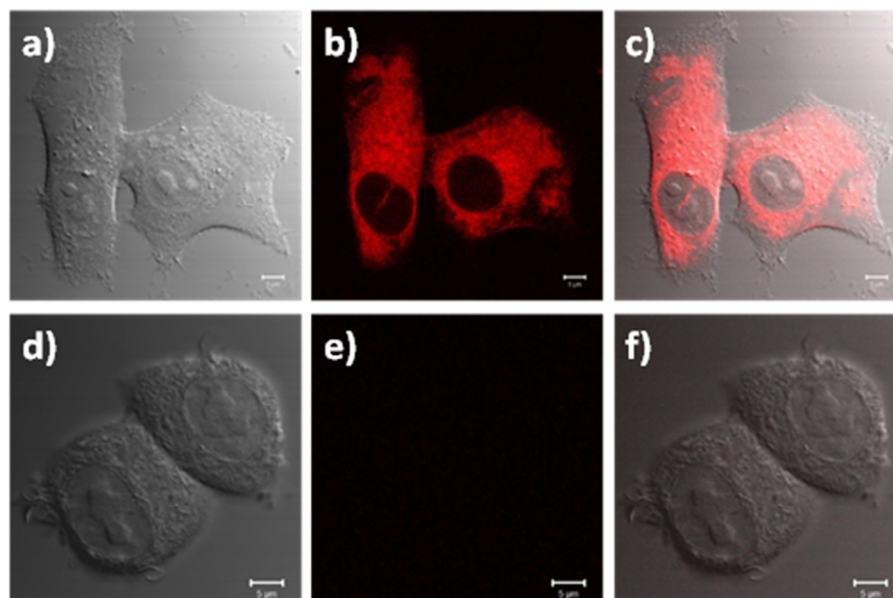toxic to the cells.

Figure 5.13‖ Laser scanning confocal microscopy images of SK-BR-3 cells: **a** – **c**) incubated with functionalised UCNPs (25 µg·mL^{-1}) and **d** – **f**) control cells without functionalised UCNPs. DIC images were obtained using a 488 nm laser (**a** and **d**). The emission due to the RB on the UCNPs was collected in the red channel (560 – 615 nm; **b** and **e**) following excitation at 543 nm. Images **c** and **f** are composite images of the DIC and red channels. Scale bars are 5 µm.

5.4.6 Suitability of the RB-lysine functionalised NaYF$_4$:Yb,Er,Gd@NaYF$_4$ UCNPs for photodynamic therapy of breast cancer cells

To establish the efficacy of the functionalised UCNPs as PDT agents, a CellTiter-Blue® cell viability assay[40] was performed *in vitro*. This assay provides information regarding the number of viable cells present in the wells of a 96-well plate by measuring the metabolic capacity of the studied cells. Viable cells are able to reduce the indicator dye resazurin into a fluorescent product, resorufin, the fluorescence emission intensity of which can be measured at 594 nm using a microplate reader upon excitation at 561 nm. Conversely, non-viable cells lose their metabolic capacity and are not able to reduce resazurin thus are unable to generate a measurable fluorescent signal. SK-BR-3 cells were seeded on 96-well microplates and incubated with varying concentrations of RB-lysine functionalised UCNPs for 3 h. A positive control for cytotoxicity, consisting of cells treated with staurosporine, was also included in the assay. Following incubation with the RB-lysine functionalised UCNPs, the cells were thoroughly washed with PBS to remove the nanoparticles that had not been internalised by the SK-BR-3 cells. The cells were subjected to PDT by irradiation with a NIR 980 nm laser for 6 min per well. Control experiments where cells incubated with the varying concentrations of RB-lysine functionalised UCNPs and with staurosporine were kept in the dark and not irradiated were also performed. Cell viability of the SK-BR-3 cells was assessed 48 h following PDT

treatment (**Figure 5.14**). A decrease in cell viability concomitant with an increase in the concentration of RB-lysine functionalised UCNPs (from 0 to 20 $\mu g \cdot mL^{-1}$) can be observed following PDT treatment of the SK-BR-3 cells. However, at high concentrations (*i.e.* ≥ 20 $\mu g \cdot mL^{-1}$) the nanoparticles exhibited some dark toxicity as indicated by the decrease in viability of cells that had been incubated with the functionalised UCNPs but had not been irradiated.
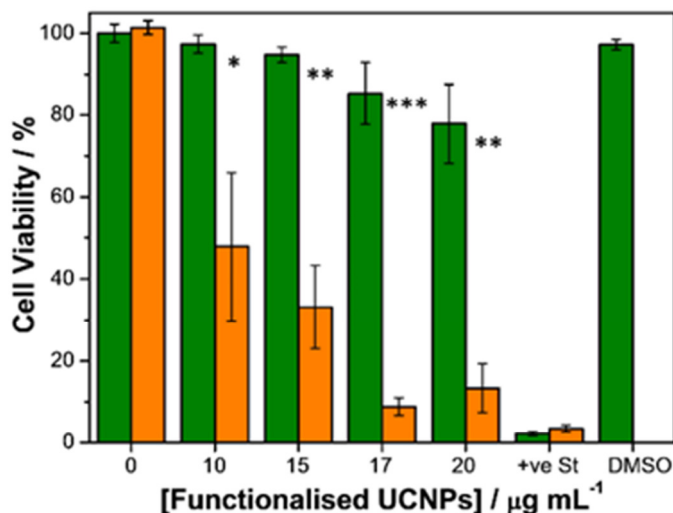

Figure 5.14‖ CellTiter-Blue® cell viability assay of SK-BR-3 cells that were incubated with varying concentrations (from 0 to 20 $\mu g \cdot mL^{-1}$) of RB functionalised UCNPs for 3 h and irradiated (orange) or non-irradiated (green) with the 980 nm NIR laser for 6 min. +ve St indicates SK-BR-3 cells that had been treated with staurosporine – a positive control for cytotoxicity. DMSO indicates SK-BR-3 cells that had been treated with McCOY's 5A phenol red free medium containing 0.25% DMSO for 3 h. Each experiment was repeated in triplicate and the relative standard error is indicated by the error bars. Statistically significant difference between non-irradiated and irradiated samples is indicated by * at $P < 0.04$; ** at $P < 0.0006$ and *** at $P < 0.00007$, obtained using a two-tailed Student's t-test, where $P < 0.05$ is considered statistically significant.

At a concentration of functionalised UCNPs of 15 $\mu g \cdot mL^{-1}$, 67% of the cells were killed following PDT while the dark toxicity of the nanoparticles was minimal (5%). The effect that the DMSO used to solubilise the functionalised UCNPs had on the viability of the cells was also investigated. No cell-death was observed when the SK-BR-3 cells were treated with McCOY's 5A phenol red free medium containing 0.25% DMSO for 3 h confirming that, under the conditions used to perform the cell viability assay, DMSO was not toxic for the cells. The results from the CellTiter-Blue® cell viability assay suggested that a concentration of 15 $\mu g \cdot mL^{-1}$ of the RB-lysine functionalised UCNPs was ideal for PDT. Laser scanning confocal fluorescence microscopy was used to further determine the suitability of the functionalised UCNPs for PDT. SK-BR-3 cells seeded on coverslips were treated with the RB-lysine functionalised UCNPs (15 $\mu g \cdot mL^{-1}$) for 3 h. Following removal of

non-uptaken nanoparticles by washing, singlet oxygen was activated by irradiating the UCNPs within the cells with the 980 nm NIR laser for 6 min. The treated cells were imaged using confocal laser scanning microscopy *ca.* 24 h following PDT treatment (**Figure 5.15a – c**). DIC images of the SK-BR-3 cells clearly show degradation of the cell membrane, which was indicative of cell death (**Figure 5.15a** and **d**). The RB-lysine functionalised UCNPs accumulated in the nucleus of the SK-BR-3 cells that had been irradiated with the 980 nm NIR laser (**Figure 5.15b** and **c**).
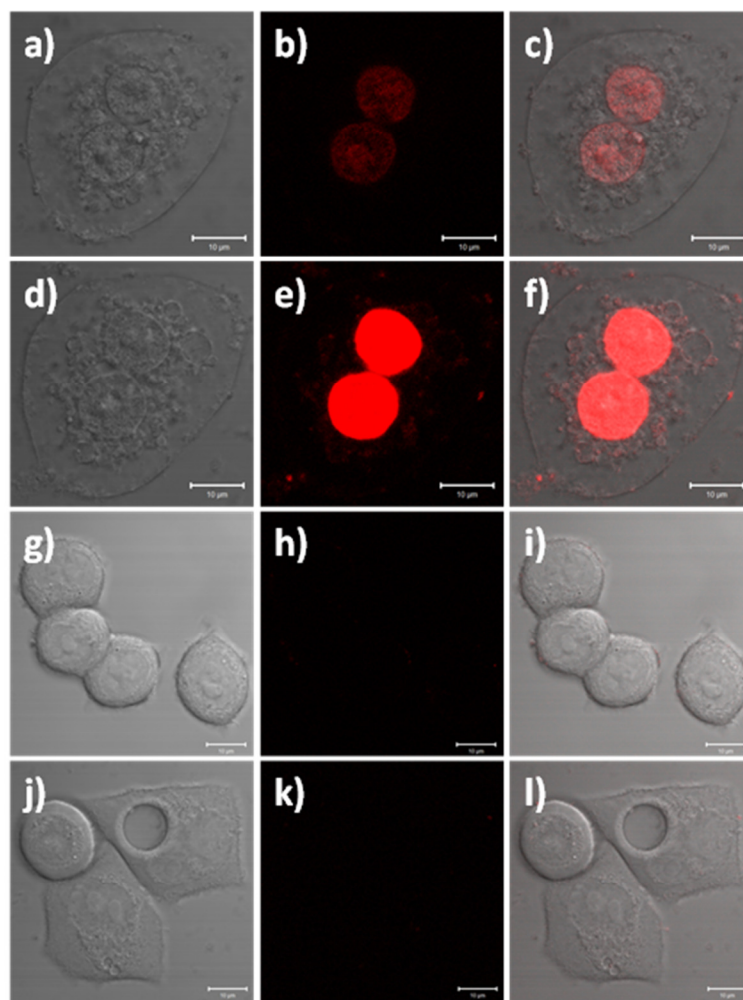
Figure 5.15‖ Laser scanning confocal microscopy images of SK-BR-3 cells: **a – f)** incubated with the functionalised UCNPs (15 µg·mL^{-1}) and irradiated with the 980 nm laser before (**a – c**) and following (**d – f**) addition of propidium iodide; **g – i)** without functionalised UCNPs, irradiated with the 980 nm laser and treated with propidium iodide; and **j – l)** incubated with the functionalised UCNPs (15 µg·mL^{-1}), non-irradiated with the 980 nm laser and treated with propidium iodide. DIC images were obtained using a 488 nm laser (**a**, **d**, **g** and **j**). The fluorescence emission due to the RB on the UCNPs and the propidium iodide was collected in the red channel (560 – 615 nm; **b**, **e**, **h** and **k**) following excitation at 543 nm (laser power 4%). Images **c**, **f**, **i** and **l** are composite images of the red and DIC channels. Scale bars are 10 µm.

The accumulation of the particles in the nucleus of the cells was not observed for non-irradiated SK-BR-3 cells that had been incubated with the RB-lysine functionalised UCNPs (**Figure 5.15j – l** and **Figure 5.16**). This result suggests that the location of the UCNPs in the nucleus, seen in **Figure 5.15b** and **c**, following NIR PDT could be indicative of cell death.

Figure 5.16‖ Laser scanning confocal microscopy images of non-irradiated SK-BR-3 cells: **a – c**) incubated with the functionalised UCNPs (15 µg·mL^{-1}); and **d – f**) without functionalised UCNPs. The images were taken before treatment with propidium iodide and the fluorescence emission due to the RB on the UCNPs was collected in the red channel (560 – 615 nm; b and e) following excitation at 543 nm using a 100% laser power. DIC images were obtained using a 488 nm laser (**a** and **d**). Images **c** and **f** are composite images of the red and DIC channels. Scale bars are 10 µm.

Furthermore, the cells that had been treated with the RB-lysine functionalised UCNPs and irradiated with the 980 nm NIR laser subsequently stained positive when incubated with propidium iodide (**Figure 5.15d – f** and **Figure 5.17**) confirming the cell death following PDT treatment.[41] The changes of cellular membrane integrity or the positive stain for propidium iodide were not observed for the control experiments.
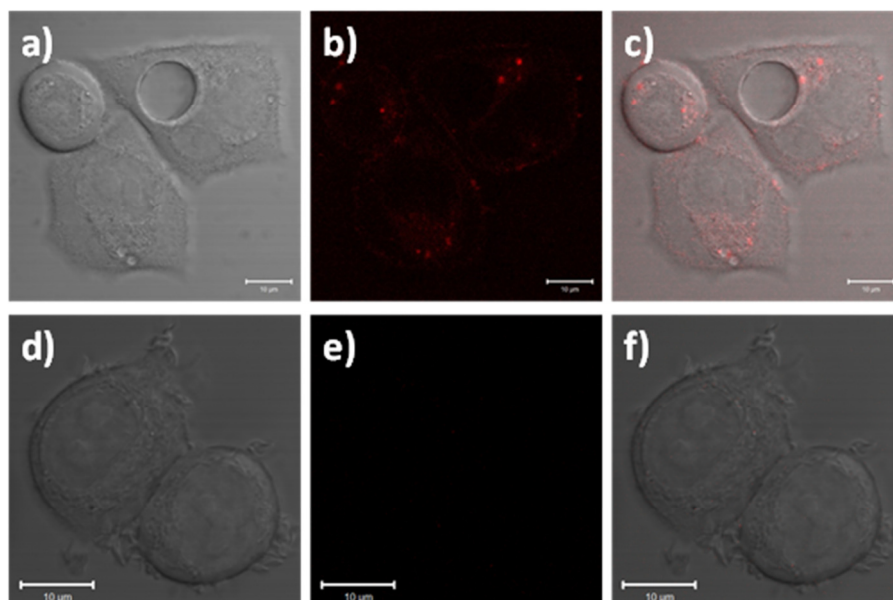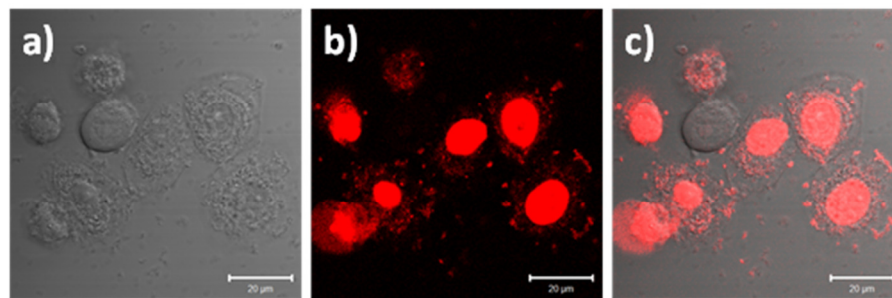
Figure 5.17‖ Laser scanning confocal microscopy images of irradiated SK-BR-3 cells incubated with the functionalised UCNPs (15 µg·mL^{-1}) and treated with propidium iodide. **a)** DIC image obtained using a 488 nm laser; **b)** fluorescence emission due to the RB on the UCNPs and the propidium iodide (red channel, 560 – 615 nm) following excitation at 543 nm (laser power 4%); and **c)** composite image of the red and DIC channels. Scale bars are 20 µm.

These included: the SK-BR-3 cells without functionalised UCNPs that had been irradiated with the 980 nm NIR laser for 6 min (**Figure 5.15g – i**); the non-irradiated SK-BR-3 cells incubated with the functionalised UCNPs (**Figure 5.15j – l**); and the non-irradiated SK-BR-3 cells without functionalised UCNPs (**Figure 5.18**). The laser power used to image the SK-BR-3 cells treated with propidium iodide was too low (4%) to be able to observe the fluorescence emission due to the internalised RB-lysine functionalised UCNPs in the non-irradiated SK-BR-3 cells shown in **Figure 5.15j – l**. To confirm the presence of the RB-lysine functionalised UCNPs in the non-irradiated SK-BR-3 cells, images using a higher laser power (100%) were obtained prior to the addition of the propidium iodide and compared with the control non-irradiated SK-BR-3 cells without RB-lysine functionalised UCNPs imaged under the same conditions (**Figure 5.15**). The fluorescence emission due to the RB from the SK-BR-3 cells that had been treated with the RB-lysine functionalised UCNPs was not observed for the control cells, thus confirming the internalisation of the RB-lysine functionalised UCNPs by the SK-BR-3 cells and the importance of NIR 980 nm irradiation to induce cell death *via* PDT. The results shown in **Figure 5.15** and **Figure 5.16 – 18** highlight that the RB-lysine functionalised UCNPs are ideal photosensitiser vehicles for PDT of breast cancer cells.
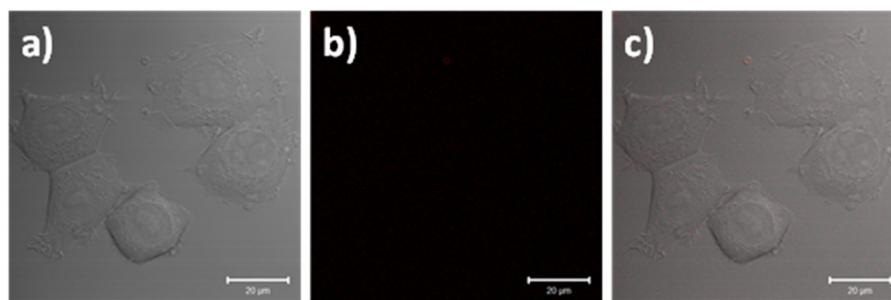
Figure 5.18‖ Laser scanning confocal microscopy images of non-irradiated SK-BR-3 cells without functionalised UCNPs that had been treated with propidium iodide. **a)** DIC image obtained using a 488 nm laser; **b)** fluorescence emission (red channel, 560 – 615 nm) following excitation at 543 nm (laser power 4%) showing no fluorescence from neither the RB on the UCNPs nor the propidium iodide; and **c)** composite image of the red and DIC channels. Scale bars are 20 µm.

5.5 Conclusions

Highly luminescent lanthanide doped core-shell upconverting nanoparticles have been synthesised and functionalised with the photosensitiser Rose Bengal *via* an amino acid (l-lysine) linker. The short distance between the photosensitiser and the light emitting core has proven efficient for a high energy transfer from the UCNPs core to the RB *via* a FRET process. The FRET process, confirmed from luminescence lifetime measurements, allowed for the excitation of the photosensitiser and thus the production of singlet oxygen using NIR light at 980 nm. The water dispersible RB-lysine functionalised UCNPs were successfully used for PDT of SK-BR-3 breast cancer cells. The efficient internalisation of the RB-lysine functionalised UCNPs by the cells was confirmed using confocal laser scanning microscopy and multi-photon microscopy, which clearly showed the emission from both the RB and the UCNPs only inside the treated cells. Following internalisation of the functionalised UCNPs, the SK-BR-3 cells were irradiated with a 980 nm laser to induce the production of singlet oxygen by RB. Cell viability assays showed high levels of cell death following irradiation, reaching *ca.* 67% of cell death at a RB-lysine functionalised UCNP concentration of only 15 µg·mL^{-1}. Additionally, at this concentration, the RB-lysine functionalised UCNPs were shown to induce negligible dark toxicity of the SK-BR-3 cells that had not been irradiated. The efficient cell death post-PDT was also confirmed using confocal microscopy and the dead cell marker propidium iodide. Only those cells that had been incubated with the RB-lysine functionalised UCNPs and irradiated with NIR light at 980 nm stained positive with propidium iodide, thus confirming the cell death following PDT treatment. The confocal microscopy experiments also showed accumulation of the UCNPs in the nucleus of the SK-BR-3 cells, only in samples that had been irradiated with NIR light to induce production of singlet oxygen. Control

100

cells, treated with the functionalised nanoparticles but not irradiated, did not show accumulation of the UCNPs within the nucleus. For future applications, targeting agents could be incorporated onto the surface of the nanoparticles yielding a vehicle for targeted photodynamic therapy to further improve the efficiency of the treatment and reduce the damage of healthy cells. Furthermore, to complement the treatment potential of the nanoplatform, the nanocrystals doped with Gd^{3+} can also be used as a multimodal diagnostic tool for magnetic resonance imaging (MRI).

The synthesised efficient RB-lysine functionalised UCNPs are shown to be successful candidates for PDT of breast cancer cells using NIR light. The NIR irradiation opens the possibility to use the reported nanoplatform to treat other deep lying tumours.

Acknowledgements

References

1   J. P. Celli, B. Q. Spring, I. Rizvi, C. L. Evans, K. S. Samkoe, S. Verma, B. W. Pogue and T. Hasan, Imaging and photodynamic therapy: mechanisms, monitoring, and optimization, *Chem. Rev.*, **2010**, 110, 2795-2838.

2   K. Plaetzer, B. Krammer, J. Berlanda, F. Berr and T. Kiesslich, Photophysics and photochemistry of photodynamic therapy: fundamental aspects, *Lasers Med. Sci.*, **2009**, 24, 259-268.

3   P. García Calavia, M. J. Marín, I. Chambrier, M. J. Cook and D. A. Russell, Towards optimisation of surface enhanced photodynamic therapy of breast cancer cells using gold nanoparticle–photosensitiser conjugates, *Photochem. Photobiol. Sci.*, **2018**, DOI: 10.1039/C7PP00225D.

4   G. Obaid, I. Chambrier, M. J. Cook and D. A. Russell, Targeting the oncofetal Thomsen–Friedenreich disaccharide using Jacalin-PEG phthalocyanine gold

nanoparticles for photodynamic cancer therapy, *Angew. Chem. Int. Ed.*, **2012**, 51, 6158-6162.

5   M. J. Marín and D. A. Russell, in Near-Infrared Nanomaterials: Preparation, Bioimaging and Therapy Applications, ed. F. Zhang, *RCS*, Cambridge, **2016**, pp. 192-231.

6   G. Chen, H. Qiu, P. N. Prasad and X., Chen, upconversion nanoparticles: design, nanochemistry, and applications in theranostics, *Chem. Rev.*, **2014**, 114, 5161-5214.

7   M. Wang, G. Abbineni, A. Clevenger, C. Mao and S. Xu, Upconversion nanoparticles: synthesis, surface modification and biological applications, *Nanomedicine*, **2011**, 7, 710-729.

8   S. Jiang, M. K. Gnanasammandhan and Y. Zhang, Optical imaging-guided cancer therapy with fluorescent nanoparticles, *J. Royal Soc. Interface*, **2010**, 7, 3-18.

9   M. Haase and H. Schäfer, Upconverting nanoparticles, *Angew. Chem. Int. Ed.*, **2011**, 50, 5808-5829.

10   J. F. Suyver, J. Grimm, M. K. van Veen, D. Biner, K. W. Krämer and H. U. Güdel, Upconversion spectroscopy and properties of $NaYF_4$ doped with Er^{3+}, Tm^{3+} and/or Yb^{3+}, *J. Lumin.*, **2006**, 117, 1-12.

11   A. G. Arguinzoniz, E. Ruggiero, A. Habtemariam, J. Hernández-Gil, L. Salassa and J. C. Mareque-Rivas, Photodynamic therapy: light harvesting and photoemission by nanoparticles for photodynamic therapy, *Part. Part. Syst. Char.*, **2014**, 31, 46-75.

12   S. Wilhelm, T. Hirsch, W. M. Patterson, E. Scheucher, T. Mayr and O. S. Wolfbeis, Multicolor upconversion nanoparticles for protein conjugation, *Theranostics*, **2013**, 3, 239-248.

13   V. Muhr, S. Wilhelm, T. Hirsch and O. S. Wolfbeis, Upconversion nanoparticles: from hydrophobic to hydrophilic surfaces, *Acc. Chem. Res.*, **2014**, 47, 3481-3493.

14   C. Wang, L. Cheng and Z. Liu, Upconversion nanoparticles for photodynamic therapy and other cancer therapeutics, *Theranostics*, **2013**, 3, 317-330.

15   P. Zhang, W. Steelant, M. Kumar and M. Scholfield, Versatile photosensitizers for photodynamic therapy at infrared excitation, *J. Am. Chem. Soc.*, **2007**, 129, 4526-4527.

16   Y. Guo, M. Kumar and P. Zhang, Nanoparticle-based photosensitizers under CW infrared excitation, *Chem. Mater.*, **2007**, 19, 6071-6072.

17   X. Yang, Q. Xiao, C. Niu, N. Jin, J. Ouyang, X. Xiao and D. He, Multifunctional core–shell upconversion nanoparticles for targeted tumor cells induced by near-infrared light, *J. Mater. Chem. B*, **2013**, 1, 2757-2763.

18   H. Guo, H. Qian, N. M. Idris and Y. Zhang, Singlet oxygen-induced apoptosis of cancer cells using upconversion fluorescent nanoparticles as a carrier of photosensitizer, *Nanomed. Nanotechnol. Biol. Med.*, **2010**, 6, 486-495.

19   H. S. Qian, H. C. Guo, P. C.-L. Ho, R. Mahendran and Y. Zhang, Mesoporous-silica-coated up-conversion fluorescent nanoparticles for photodynamic therapy, *Small*, **2009**, 5, 2285-2290.

20   B. Hou, B. Zheng, X. Gong, H. Wang, S. Wang, Z. Liao, X. Li, X. Zhang and J. Chang, A UCN@mSiO$_2$@cross-linked lipid with high steric stability as a NIR remote controlled-release nanocarrier for photodynamic therapy, *J. Mater. Chem. B*, **2015**, 3, 3531-3540.

21   M. Gonzalez-Bejar, M. Liras, L. Frances-Soriano, V. Voliani, V. Herranz-Perez, M. Duran-Moreno, J. M. Garcia-Verdugo, E. I. Alarcon, J. C. Scaiano and J. Perez-Prieto, NIR excitation of upconversion nanohybrids containing a surface grafted Bodipy induces oxygen-mediated cancer cell death, *J. Mater. Chem. B*, **2014**, 2, 4554-4563.

22   J. Shan, S. J. Budijono, G. Hu, N. Yao, Y. Kang, Y. Ju and R. K. Prud'homme, Pegylated composite nanoparticles containing upconverting phosphors and meso-tetraphenyl porphine TPP for photodynamic therapy, *Adv. Funct. Mater.*, **2011**, 21, 2488-2495.

23   C. Wang, H. Tao, L. Cheng and Z. Liu, Near-infrared light induced in vivo photodynamic therapy of cancer based on upconversion nanoparticles, *Biomaterials*, **2011**, 32, 6145-6154.

24   X. Wang, K. Liu, G. Yang, L. Cheng, L. He, Y. Liu, Y. Li, L. Guo and Z. Liu, Near-infrared light triggered photodynamic therapy in combination with gene therapy using upconversion nanoparticles for effective cancer cell killing, *Nanoscale*, **2014**, 6, 9198-9205.

25   S. S. Lucky, N. Muhammad Idris, Z. Li, K. Huang, K. C. Soo and Y. Zhang, Titania coated upconversion nanoparticles for near-infrared light triggered photodynamic therapy, *ACS Nano*, **2015**, 9, 191-205.

26   K. Liu, X. Liu, Q. Zeng, Y. Zhang, L. Tu, T. Liu, X. Kong, Y. Wang, F. Cao, S. A. G. Lambrechts, M. C. G. Aalders and H. Zhang, Covalently assembled NIR nanoplatform for simultaneous fluorescence imaging and photodynamic therapy of cancer cells, *ACS Nano*, **2012**, 6, 4054-4062.

27   D. K. Chatterjee and Y. Zhang, Upconverting nanoparticles as nanotransducers for photodynamic therapy in cancer cells, *Nanomedicine*, **2008**, 3, 73-82.

28   A. Zhou, Y. Wei, B. Wu, Q. Chen and D. Xing, Pyropheophorbide A and c(RGDyK) comodified chitosan-wrapped upconversion nanoparticle for targeted near-infrared photodynamic therapy, *Mol. Pharm.*, **2012**, 9, 1580-1589.

29   S. Cui, H. Chen, H. Zhu, J. Tian, X. Chi, Z. Qian, S. Achilefu and Y. Gu, Amphiphilic
      chitosan modified upconversion nanoparticles for in vivo photodynamic therapy
      induced by near-infrared light, *J. Mater. Chem.*, **2012**, 22, 4861-4873.

30   H. Wang, Z. Liu, S. Wang, C. Dong, X. Gong, P. Zhao and J. Chang, MC540 and
      Upconverting nanocrystal coloaded polymeric liposome for near-infrared light-
      triggered photodynamic therapy and cell fluorescent imaging, *ACS Appl. Mater.
      Interfaces*, **2014**, 6, 3219-3225.

31   G. Tian, W. Ren, L. Yan, S. Jian, Z. Gu, L. Zhou, S. Jin, W. Yin, S. Li and Y. Zhao,
      Red-emitting upconverting nanoparticles for photodynamic therapy in cancer cells
      under near-infrared excitation, *Small*, **2013**, 9, 1929-1938.

32   L. Zhou, Z. Li, Z. Liu, M. Yin, J. Ren and X. Qu, One-step nucleotide-programmed
      growth of porous upconversion nanoparticles: application to cell labeling and drug
      delivery, *Nanoscale*, **2014**, 6, 1445-1452.

33   M. Wang, Z. Chen, W. Zheng, H. Zhu, S. Lu, E. Ma, D. Tu, S. Zhou, M. Huang and
      X. Chen, Lanthanide-doped upconversion nanoparticles electrostatically coupled
      with photosensitizers for near-infrared-triggered photodynamic therapy, *Nanoscale*,
      2014, 6, 8274-8282.

34   V. Muhr, C. Wurth, M. Kraft, M. Buchner, A. J. Baeumner, U. Resch-Genger and T.
      Hirsch, Particle-size-dependent Förster resonance energy transfer from
      upconversion nanoparticles to organic dyes, *Anal. Chem.*, **2017**, 89, 4868-4874.

35   S. Wilhelm, M. Kaiser, C. Wurth, J. Heiland, C. Carrillo-Carrion, V. Muhr, O. S.
      Wolfbeis, W. J. Parak, U. Resch-Genger and T. Hirsch, Water dispersible
      upconverting nanoparticles: effects of surface modification on their luminescence
      and colloidal stability, *Nanoscale*, **2015**, 7, 1403-1410.

36   F. Hund, Das ternäre fluorid $NaYF_4$, *Zeitschrift für anorganische Chemie*, **1950**, 261,
      106-115.

37   N. J. J. Johnson, A. Korinek, C. H. Dong and F. C. J. M. van Veggel, Self-focusing
      by ostwald ripening: a strategy for layer-by-layer epitaxial growth on upconverting
      nanocrystals, *J. Am. Chem. Soc.*, 2012, 134, 11068-11071.

38   C. Würth, M. Kaiser, S. Wilhelm, B. Grauel, T. Hirsch and U. Resch-Genger,
      Excitation power dependent population pathways and absolute quantum yields of
      upconversion nanoparticles in different solvents, *Nanoscale*, **2017**, 9, 4283–4294.

39   M. Yu, F. Li, Z. Chen, H. Hu, C. Zhan, H. Yang and C. Huang, Laser scanning up-
      conversion luminescence microscopy for imaging cells labeled with rare-earth
      nanophosphors, *Anal. Chem.*, **2009**, 81, 930-935.

40   N. P. Gabrielson and D. W. Pack, Acetylation of polyethylenimine enhances gene
      delivery via weakened polymer/DNA interactions, *Biomacromolecules*, **2006**, 7,
      2427-2435.

41   C. Riccardi and I. Nicoletti, Analysis of apoptosis by propidium iodide staining and
      flow cytometry, *Nat. Protocols*, **2006**, 1, 1458-1461.

6 EMBEDDED NANOLAMPS IN ELECTROSPUN NANOFIBERS ENABLING ONLINE MONITORING AND RATIOMETRIC MEASUREMENTS

6.1 Abstract

A multifunctional composite nanomaterial based on nanofiber embedding upconversion nanoparticles (UCNPs) is designed to address the common limitations of bioanalysis including the colloidal stability of nanoparticles, high background signals and small sample volumes. We fabricate thin and uniform electrospun polyvinylpyrrolidone (PVP) nanofibers with a diameter of 170 ± 80 nm, containing up to 254 ± 9 mg mL^{-1} of non-agglomerated UCNPs. On distributing these nanofibers in a microfluidic channel a 50-fold increase in luminescence over dispersed particles can be obtained. A versatile miniaturized platform is created to work with small sample volumes by transferring the upconversion nanofibers into microfluidic channels. Fast and reproducible analytical signal response to their environment is demonstrated by taking advantage of the isotope effect between H_2O and D_2O upon 980 nm excitation. Furthermore, relevance to analytical applications employing energy transfer was confirmed using the spectral overlap of the green UCNP emission with the absorption spectra of a dye. At minute optical path lengths (e.g. 50 mm) the luminescence properties of the UCNPs help in avoiding the most disturbing light scattering effects of the excitation source and channel geometries. This new nanomaterial platform enables rapid, simple and reliable online monitoring in microfluidic systems, medical applications (e.g. in-tissue, in *vivo*) and anti-counterfeiting in contrast to solution-based UCNP applications.
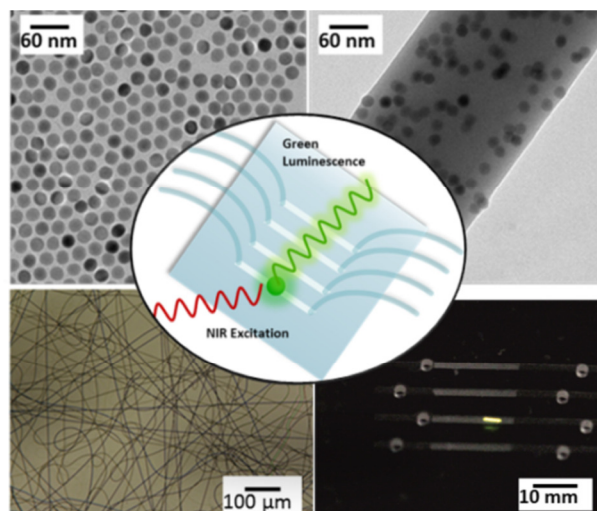
Figure 6.1‖ Upconverting nanoparticles were embedded in electrospun PVP nanofibers as light emitting material for online monitoring in microfluidic systems.

This chapter has been published.

Author contributions

MB synthesized the nanoparticles, performed the surface modification, characterized the composite material, made the optical measurements, designed the figures and wrote the manuscript. LM-C, UN and MS optimized the spinning process, the transfer of the nanofibermat and the bonding in the microfluidic channel. CF performed the TEM measurements. The work was designed and supervised by NW, LMC, TH, AD and AB. The paper was revised by TH, AD, NW and AB (corresponding author).

6.2 Introduction

Nanofibers consist of a one-dimensional nanostructure with a diameter typically in the range of 10–100 nm.[1] With their high surface-to-volume ratio nanofibers have the potential to provide an immense sensing surface when loaded with biorecognition molecules without excluding much volume within a sample.[2] Various methods have been developed for the fabrication of nanofibers, including interfacial polymerization, catalytic synthesis, self-assembly and electrospinning. Of these, electrospinning is the most versatile and cost-effective method with a simple set-up, high-throughput and the possibility of fabricating uniform nanofibers with a long length.[3,4] The different morphology, diameter, composition and spatial alignment of nanofibers can be controlled by adjusting the solution composition and processing parameters.[5,6] Various polymers including PVP,[7] poly(methyl methacrylate) (PMMA),[8] poly(lactic acid)[9] and poly(vinyl alcohol)[10] were successfully spun into nanofibers depending on a desired property or application. Many functional materials[11] such as magnetic nanoparticles,[12] gold nanoparticles,[13,14] carbon nanotubes,[15] metal oxide nanoparticles[16] and biomolecules[17] have been incorporated into nanofibers. Moreover, the surface of 1D materials can be modified with different functional groups and molecules.[18,19] The resulting composite of non-woven nanofibers has demonstrated great potential in applications for biosensing,[20] diagnostics,[21] tissue engineering[22] and wound dressing.[23]

Lanthanide doped UCNPs have gained interest as multifunctional light emitting composite materials[24] due to their properties of converting near-infrared light to UV-light or to visible light, and also for analytical applications.[25] Due to the near infrared excitation followed by anti-Stokes emission background luminescence can be minimized for higher signal-to noise ratios.[26,27] In comparison to UCNPs fluorescent dyes often have Stokes shifts of only 20–30 nm with a broad excitation and emission peak, limiting their application in surface-based sensing due to light scattering. Moreover, UCNPs show no blinking or photo-bleaching, which makes them interesting probes for bioanalytical systems. The host lattice and the composition of the UCNPs determine their luminescence properties. The most efficient while stable host lattice is the hexagonal $NaYF_4$ phase which has low phonon energies that reduce the non-radiative deactivation processes within the crystal and consequently increase the overall quantum yield.[28] The synthesis of UCNPs has improved significantly over the last years regarding the size, uniformity and luminescence properties of the particles.[29–31] For analytical applications, several surface modification techniques have been established.[32] Still, surface modifications and functionalization of the nanoparticles frequently lead to agglomeration and reduced colloidal stability in

aqueous dispersions. The majority of the nanoparticles are stabilized in aqueous systems by the negative charge of carboxylic acid groups degrading colloidal dispersibility at low pH values.[33] Solvent/buffer exchanges during analytical applications require time-consuming purifications steps such as centrifugation or dialysis, which are accompanied by a potential loss of nanoparticles and aggregation. Furthermore, since most sensor devices and applications using UCNPs until now have been intensity-based, fluctuations in the particle concentration lead to unfavorable uncertainties and a higher limit of detections. UCNPs have been successfully incorporated in PMMA,[34] in polystyrene,[35] PVP[36–39] poly(e-caprolactone)[40] and TiO_2 nanofibers.[41] Until now only a few applications have been reported, e.g. drug delivery[40,41] studies, where the nanofibers are used as vesicles and UCNPs as activators for drug release, and photodynamic therapy[42] or anti-counterfeit devices, by decorating Ag nanowires with the UCNPs.[43] Presley et al. reported an oxygen sensor based on the spectral overlap of a ruthenium complex with the emission of Tm^{3+} doped UCNPs embedded in polysulfone nanofibers[44] and Fu et al. investigated a detection system for microRNA.[45]

By incorporating nanomaterials such as luminescent nanofibers into microfluidic channels light scattering effects on the surface are increased preventing a sufficient signal response. Considering significantly inhomogeneous samples such as food, environmental and clinical samples fluorescence readout from a microfluidic channel may become even more complicated due to high background signals. UCNPs can significantly ameliorate this situation and minimize the background luminescence, since NIR light is used for excitation. Furthermore, due to the large anti-Stokes line-like emission scattering effects of the excitation light on the surface influence the optical readout only marginally. By entrapping the nanoparticles inside the nanofibers time consuming surface modifications are unnecessary. Solvent/buffer or sample preparation steps can easily be performed, without considering the colloidal stability of the particles. Since the particles are embedded inside the nanofibers in microfluidic channels, fluctuations of the particle concentration can be prevented, enabling successful online monitoring of the UCNPs luminescence.

In this work, we report electrospinning of PVP nanofibers with embedded UCNPs, optimization of the spinning process, and luminescence characterization of the nanolamp structures. Furthermore, their application for online monitoring was demonstrated in microfluidic flow channels as the nanolamps respond deliberately and sensitively to changes in the aqueous environment.

6.3 Experimental Section

Chemicals

Ammonium fluoride (>98%), polyvinylpyrrolidone (PVP, Mw = 1 300 000), HEPES (99.5%) erbium(III) chloride hexahydrate (99.9%), ethanol (>99.8%), deuterium oxide (99.9%), poly(acrylic acid) (PAA) (MW 2100), Rose Bengal and nitrosyl tetrafluoroborate (95%) were purchased from Sigma Aldrich (www.sigmaaldrich.com). 1-Octadecene (90%) and oleic acid (90%) were bought from Alfa Aesar (www.alfa.com). Sodium hydroxide (98-100%), acetic acid (100%), phosphoric acid (85%), potassium chloride (99.5%) and disodium hydrogen phosphate (99.5%) were purchased from Merck (www.merck.de). Cyclohexane (99.5%), dimethylformamide (DMF, 99.5%), and chloroform (99.8%) were obtained from Acros Organics (www.acros.com). Yttrium chloride hexahydrate (99.99%), ytterbium chloride hexahydrate (99.99%) and gadolinium chloride hexahydrate (99.99%) were bought from Treibacher Industrie AG (www.treibacher.at). Clear Tygon Micro Bore PVC Tubing (0.51 mm ID, 1.52 mm OD, 0.51 Wall) was used for the microfluidics. The tubes were glued with superglue (Pattex) to the microfluidic channel. Plexiglas (PMMA) plates (5 cm × 5 cm × 0.15 cm) were purchased from Evonik (www.plexiglas.de). For all experiments, double distilled water was used.

Instrumental

The size of the synthesized $NaYF_4$ nanoparticles was determined by dynamic light scattering (DLS) and transmission electron microscopy (TEM). DLS-measurements were performed in semimicro disposable poly(methyl methacrylate) (PMMA) cuvettes on a Malvern Zetasizer Nano ZS (www.malvern.com). DLS spectra of particles dispersed in DMF and all other optical measurements were accomplished in precision cells made of quartz glass Suprasil from Hellma (www.hellma-analytics.com). Each measurement was performed three times with at least 12 sub runs. TEM images were generated with a 120 kV Philips CM12 microscope and were evaluated with ImageJ and Origin 8.

The luminescence spectra were acquired on an Aminco Bowman AB2 spectrometer (Thermo Electron Corporation, www.thermofisher.com) coupled with a 200 mW cw laser (980 nm) (www.picotronic.de).

UV/VIS absorption spectra were recorded with a Perkin-Elmer (www.perkinelmer.com) Lambda 14P UV/VIS spectrometer.

An inductively coupled plasma optical emission spectrometer Spectroflame EOP from Spectro (www.spectro.com) was used to determine the composition and the exact mass

concentration of the nanoparticles. For this purpose, approximately 0.3 mg of the nanoparticles were dried at 70 1C in an oven. The precipitate was dissolved in 417 mL of sulfuric acid (96%) assisted by 15 min of sonication. The solution was diluted with double distilled water to 7.5 mL ($c(H_2SO_4) = 1$ M) and afterwards with 1 M nitric acid to 15 mL. The final concentration of sulfuric acid and nitric acid was 0.5 M. The emission wavelengths for the lanthanide ions were 363.312 nm for yttrium, 342.247 nm for gadolinium, 349.910 nm for erbium and 401.225 nm for ytterbium.

Lifetime measurements were performed with a 980 nm (cw, 200 mW) laser module and an optical chopper (MC2000 with a two slot chopper blade MC1F2) from Thorlabs. The signal was amplified with a photomultiplier tube from PreSens (www.presens.de) and analyzed by using a digital storage oscilloscope (DSO 8204) from Voltcraft. Optical bandpass filters (FF01-535/150-25 and FF01-665/150-25) from Semrock were used for measuring luminescence decay times for the green (541 nm) and the red emission (656 nm).

Nanofibers were produced with an electrospinning device from Spraybase (www.spraybase.com). The activation of the PMMA substrate with O_3 was carried out with a UVO-Cleaner Model 144 AX-220 Series from Jelight Company Inc. (www.jelight.com).

A Specac Manual Hydraulic Press with Atlas Heated Platens (P/N GS15515) was used for hot embossing and bonding of the microfluidic device (www.specac.com).

A KD Scientific Legato 180 Dual Syringe Pump was used for microfluidic systems (http://www.kdscientific.com).

Confocal laser scanning microscopy was carried out with a C1 confocal system equipped with a Nikon Eclipse 90i and a laser diode module (www.nikoninstruments.com). Images were evaluated by ImageJ software.

A Leica microscope was used for light microscopy images (www.leica.de).

X-ray powder diffraction (XRD) patterns were collected using a Huber Guinier G670 diffractometer with a Cu source (Kα radiation of 1.54060 Å). The measurements were made at 40 kV and 30 mA with a resolution of 0.005° (2θ).

Synthesis of upconversion nanoparticles

Synthesis of β-NaYF$_4$ (20% Yb, 2% Er, 10% Gd) nanoparticles. The synthesis of Ln^{3+} doped NaYF$_4$ UCNPs is based on a reported procedure.[46] The following description is for 5 mmol of total rare earth chlorides. The synthesis was performed in a 250 mL three-necked round bottom flask under nitrogen flow. 1031.42 mg of YCl$_3$·6 H$_2$O (3.4 mmol) were dissolved together with 387.49 mg of YbCl$_3$·6 H$_2$O (1 mmol), 38.17 mg of ErCl$_3$·6 H$_2$O (0.1 mmol) and 185.65 mg of GdCl$_3$·6 H$_2$O (0.5 mmol) in 30 mL of methanol. 40 mL of oleic acid and 75 mL of octadecene were added and the cloudy solution was heated to 160 °C by a heating mantle with temperature control. The reaction mixture was stirred for 30 min in vacuo (200 Pa) at 160 °C in order to obtain a clear solution of the oleate coordinated yttrium and lanthanide ions. Then, the solution was cooled to room temperature. Afterwards, a solution of 0.74 g of NH$_4$F (20.0 mmol) and 0.5 g of NaOH (12.5 mmol) in 50 mL of methanol was added. The suspension was heated up to 120 °C for 30 min to remove the methanol. A reflux cooler was assembled and the solution was heated to 325 °C to induce the growth of the nanoparticles. As soon as the temperature reached 300 °C, a timer was started and the occurring luminescence of the UCNPs was controlled with a 980 nm laser module (200 mW, cw). After the first luminescence was visible the nanoparticles were stirred for another 10 min for growth and self-focusing (Ostwald ripening). The solution was cooled to room temperature and the particles were precipitated by addition of ethanol (≈200 mL). The purification was done under air. The white particles were collected by centrifugation (1000 g, 5 min). The precipitate was dispersed twice in 20 mL chloroform and precipitated again with ethanol (≈200 mL). This washing step was repeated with cyclohexane and acetone until a clear solution in cyclohexane was obtained. In the last step, the particles were dissolved in 40 mL of cyclohexane and large aggregates were separated from the nanoparticle suspension by centrifugation (1000 g, 2 min). The oleate-capped nanoparticles were stored at 4 °C in a refrigerator.

Synthesis of α-NaYF$_4$ nanoparticles. The synthesis was prepared in a three-necked round bottom flask under nitrogen flow. 3033.6 mg of YCl$_3$·6 H2O (10 mmol) was dissolved in 20 mL methanol. 80 mL of oleic acid and 150 mL of octadecene were added and the cloudy solution was heated up to 160 °C by a heating mantle with temperature control. The reaction mixture was stirred for 30 min in vacuo (200 Pa) at 160 °C in order to obtain a clear solution of the oleate-coordinated precursors and then was cooled to room temperature. Afterwards, a solution of 1.48 g of NH$_4$F (40.0 mmol) and 1 g of NaOH (25 mmol) in 40 mL of methanol was added. The white suspension was heated to 120 °C for 30 min to remove the methanol. The clear solution was heated to 240 °C to induce the

growth of the nanoparticles. After 30 min the solution was cooled to room temperature and the particles were purified like the core particles under air.

Synthesis of NaYF$_4$ (20% Yb, 2% Er, 10% Gd)@NaYF$_4$ nanoparticles. The synthesis was prepared in two three-necked round bottom flasks under nitrogen flow. 0.5 mmol of the NaYF$_4$ (20% Yb, 10% Gd, 2% Er) core particles were heated together with 2.5 mL of oleic acid and 2.5 mL of octadecene to 120 °C. 1 mmol of the shell-material dispersed in a few milliliters of cyclohexane was heated with 5 mL of oleic acid and 5 mL of octadecene also to 120 °C. The reaction mixtures were stirred for 30 min in vacuo (200 Pa) at 160 °C in order to remove cyclohexane. While the mixture of the core particles was heated to 325 °C under reflux cooling, the shell material was kept at 120 °C. The shell material was injected stepwise (0.5, 1, 1.5 and 2 mL) to the core particles. The time period after each injection was 10 min. During the injection of the shell material the temperature has to be above 300 °C to obtain a homogeneous shell growth. After the last injection the particles were stirred for another 10 min at reflux and were then cooled to room temperature. The particles were purified via centrifugation like the core particles.

Leakage of UCNPs from microfluidic channels

Double distilled water was flown through the microfluidic channel containing the modified nanofibers (40 mg·mL^{-1}, spinning time 15 min) at a flow rate of 25 μL·min^{-1}. The solution was collected for 3 h and prepared for ICP-OES measurements after drying in an oven at 70 °C. With a detection limit of 600 nM (0.0533 μg·mL^{-1}) for Y^{3+}-ions no leakage of the UCNPs from the nanofibers and from the microfluidic channel was observed. Y^{3+} ions were chosen since they have the highest concentration inside the nanocrystals.

Surface modification of NaYF$_4$ nanoparticles

For the preparation of uncapped NaYF$_4$ particles a ligand exchange method was used. Equal volumes of cyclohexane, containing the oleate capped upconversion nanoparticles, and DMF were stirred at 30 °C. Nitrosyl tetrafluoroborate was put directly into the stirring solution (one mg NOBF$_4$ was inserted per one mg nanoparticle). NOBF4 led to a protonation of the oleate, leading to a detachment of the ligand from the particle surface. The uncoated nanoparticles are at the same time stabilized by BF$_4^-$ ions in the DMF phase. After 15 min of stirring at 30 °C, the upper phase (cyclohexane) was removed and the DMF phase was washed with an excess of chloroform (10-20 mL). After being centrifuged (1000 g, 5 min), the jelly-like precipitate was washed again with 1-2 mL of DMF and chloroform (10-20 mL). In the last step, the particles were dispersed in the

desired volume of DMF and aggregates were separated by centrifugation (1000 g, 3 min). The uncapped nanoparticles were stored in the dark at 4 °C in the refrigerator.

Preparation of the spinning solution

The spinning solutions were prepared by dissolving 14% (w/v) of PVP in DMF (2.5 mL) containing the desired mass concentration of UCNPs. The dispersion was sonicated for 30 min at 60 °C to form a clear solution, then 2.5 mL of ethanol was added and the polymer solution was stirred overnight at room temperature.

Electrospinning of nanofibers

The spinning solution was loaded into a 5 mL FORTUNAs OPTIMAs glass syringe. The polymer solutions were pumped with 0.003 mL·min^{-1} through PTFE tubing with a 26 gauge needle at its end. The temperature for electrospinning was ideally between 20 °C and 25 C. Relative humidity should not exceed 50%. The distance between the needle and the grounded collector plate was 15 cm, the voltage was set to 14.5 keV.

Transferring of the nanofiber mats to a microfluidic device

For transferring the nanofibers to the microfluidic channel the fibers were electrospun on a metallic wire with a mirror of 2 cm × 3 cm. The fiber mat was collected for 15 min. Then, the fiber mat was heat treated for 5 h at 175 1C in a drying cabinet. The brass template with raised channels measuring 30 mm × 1 mm × 50 mm was fabricated using a Kern Evo micromilling machine (www.kern-microtechnik.com). Microfluidic channels were embossed into PMMA sheets. The hot press was heated to 110 C. The brass mold was placed on top of the PMMA sheet. Then, the upper hot plate was moved to touch the mold for about 30 s. Next a pressure of about 100 kg was added for 5 min. The pressure was carefully released and the sandwich was allowed to cool on the bench for 2–3 min. Inlet holes were drilled into the PMMA using a 1.2 mm drill bit. PMMA plates were activated in an ozone generator (oxygen flow rate 0.5 L min^{-1}) and with UV-light for 10 min. For the fabrication of the microfluidic device containing the modified nanofibers the temperature of the hot press was set to 80 C. On the bottom PMMA sheet (containing the microfluidic system) the nanofiber mat was placed in the middle of the microfluidic system. A cover plate was added and both plates were thermostatically controlled for 5min. A pressure of 500 kg was applied for 5 min and afterwards the plates were allowed to cool to room temperature.

6.4 Results

6.4.1 Spinning of PVP Nanofibers

The generation of optically functional nanofibers for analytical applications was achieved by choosing a polymer and UCNPs that share similar solubility/dispersibility properties. The aim was to produce thin and uniform nanofibers, containing a large number of UCNPs for high luminescence yields. PVP nanofibers can be spun from PVP dissolved in DMF/ethanol (1 : 1 v/v) mixtures resulting in nanofiber diameters in the range of 100-400 nm.[47] The influence of spinning composition and process parameters was initially studied. Specifically, the morphology of the nanofibers was optimized regarding PVP concentration, flow rate and voltage (**Table 6.1**).

Table 6.1‖ Conditions for optimized solution and processing parameters for electrospun PVP nanofibers.

Concentration (w/v)	Flow rate ($\mu L \cdot min^{-1}$)	Voltage (kV)	Morphology
9	1	7-9	bead
	3	7-9	bead
	5	8-10	bead
	8	6-11	bead
	10	7-12	bead
10	1	11-13	bead
	3	11-13	bead
	5	8-11	bead
	8	8-10	bead
	10	11-13	bead
11	1	9-11	bead
	3	8-12	bead
	5	9-11	bead
	8	8-10	bead
	10	7-9	bead
12	1	8-10	bead
	3	8-10	bead
	5	8-10	bead
	8	9-11	bead
	10	8-11	bead
13	1	8-10	bead
	3	7-9	bead
	5	7-9	bead
	8	6-11	bead
	10	7-12	bead
14	1	9-11	smooth
	3	8-10	smooth
	5	8-12	smooth
	8	8-14	smooth
	10	6-17	smooth

Light microscopy images of PVP nanofibers spun at different concentrations of PVP are shown in **Figure 6.3**. As the fiber thickness generally increases with increasing polymer concentration/viscosity the lowest possible PVP concentration was sought.[48] A PVP concentration of 14% (w/v) resulted in non-beaded nanofibers of high uniformity and was chosen for all further studies. Lower polymer concentrations resulted in the formation of polymer beads and inhomogeneous nanofibers.

6.4.2 Synthesis and Surface Modification of UCNPs

$NaYF_4$ nanoparticles doped with Yb^{3+}, Gd^{3+} and Er^{3+} ions were synthesized via a thermal decomposition method combined with an Ostwald ripening strategy in high boiling solvents. The monodisperse particles have an average diameter of 21.9 ± 0.8 nm according to TEM-images and a solvodynamic diameter of 24.7 ± 3.3 nm (polydispersity index (PDI): 0.137) regarding DLS measurements in cyclohexane (**Figure 6.3**). $NaYF_4$ can crystallize in two different phases, the cubic (a) and the hexagonal phase (b). The hexagonal phase is thermodynamically more stable and has an overall larger brightness.[49] The desired hexagonal phase of the successfully synthesized nanoparticles was confirmed by XRD-measurements (**Figure 6.2**).
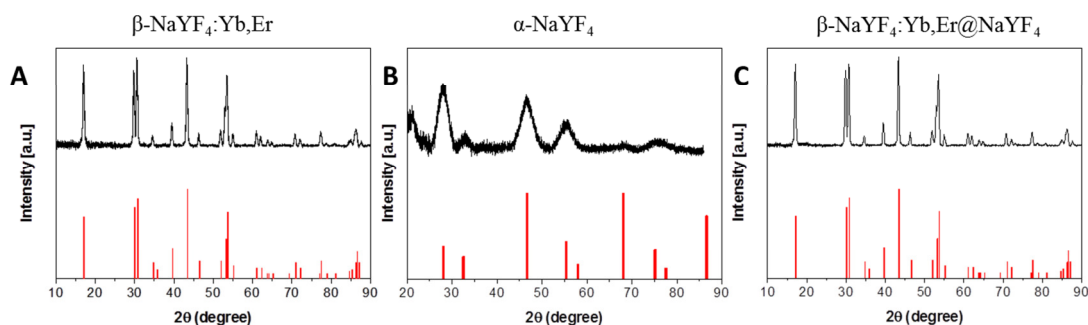

Figure 6.2 ‖ **A**) XRD patterns of β-$NaYF_4$ (20% Yb, 10% Gd, 2% Er (21.9 nm, black) and a reference pattern of β-NaYF4 (red, JCPDS no. 16-0334). **B**) XRD patterns of cubic α-$NaYF_4$ nanoparticles (black) and a reference pattern of α-$NaYF_4$ (red, JCPDS no. 039-0724). **C**) XRD patterns of β-$NaYF_4$ (20% Yb, 10% Gd, 2% Er)@$NaYF_4$ (25.5 nm, black) and a reference pattern of β-$NaYF_4$ (red, JCPDS no. 16-0334).

After NIR excitation at 980 nm the particles show the typical anti-Stokes emission of Yb,Er-doped UCNPs, a red emission at 656 nm ($^4F_{9/2}$ - $^4I_{15/2}$) and two green emissions at 541 nm ($^4S_3/2$ - $4I15_{/2}$) and 526 nm ($^2H_{11/2}$ - $^4I_{15/2}$) (**Figure 6.4**). $NaYF_4$:Yb,Er,Gd@$NaYF_4$ core–shell nanoparticles were synthesized in order to obtain higher luminescence brightness. A $NaYF_4$ shell increases the luminescence intensity due to minimization of surface defects and reduction of solvent quenching effects.[50] For growing a shell around the UCNPs cubic $NaYF_4$ (2–3 nm) nanoparticles were synthesized to serve as the shell

material (**Figure 6.2**). The smaller cubic nanoparticles are thermodynamically less stable than the larger core particles due to their higher surface-to-volume ratio.[51] The α-NaYF$_4$ particles were consequently dissolved and grew a shell around the core particles, increasing the total diameter of the particles by 3.6 ± 0.9 nm. The core–shell particles were shown to have an average diameter of 25.5 nm ± 0.9 nm and a solvodynamic diameter of 29.9 ± 9.2 nm (PDI: 0.098, **Figure 6.3**). The hexagonal phase of the core–shell nanoparticles was again proven with XRD-measurements (**Figure 6.1**). The mass concentration and the exact composition of all particles were determined by ICP-OES measurements (**Table 6.2**).

Table 6.2 ‖ The composition of the core NaYF$_4$:Yb,Er,Gd and the core-shell NaYF$_4$:Yb,Er,Gd@NaYF$_4$ nanoparticles as determined by ICP-OES measurements.

lanthanide ions	Y^{3+}	Yb^{3+}	Gd^{3+}	Er^{3+}
composition core particles [%]	68.2	19.9	9.9	2.0
composition core-shell particles [%]	84.2	9.7	5.2	1.0

Subsequently, the surface of the oleate capped particles and core–shell particles were modified to enable colloidal stability inside the spinning solution. A ligand exchange was performed in a two-phase system of cyclohexane and DMF. The modified nanoparticles show no tendency of agglomeration as proven by DLS measurements (**Figure 5.3**).
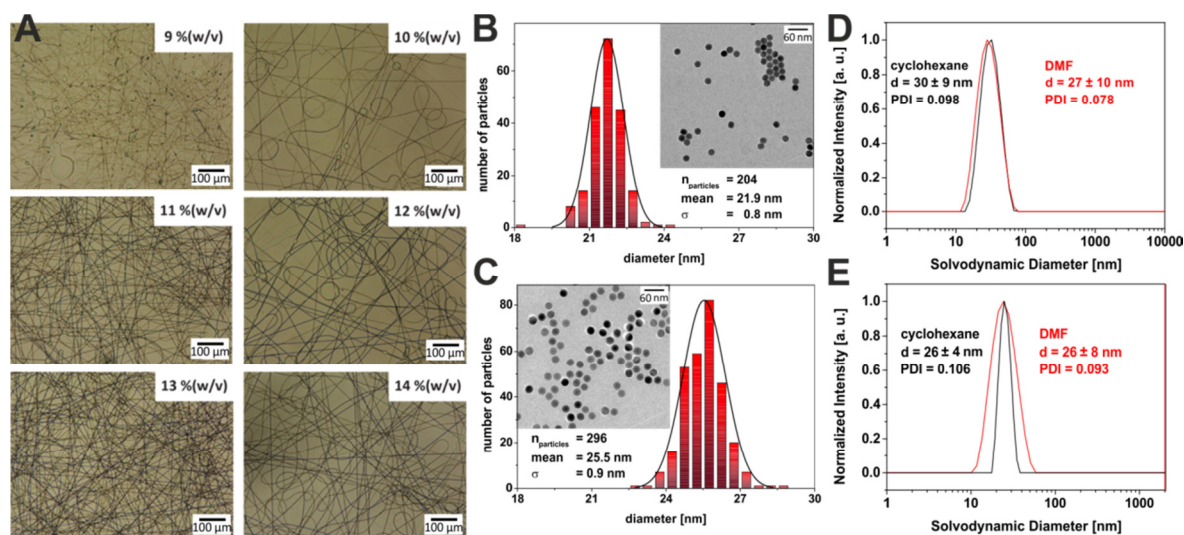
Figure 6.3 ‖ **A**) Light microscopy images of PVP nanofibers spun on glass slides with different PVP concentrations (9 to 14% (w/v)). The sizes of the NaYF$_4$:Yb,Er,Gd (**B**) core and NaYF$_4$:Yb,Er,Gd@NaYF$_4$ (**C**) core–shell nanoparticles were determined considering the TEM images with the related histograms of the particle-size-distribution. DLS-measurements of the core (**D**) and core–shell particles (**E**) dispersed in cyclohexane and in DMF after surface modification.

The luminescence properties of equivalent numbers of core particles and core–shell particles in the spinning solution were compared, regarding the Yb^{3+} by ICP-OES measurements. It was found that the core–shell particles enhance the luminescence intensity significantly (by a factor of 12), as expected, due to reduced surface quenching effects (**Figure 6.4**). Moreover, the luminescent lifetime of the core–shell nanoparticles compared to the core particles increased from 100 to 279 µs for the green and from 183 to 377 µs for the red emission, confirming also successful shell growth (**Figure 6.4**).
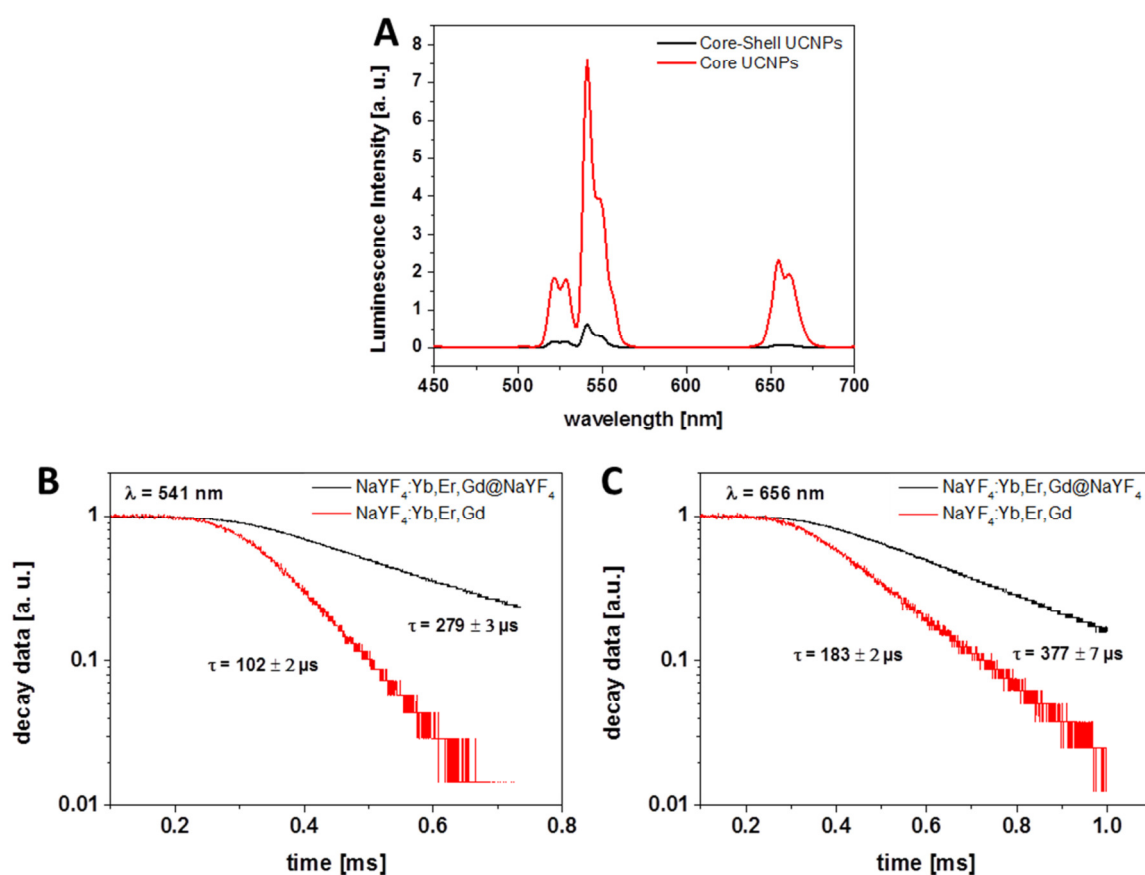
Figure 6.4 ‖ A) The luminescence spectra of the core (NaYF$_4$:Yb,Er,Gd) and the core-shell (NaYF$_4$:Yb,Er,Gd@NaYF$_4$) particles inside the spinning solution (14%(w/v) PVP, 1:1 DMF/ethanol, UCNPs) were compared. The spectra were normalized to the same number of nanoparticles regarding ICP-OES measurements. **B,C**) Cut and normalized decay data of core and core-shell nanoparticles dispersed in the spinning solution. The luminescence decay of the green upconversion emission around 541 nm (B) and the red emission around 656 nm (**C**) were recorded. The particles were excited with a 980 nm cw laser (200 mW).

6.4.3 Embedding of UCNPs inside the Nanofibers

In general, two different strategies have been described for the incorporation of nanoparticles into nanofibers: the direct embedding of nanoparticles in the spinning solution, and the sintering of nanoparticle precursor material inside the nanofibers. With the sintering method high and homogenous particle loading in the nanofibers can be achieved, however temperatures of 500–800 °C[52,53] make the nanofibers brittle, hindering a successful transfer of the fiber mat. For the embedding of the nanoparticles in the spinning solution the surface of the UCNPs must be adapted for colloidal stability. Reports published up to date neglect colloidal stability as an important parameter. Hence the concentration of the particles inside the spinning solution was restricted to about 5 mg·mL^{-1}, resulting in low particle loading in electrospun nanofibers.[39,40] Furthermore, the particles inside the nanofibers show no homogenous distribution and form clusters inside the nanofibers.[41] Instead, here the UCNP synthesis and functionalization process were matched to the nanofiber electrospinning process. Consequently, the electrospinning process itself was not affected by the presence of UCNPs in the spinning dope. Thus, UCNP concentrations up to 40 mg·mL^{-1} dispersed in the polymer solution can be spun into uniform fibers. TEM images show a random distribution of the particles inside the fibers without forming agglomerates (**Figure 6.5**). It is assumed that all particles were entrapped or associated with the nanofibers, as no free particles were found in the TEM images. The diameter of the nanofibers was 170 ± 80 nm and was not influenced by doping with the particles. The luminescence of the nanofibers is correlated with particle content. The amount of nanoparticles inside the nanofibers can be controlled by the amount of particles doped into the spinning solution. Specifically, a linear relationship was found by plotting the mass concentration against the number of the particles inside the nanofibers (up to 12,000 particles in one mm^3). At this point, the concentration of UCNPs in nanofibers is only limited by their dispersibility in DMF, i.e. at concentrations above 80 mg·mL^{-1} UCNPs aggregate during the surface modification with NOBF$_4$. The theoretical concentration of the UCNPs inside the nanofibers was calculated to be 254 ± 9 mg·mL^{-1} for the highest concentrated spinning solution (i.e. 40 mg·mL^{-1}) or to express it differently, considering the density of NaYF$_4$ in a nanofiber 0.34 ± 0.01 mg mm^{-1} UCNPs are embedded along the length scale of the nanofibers. Even by considering the low fiber density of 10% in the fiber mats, the mass concentration inside the fiber mat is about five times higher than the common mass concentration of UCNPs achieved in aqueous solutions (up to 5 mg mL^{-1}).[44] Consequently, electrospinning of UCNPs into PVP nanofibers is an excellent method to obtain high particle concentrations even in aqueous solutions. It is also worth mentioning that the embedment of nanoparticles into nanofibers

by NOBF$_4$ assisted surface modification is not restricted to UCNPs and can be adapted for example for CoPt, Bi$_2$S$_3$, Fe$_3$O$_4$ and FePt nanoparticles.[36]
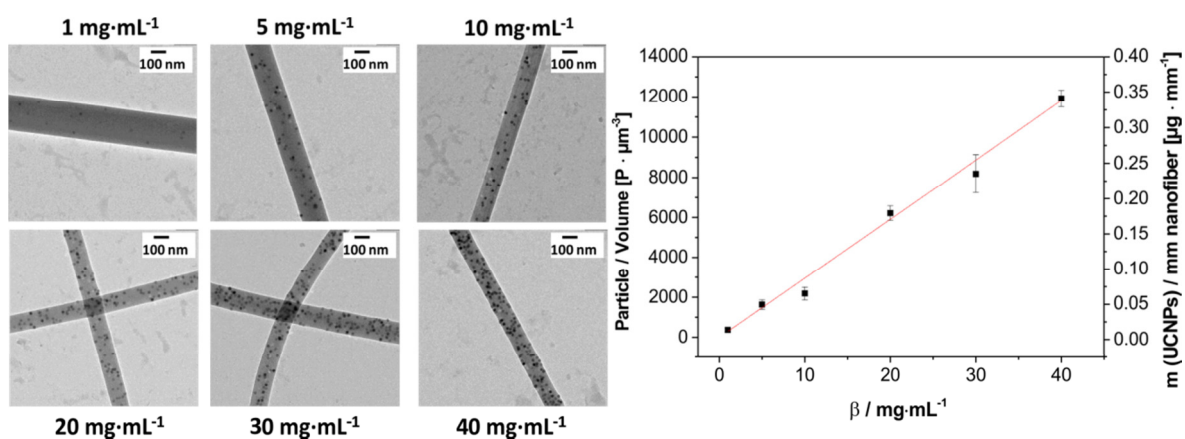
Figure 6.5‖ TEM images of PVP (14% (w/v)) nanofibers containing UCNPs are shown. The concentration of the UCNPs in the spinning solutions varied from 1 to 40 mg·mL^{-1}. On the right the mass concentration of the spinning solution was plotted against the number of particles inside the nanofibers. The particle to volume ratio was evaluated with ImageJ. The mass of the UCNPs inside a nanofiber of 1 mm was calculated with the density of NaYF$_4$ and the number of particles inside the nanofibers. For each mass concentration, several TEM-images (5–6) were analyzed for the calculation.

6.4.4 Transfer to a Microfluidic System

After electrospinning the PVP fibers are stacked together to form fiber mats. Long spinning times result in an uneven pore distribution of the nanofiber mats on the collector wire.[54] Therefore, around 5 mm thick mats were spun and the desired thickness generated by simple overlaying of the mats prior to heat treatment and bonding into the microfluidic channels. Heat treatment of the PVP nanofibermat at 175 °C was necessary for crosslinking of the nanofibers, yielding mechanically stable nanofiber mats insoluble in water.
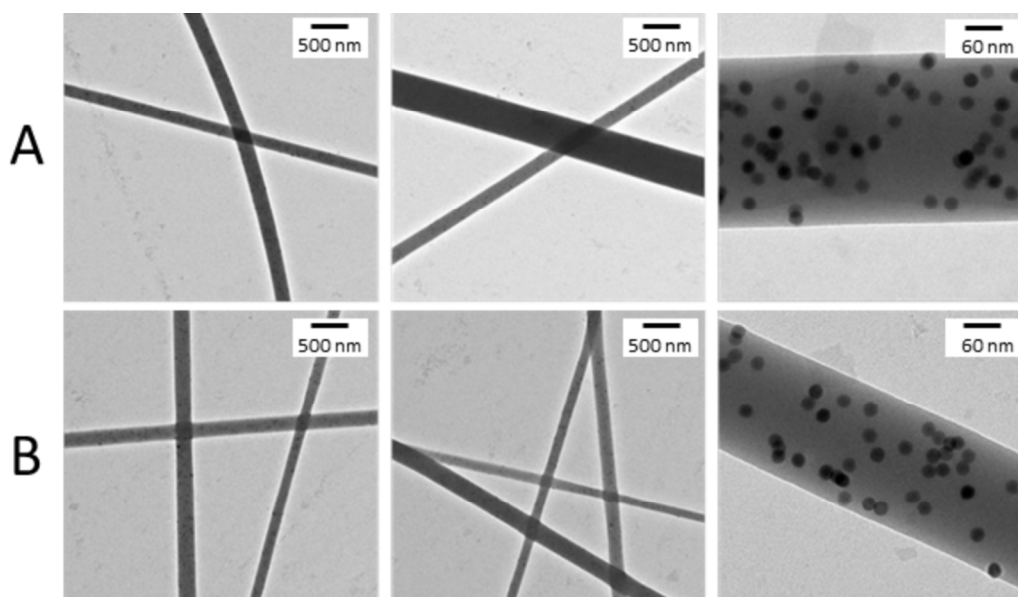

Figure 6.6‖ TEM-images of the PVP nanofibers containing 10 mg·mL^{-1} UCNPs. **A**) shows the morphology of the nanofibers before and (**B**) after heat-treatment. The diameter of the fibers and the distribution of the UCNPs inside the nanofibers are comparable, additionally in (**B**) cross-linking of the PVP nanofibers occurs.

The corresponding TEM images (**Figure 6.6**) show the UCNP containing nanofibers before and after heat treatment. The diameter of the fibers was not affected by the heat treatment; however, crosslinking can be observed on overlying nanofibers (**Figure 6.6B**). The distribution of the UCNPs inside the nanofibers was not influenced by the heat-treatment. The nanofiber mats were transferred to the microfluidic system using a hot embossing method (**Figure 6.8**). PMMA sheets were used due to their high optical transmission for NIR light and for visible light.[55] The morphology of the fibers inside the microfluidic channel was investigated using confocal microscopy measuring the scattered light from the nanofibers. **Figure 6.7** shows a dense permeable network of nanofibers inside the microfluidic channel indicating the successful transfer of the nanofibers.
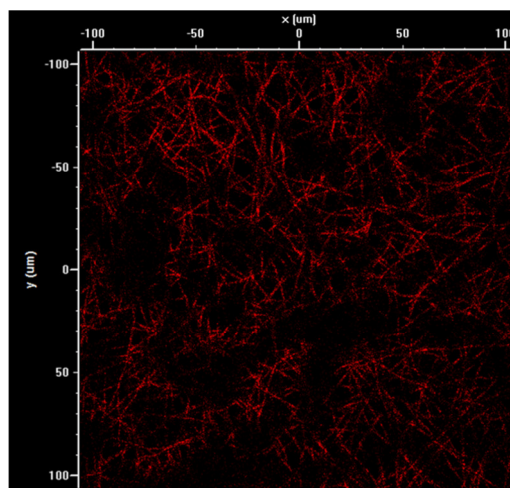
Figure 6.7‖ UCNP-nanofibers embedded in a microfluidic channel while excited at 543 nm. The scattered light caused by the nanofibers was collected with a long pass filter at 650 nm.

6.4.5 Stability of PVP Nanofibers within the Microfluidic

Important factors for a successful sensor application are the mechanical stability of the nanofibers inside the microfluidic channels and leak-free entrapment of the UCNPs. Thus, the stability of the modified nanofibers inside the microfluidic channel was investigated. The morphology of the fibers was obtained before and after water flow with a confocal microscope. It was observed that the fibers were not washed out from the microfluidic channel retaining their local position (**Figure 6.8**). Using ICP-OES measurements leakage of the UCNPs from the nanofibers was excluded.

Figure 6.8‖ The morphology of PVP nanofibers (20 mg·mL^{-1}, 10 min) were investigated inside themicrofluidic channel, (**A**) the nanofibers before the water flow, (**B**) during water flow and **C**) after drying of the microfluidic channel.

6.4.6 Luminescence Properties

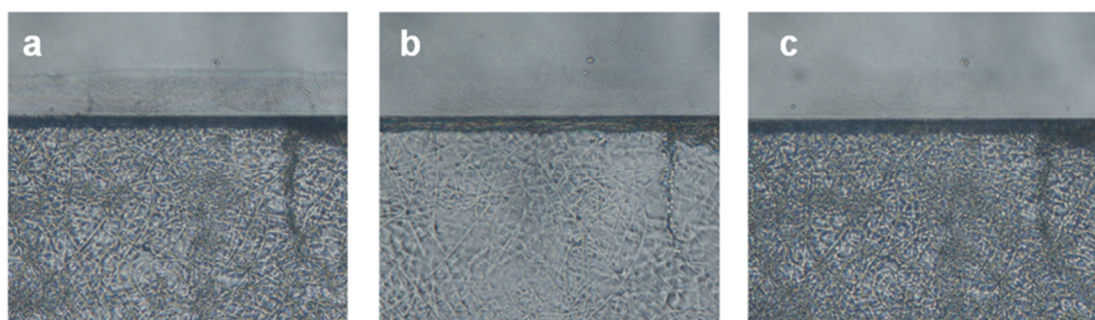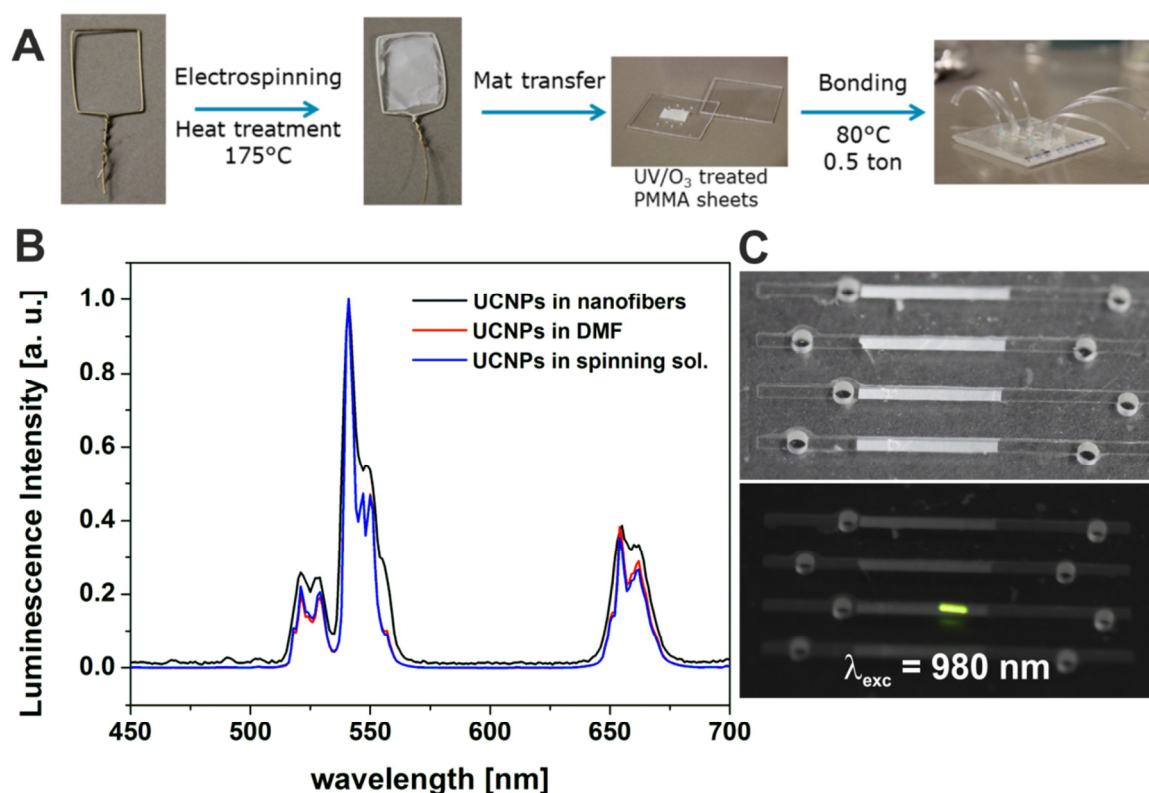**Figure 6.9 ‖ A**) The transfer of the PVP nanofibers to the microfluidic channel is shown. **B**) On the left side, the luminescence spectra of the upconversion nanoparticles were compared among the $NOBF_4$-modified nanoparticles dispersed in DMF, the particles dispersed in the spinning solution and the UCNPs embedded in the PVP nanofibers. **C**) On the right side, PVP nanofibers containing UCNPs in the microfluidic channel are shown. Under NIR excitation the green luminescence of the UCNPs is visible. The nanoparticles were excited with a 980 nm cw laser (200 mW).

The luminescence properties of the UCNPs in DMF, in the spinning solution and inside the nanofibers were compared to determine possible entrapment effects. All spectra showed the typical line-like emission from Er-doped UCNPs (**Figure 6.9**). Compared to organic dyes, only a very small peak broadening occurred due to the scattered light. Precisely, for example the FWHM of the red peak broadens from 12.7 nm for the particles in DMF to 16.1 nm for the particles inside the nanofibers. The bright green luminescence of the UCNPs embedded inside the nanofibers can even be clearly seen by naked eye upon NIR excitation. In contrast to particle flow systems the luminescence intensity of the UCNPs is not influenced by particle fluctuations caused by several preparation steps. Buffer exchanges and binding steps can be performed easily saving time and enabling high reproducibility. PBS, HEPES (50 mM, pH 7.4) and TRIS buffer (50 mM, pH 7.4) were flown subsequently through the microfluidic channel. The luminescence intensity of the

UCNPs embedded in the nanofibers was not influenced while flowing different buffers (**Figure 6.11**). Moreover, the luminescence signal of the nanolamps was also not affected by the different pH values of the Britton–Robinson buffers (pH 2–12). Overall, the luminescence signal in the microfluidic channel fluctuates only about 1.3% over 1 h of solvent flow, demonstrating the robustness of the system. In contrast, the luminescence intensity of the PAA coated core nanoparticles (21.9 nm) in cuvettes (**Figure 6.10**) shows severe signal fluctuations in various buffers and at different pH values due to aggregation or even immediate precipitation. This demonstrates that the surface modification strategy leads to the colloidal stability of dispersed particles only under restricted conditions (e.g. pH, temperature, ionic strength, solvents) whereas the nanofiber embedded particles remain unaffected.
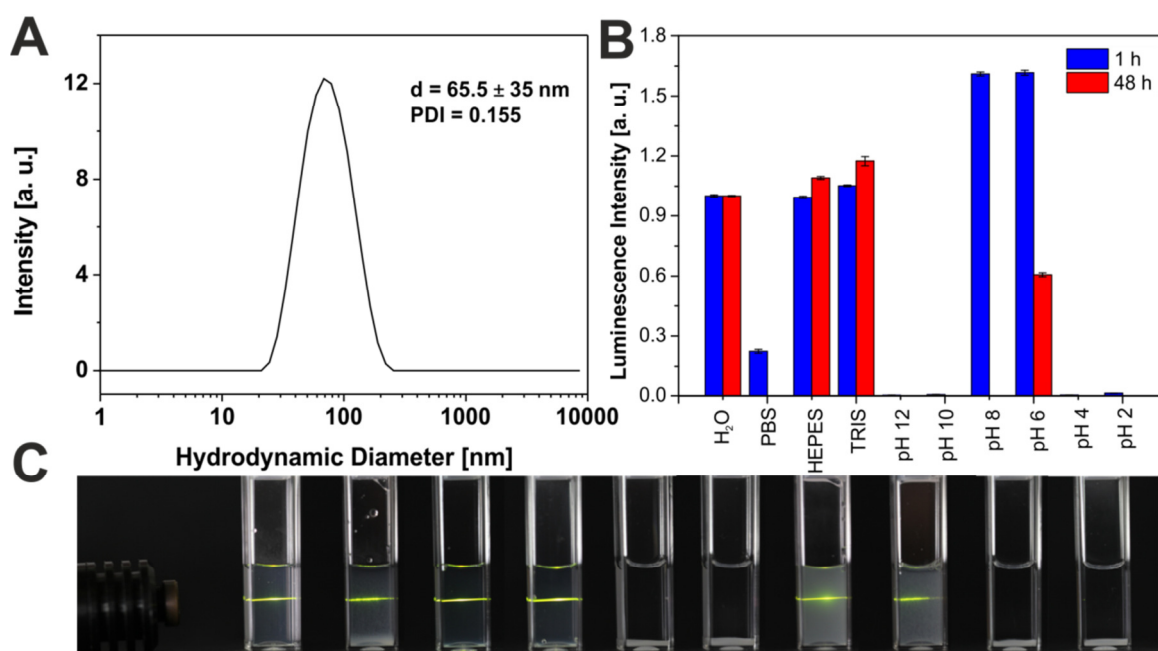
Figure 6.10‖ A) DLS measurements of polyacrylic acid coated $NaYF_4$:Yb,Er,Gd in double distilled water. The hydrodynamic diameter was 65.5 ± 35 nm with a polydispersity index of 0.155. **B**) The luminescence intensity of $NaYF_4$:Yb,Er,Gd nanoparticles in different aqueous dispersions was measured at 541 nm (n = 10). The PAA modified nanoparticles were excited with a 980 nm laser module (cw, 200 mW). The measurements were performed 1 h and 48 h after their surface modification. The particles were dispersed in double distilled water, PBS buffer, HEPES buffer (50 mM, pH 7.4), TRIS buffer (50 mM, pH 7.4) and Britton-Robinson buffers of different pH (0.04 M H_3PO_4, 0.04 M acetic acid, 0.04 M boric acid, pH 12-2). The mass concentration of the particles was 2 mg·mL^{-1}. **C**) Images of PAA modified particles in different aqueous dispersion under NIR excitation 1 h after synthesis. From left to right the particles were dispersed in double distilled water, PBS buffer, HEPES buffer (50 mM, pH 7.4), TRIS buffer (50 mM, pH 7.4) and Britton-Robinson buffers of different pH (0.04 M H_3PO_4, 0.04 M acetic acid, 0.04 M boric acid, pH 12-2).

6.4.7 Online Monitoring of UCNPs in Microfluidic Channels

As seen, the luminescence intensity of the UCNPs remains constant inside the microfluidic channel throughout any flow manipulation. The immediate response of the particles to the solution around the nanofibers was then demonstrated taking advantage of the different luminescence behaviors of the UCNPs in H_2O and D_2O (**Figure 6.11**). Generally, upon changing the solvent from D_2O to H_2O a significant decrease in the luminescence of dispersed UCNPs occurs due to water quenching of the luminescence and a local absorption band of water at 980 nm (**Figure 6.12**). Specifically, in comparison to the low energy vibrational modes of the O–D bonds quenching through the O–H bonds of water is strongly increased.[46] Since the optical pathway inside the microfluidic channel is only 50 mm, the laser energy absorbance caused by water inside the microfluidic channel is reduced to a value of 0.001 ($\varepsilon_{980\,nm} = 3.6 \times 10^{-3}$ L·mol^{-1}·cm^{-1}) and can be neglected. The observed changes in measured luminescence are therefore only caused by the surface-interaction of D_2O with the UNCPs. This can be observed when injecting D_2O and H_2O consecutively into the microfluidic channel. The exchange of D_2O by H_2O reduces the luminescence signal of the UCNPs by a factor of three. It is assumed that the water quenching affects primarily the particles attached to the surface or near the surface (<10 nm) of the nanofibers. The signal changes were fully reversible upon flushing alternatively H_2O and D_2O through the system. A full signal response was recorded after 2.5 min, showing a fast signal response. At the beginning of the measurement a small signal drift of the luminescence signal of the UCNPs occurred. Since leakage of the particles was excluded with ICP-OES measurements one explanation can be an incomplete wetting of the nanofibers at the beginning due to the entrapment of minimal pockets of air. Overall, this D_2O/H_2O study proves that the nanofibers within the nanofiber mats were immersed completely by the solvent, making the high surface to volume ratio of the nanofibers inside the microfluidic channel accessible for further modifications. The signal response of the nanoparticles embedded within the nanofibers in the microfluidic channel was investigated further with a fluorescent dye in order to demonstrate the functionality of the nanolamps as a light source for analytical applications in microfluidic systems. Rose Bengal (RB) was chosen as the model dye since its absorption band overlaps only with the green emission of the UCNPs (541 nm, **Figure 6.12**).
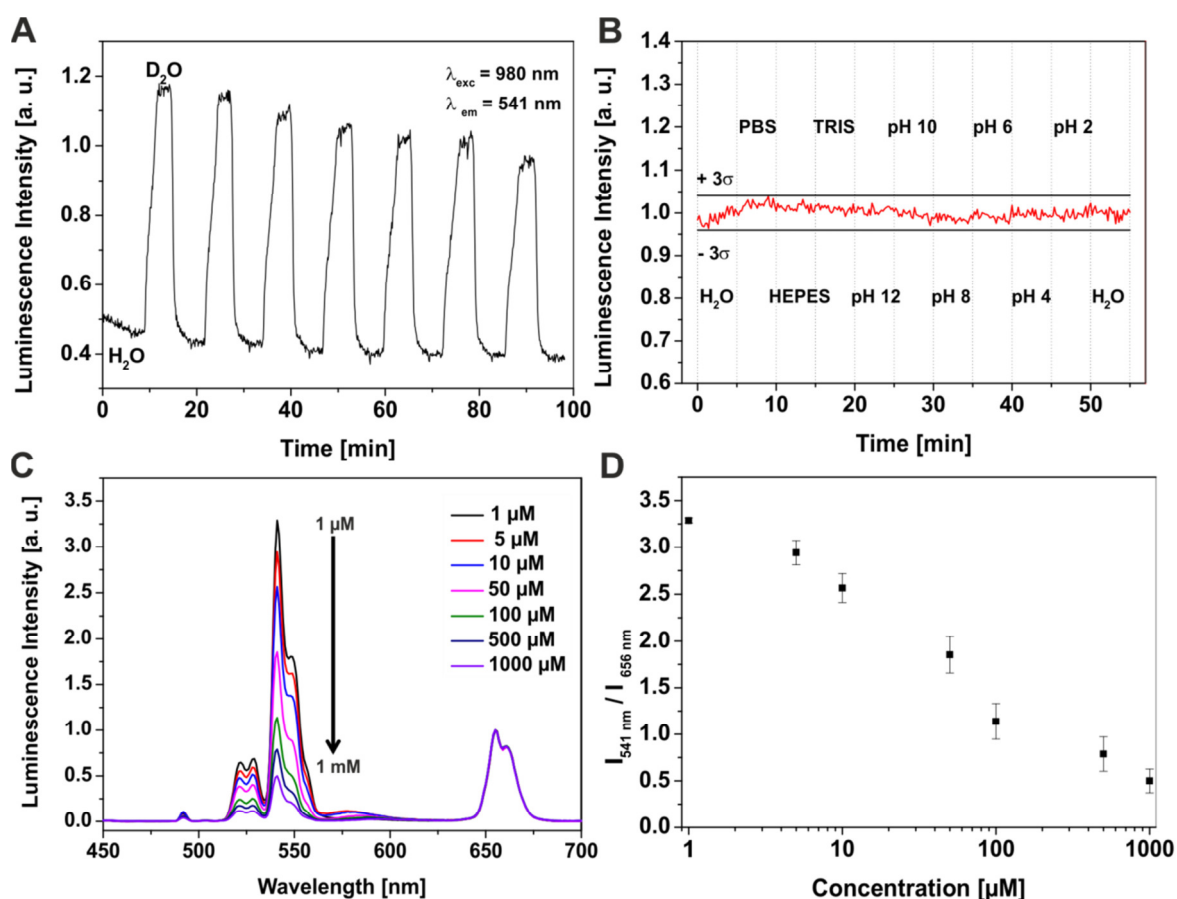
Figure 6.11 ‖ The luminescence intensity of NaYF$_4$ nanoparticles embedded in PVP nanofibers (β(UCNPs) = 40 mg·mL^{-1}, spinning time: 15 min) was recorded at 541 nm in a microfluidic channel. **A**) The nanofibers were flushed alternately with double distilled water and deuterium oxide. **B**) The nanofibers were flushed successively with double distilled water, PBS buffer, HEPES buffer (50 mM, pH 7.4), TRIS buffer (50 mM, pH 7.4), and Britton–Robinson buffers (0.04 M H$_3$PO$_4$, 0.04 M acetic acid, 0.04 M boric acid, pH 2-12). The flow rate was 100 mL·min^{-1}. **C**) Luminescence spectra of the NaYF$_4$:Yb,Er,Gd@NaYF$_4$ nanoparticles embedded in PVP nanofibers (β(UCNPs) = 32 mg·mL^{-1}, spinning time: 15 min) in a microfluidic channel under different Rose Bengal concentrations (1 μM, 5 μM, 10 μM, 50 μM, 100 μM, 500 mM, 1000 μM). **D**) The ratio of the green (541 nm) to red (656 nm) emission was plotted against the concentration of Rose Bengal. The nanofibers were excited with a 980 nm laser module (cw, 200 mW). The flow rate was 25 mL·min^{-1}.

For this experiment the core shell nanoparticles were embedded inside the nanofibers. With their enhanced luminescence properties, thinner fiber mats with higher luminescence properties can be spun avoiding potential signal fluctuations due to deviations of the thickness of the nanofiber mats. With increasing dye concentration within the solution flown through the microfluidic channel the green luminescence of the UCNPs is reduced due to an inner filter effect. In contrast, the red emission of the nanoparticles is not influenced by the fluorescent dye and can be used as a reference peak enabling ratiometric measurements as shown in (**Figure 6.11**). For example, a concentration of 1 mM RB leads to an 85% decrease of the green luminescence (541 nm) of the

embedded particles. Furthermore, linear behavior between the RB concentration and the green luminescence of the nanofibers can be found over three orders of magnitude (LOD = 0.5 µmol·L^{-1}). For low RB concentration the emission of the dye was observed at 580 nm after NIR excitation.
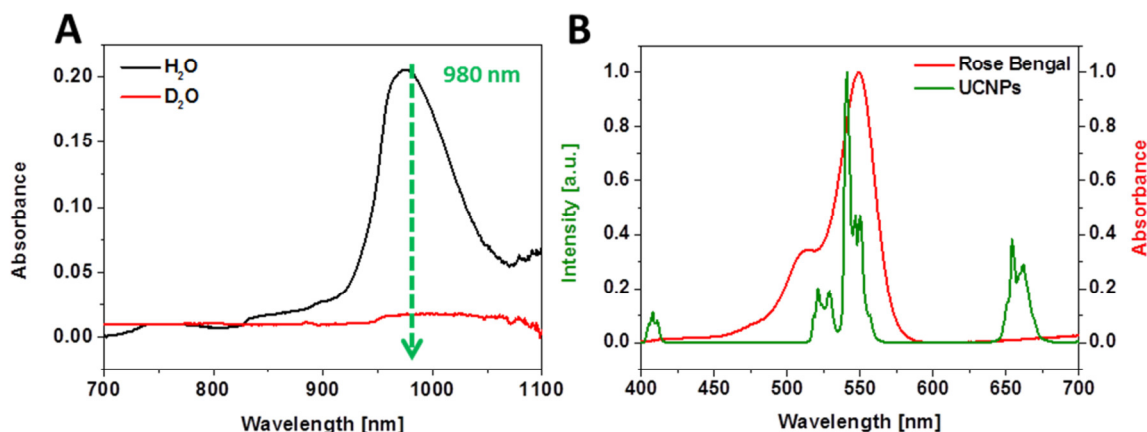
Figure 6.12 ‖ **A**) Absorption spectra of D_2O and H_2O were collected from 700 nm to 1100 nm. The dashed line indicates the absorption at 980 nm. **B**) The spectral overlap between the absorbance spectra of Rose Bengal (red) and the green emission of erbium doped upconversion nanoparticles is shown. The UCNPs were excited at 980 nm. The spectra were collected in water.

6.5 Conclusion

UCNPs were successfully incorporated into PVP nanofibers and were homogeneously distributed. The concentration of the nanoparticles inside the nanofibers can easily be controlled by the particle concentration inside the spinning solution. Hence, the brightness of the nanofibers can be tuned to match the desired application. The luminescence signal inside the nanofibers stays constant in aqueous solutions and is not influenced by buffer or pH changes. This new platform can be expanded to a multimodal platform by extending the emission wavelengths by doping UCNPs with different emitting lanthanide ions (Tm^{3+}, Eu^{3+}, Ho^{3+}). The in situ generated light inside the platform can be used for sensing applications based on the inner filter effect or FRET,[56] but also in microreactors for photocatalysis or as a light source for photoreactions. A multifunctional analytical platform can be achieved by embedding for example BF_4^- stabilized magnetic or catalytic active nanoparticles in the nanofibers without time consuming optimization steps.[36] Overall, this versatile analytical platform for optical online monitoring can be used in almost any bioanalytical environment, including in vivo applications. Due to the NIR excitation this

composite material can be applied to deep tissue both for analyses as well as for controlled drug delivery. By using numerous microfluidic channels high throughput screening for specific analytes can be achieved, requiring only small sample volumes and a simple optical read out.

Acknowledgements

References

1   Z.-M. Huang, Y.-Z. Zhang, M. Kotaki and S. Ramakrishna, A review on polymer nanofibers by electrospinning and their applications in nanocomposites, Compos. *Sci. Technol.*, **2003**, 63, 2223–2253.

2   L. A. Mercante, V. P. Scagion, F. L. Migliorini, L. H. Mattosoand D. S. Correa, Electrospinning-based (bio)sensors for food and agricultural applications, *TrAC*, **2017**, 91, 91–103.

3   J. Xue, J. Xie, W. Liu and Y. Xia, Electrospun nanofibers: new concepts, materials, and applications, *Acc. Chem. Res.*, **2017**, 50, 1976–1987.

4   E. Sapountzi, M. Braiek, J.-F. Chateaux, N. Jaffrezic-Renault and F. Lagarde, Recent advances in electrospun nanofiber interfaces for biosensing devices, *Sensors*, **2017**, 17, 1887.

5   L. Matlock-Colangelo and A. J. Baeumner, Biologically inspired nanofibers for use in translational bioanalytical systems, *Annu. Rev. Anal.Chem.*, **2014**, 7, 23–42.

6   D. Li and Y. Xia, Electrospinning of Nanofibers, *Adv. Mater.*, **2004**, 16, 1151–1170.

7   A. Y. Mikheev, I. L. Kanev, T. Y. Morozova and V. N. Morozov, Water-soluble filters from ultra-thin polyvinylpyrrolidone nanofibers, *J. Membr. Sci.*, **2013**, 448, 151–159.

8   A. R. Rabiatul, Y. Lokanathan, C. M. Rohaina, S. R. Chowdhury, B. S. Aminuddin and B. H. I. Ruszymah, Surface modification of electrospun poly(methyl methacrylate) (PMMA) nanofibers for the development of in vitro respiratory epithelium model, *J. Biomater. Sci., Polym. Ed.*, **2015**, 26, 1297–1311.

9   D. Li, M. W. Frey and A. J. Baeumner, Electrospun polylactic acid nanofiber membranes as substrates for biosensor assemblies, *J. Membr. Sci.*, **2006**, 279, 354–363.

10   L. Matlock-Colangelo, D. Cho, C. L. Pitner, M. W. Frey and A. J. Baeumner, Functionalized electrospun nanofibers as bioseparators in microfluidic systems, *Lab Chip*, **2012**, 12, 1696–1701.

11   S. Jiang, L.-P. Lv, K. Landfester and D. Crespy, Nanocontainers in and onto Nanofibers, Accounts of chemical research, *Acc. Chem. Res.*, **2016**, 49, 816–823.

12   C. W. Kartikowati, A. Suhendi, R. Zulhijah, T. Ogi, T. Iwaki and K. Okuyama, Preparation and evaluation of magnetic nanocomposite fibers containing α"-Fe16N2 and α-Fe nanoparticles in polyvinylpyrrolidone via magneto-electrospinning, *Nanotechnology*, **2016**, 27, 025601.

13   S. Nartker, D. Aryan, L. Wang and M. Stogsdill, Electrospinning and Characterization of Polyvinyl Alcohol Nanofibers with Gold Nanoparticles, *Nanosci. Nanotechnol. Lett.*, **2015**, 7, 718–722.

14   O. C. Ifegwu, C. Anyakora and N. Torto, Nylon 6–Gold Nanoparticle Composite Fibers for Colorimetric Detection of Urinary 1-Hydroxypyrene, *J. Appl. Spectrosc.*, **2015**, 82, 260–265.

15   Z. Ouyang, J. Li, J. Wang, Q. Li, T. Ni, X. Zhang, H. Wang, Q. Li, Z. Su and G. Wei, Fabrication, characterization and sensor application of electrospun polyurethane nanofibers filled with carbon nanotubes and silver nanoparticles, *J. Mater. Chem. B*, **2013**, 1, 2415–2424.

16   G. Xia, L. Zhang, F. Fang, D. Sun, Z. Guo, H. Liu and X. Yu, General synthesis of transition metal oxide ultrafine nanoparticles embedded in hierarchically porous carbon nanofibers as advanced electrodes for lithium storage, *Adv. Funct. Mater.*, **2016**, 26, 6188–6196.

17   M. W. Frey, D. Li, T. Tsong, A. J. Baeumner and Y. L. Joo, Incorporation of biotin into PLA nanofibers via suspension and dissolution in the electrospinning dope, *J. Biobased Mater. Bioenergy*, **2007**, 1, 220–228.

18   J.-P. Chen and C.-H. Su, Surface modification of electrospun PLLA nanofibers by plasma treatment and cationized gelatin immobilization for cartilage tissue engineering, *Acta Biomater.*, **2011**, 7, 234–243.

19   H. S. Yoo, T. G. Kim and T. G. Park, Surface-functionalized electrospun nanofibers for tissue engineering and drug delivery, *Adv. Drug Delivery Rev.*, **2009**, 61, 1033–1042.

20   S. Marx, M. V. Jose, J. D. Andersen and A. J. Russell, Electrospun gold nanofiber electrodes for biosensors, *Biosens.Bioelectron.*, **2011**, 26, 2981–2986.

21   R. Sridhar, S. Sundarrajan, J. R. Venugopal, R. Ravichandran and S. Ramakrishna, Electrospun inorganic and polymer composite nanofibers for biomedical applications, *J. Biomater. Sci. Polym. Ed.,* **2013**, 24, 365–385.

22   M. Shevach, B. M. Maoz, R. Feiner, A. Shapira and T. Dvir, Nanoengineering gold particle composite fibers for cardiac tissue engineering, *J. Mater. Chem. B*, **2013**, 1, 5210–5217.

23   A. GhavamiNejad, A. Rajan Unnithan, A. Ramachandra Kurup Sasikala, M. Samarikhalaj, R. G. Thomas, Y. Y. Jeong, S. Nasseri, P. Murugesan, D. Wu and C. Hee Park, et al., *ACS Appl. Mater. Interfaces*, **2015**, 7, 12176–12183.

24   G. Bai, M. Tsang and J. Hao, Luminescent ions in advanced composite materials for multifunctional applications, *Adv. Funct. Mater.*, **2016**, 26, 6330–6350.

25   F. Zhang, *Nanostructure Science and Technology*, Springer, **2015**.

26   F. Wang and X. Liu, Recent advances in the chemistry of lanthanide-doped upconversion nanocrystals, *Chem. Soc. Rev.*, **2009**, 38, 976–989.

27   M. Haase and H. Schäfer, Upconverting nanoparticles, *Angew. Chem. Int. Ed. Engl.*, **2011**, 50, 5808–5829.

28   J. F. Suyver, J. Grimm, M. K. van Veen, D. Biner, K. W.Krämer and H. U. Güdel, Upconversion spectroscopy and properties of $NaYF_4$ doped with Er^{3+}, Tm^{3+} and/or Yb^{3+}, *J. Lumin.*, **2006**, 117, 1–12.

29   Z. Li, Y. Zhang and S. Jiang, Multicolor core/shell-structured upconversion fluorescent nanoparticles, *Adv. Mater.*, **2008**, 20, 4765–4769.

30   G. Chen, H. Qiu, P. N. Prasad and X. Chen, Upconversion nanoparticles: design, nanochemistry, and applications in theranostics, *Chem. Rev.*, **2014**, 114, 5161–5214.

31   J. Zhou, Z. Liu and F. Li, Upconversion nanophosphors for small-animal imaging, *Chem. Soc. Rev.*, **2012**, 41, 1323–1349.

32   V. Muhr, S. Wilhelm, T. Hirsch and O. S. Wolfbeis, Upconversion nanoparticles: from hydrophobic to hydrophilic surfaces, *Acc. Chem. Res.*, **2014**, 47, 3481–3493.

33   C.-A. J. Lin, R.A. Sperling, J.K. Li, T.-Y.Yang, P.-Y. Li, M. Zanella, W. H. Chang and W. J. Parak, Design of an amphiphilic polymer for nanoparticle coating and functionalization, *Small*, **2008**, 4, 334–341.

34   Y. Bao, Q. A. N. Luu, Y. Zhao, H. Fong, P. S. May and C. Jiang, Upconversion polymeric nanofibers containing lanthanide-doped nanoparticles via electrospinning, *Nanoscale*, **2012**, 4, 7369–7375.

35   Z. Watkins, J. Taylor, S. D'Souza, J. Britton and T. Nyokong, Fluorescence behaviour and singlet oxygen production of aluminium phthalocyanine in the presence of upconversion nanoparticles, *J. Fluoresc.*, **2015**, 25, 1417–1429.

36   A. Dong, X. Ye, J. Chen, Y. Kang, T. Gordon, J. M. Kikkawa and C. B. Murray, A generalized ligand-exchange strategy enabling sequential surface functionalization of colloidal nanocrystals, *J. Am. Chem. Soc.*, **2011**, 133, 998–1006.

37   Q. Ma, J. Wang, X. Dong, W. Yu and G. Liu, Electrospinning fabrication and characterization of magnetic-upconversion fluorescent bifunctional core–shell nanofibers, *J. Nanopart. Res.*, **2014**, 16, 1–10.

38   D. Li, X. Dong, W. Yu, J. Wang and G. Liu, Synthesis and upconversion luminescence properties of YF_3:Yb^{3+}/Er^{3+} hollow nanofibers derived from Y_2O_3:Yb^{3+}/Er^{3+} hollow nanofibers, *J. Nanopart. Res.*, **2013**, 15, 1704.

39   P. Zou, X. Hong, Y. Ding, Z. Zhang, X. Chu, T. Shaymurat, C. Shao and Y. Liu, Up-conversion luminescence of $NaYF_4$:Yb^{3+}/Er^{3+} nanoparticles embedded into PVP nanotubes with controllable diameters, *J. Phys. Chem. C*, **2012**, 116, 5787–5791.

40   Z. Hou, X. Li, C. Li, Y. Dai, P. Ma, X. Zhang, X. Kang, Z. Cheng and J. Lin, Electrospun upconversion composite fibers as dual drugs delivery system with individual release properties, *Langmuir*, **2013**, 29, 9473–9482.

41   F. Zhang, C.-L. Zhang, H.-Y. Peng, H.-P. Cong and H.-S. Qian, Near-infrared photocatalytic upconversion nanoparticles/TiO_2 nanofibers assembled in large scale by electrospinning, *Part. Part. Syst. Charact.*, **2016**, 33, 248–253.

42   Y. Fu, H. Liu, Z. Ren, X. Li, J. Huang, S. Best and G. Han, Luminescent $CaTiO_3$:Yb,Er nanofibers co-conjugated with Rose Bengal and gold nanorods for potential synergistic photodynamic/photothermal therapy, *J. Mater. Chem. B*, **2017**, 5, 5128–5136.

43   K. Park, K. Jung, S. J. Kwon, H. S. Jang, D. Byun, I. K. Han and H. Ko, Plasmonic nanowire-enhanced upconversion luminescence for anticounterfeit devices, *Adv. Funct. Mater.*, **2016**, 26, 7836–7846.

44   K. Presley, J. Hwang, S. Cheong, R. Tilley, J. Collins, M. Viapiano and J. Lannutti, Nanoscale upconversion for oxygen sensing, *Mater. Sci. Eng. C*, **2017**, 70, 76–84.

45   Y. Fu, T. Chen, G. Wang, T. Gu, C. Xie, J. Huang, X. Li, S. Best and G. Han, Production of a fluorescence resonance energy transfer (FRET) biosensor membrane for microRNA detection, *J. Mater. Chem. B*, **2017**, 65, 87.

46   S. Wilhelm, M. Kaiser, C. Wurth, J. Heiland, C. Carrillo-Carrion, V. Muhr, O. S. Wolfbeis, W. J. Parak, U. Resch- Genger and T. Hirsch, Water dispersible upconverting nanoparticles: effects of surface modification on their luminescence and colloidal stability, *Nanoscale*, **2015**, 7, 1403–1410.

47   K. Nasouri, A. M. Shoushtari and M. R. M. Mojtahedi, Evaluation of effective electrospinning parameters controlling polyvinylpyrrolidone nanofibers surface morphology via response surface methodology, *Fibers Polym.*, **2015**, 16(9), 1941–1954.

48   V. Beachley and X. Wen, Effect of electrospinning parameters on the nanofiber diameter and length, *Mater. Sci. Eng. C*, **2009**, 29, 663–668.

49   J.-H. Zeng, J. Su, Z.-H. Li, R.-X. Yan and Y.-D. Li, Synthesis and upconversion luminescence of hexagonal-phase NaYF$_4$: Yb, Er^{3+} phosphors of controlled size and morphology, *Adv. Mater.*, **2005**, 17, 2119–2123.

50   Y. Sheng, L.-D. Liao, A. Bandla, Y.-H. Liu, N. Thakor and M. C. Tan, Size and shell effects on the photoacoustic and luminescence properties of dual modal rare-earth-doped nanoparticles for infrared photoacoustic imaging, *ACS Biomater. Sci. Eng.*, **2016**, 2, 809–817.

51   N. J. J. Johnson, A. Korinek, C. Dong and F. C. J. M. van Veggel, Self-focusing by Ostwald ripening: a strategy for layer-by-layer epitaxial growth on upconverting nanocrystals, *J. Am. Chem. Soc.*, **2012**, 134, 11068–11071.

52   Y. Fu, S. Gong, X. Liu, G. Xu, Z. Ren, X. Li and G. Han, Crystallization and concentration modulated tunable upconversion luminescence of Er^{3+} doped PZT nanofibers, *J. Mater. Chem. C*, **2015**, 3, 382–389.

53   M. Liu, M. Gu, Y. Tian, P. Huang, L. Wang, Q. Shi and C. Cui, Multifunctional CaSc$_2$O$_4$:Yb^{3+}/Er^{3+} one-dimensional nanofibers: electrospinning synthesis and concentration-modulated upconversion luminescent properties, *J. Mater. Chem. C*, **2017**, 5, 4025–4033.

54   L. Matlock-Colangelo, B. Coon, C. L. Pitner, M. W. Frey and A. J. Baeumner, Functionalized electrospun poly(vinyl alcohol) nanofibers for on-chip concentration of E. coli cells, *Anal. Bioanal. Chem.*, **2016**, 408, 1327–1334.

55   C.-W. Tsao and D. L. DeVoe, Bonding of thermoplastic polymer microfluidics, *Microfluid. Nanofluid.*, **2009**, 6, 1–16.

56   V. Muhr, C. Würth, M. Kraft, M. Buchner, A. J. Baeumner, U. Resch-Genger and T. Hirsch, Particle-Size-Dependent Förster Resonance Energy Transfer from Upconversion Nanoparticles to Organic Dyes, *Anal. Chem.*, **2017**, 89, 4868–4874.

7 CONCLUSION AND PERSPECTIVES

Lanthanide-doped nanoparticles have been successfully applied for sensing, theranostic and assays applications regarding their specific optical properties. $GdVO_4$ nanoparticles doped with europium ions are tested in luminescent assays for the detection of H_2O_2. Upconverting nanoparticles (UCNPs) have been established for a theranostic application in photodynamic therapy and for luminescent sensing in microfluidic channels.

$GdVO_4$:Eu nanoparticles change their luminescent properties by varying the europium concentration and in presence of peroxide. This can be utilized in the design of a sensor application for H_2O_2 an important by-product in many enzymatic reactions. It is challenging to detect very low concentrations of H_2O_2 under physiological conditions. Furthermore, biological fluids suffer from scattering and from strong absorbance of light. It is expected that luminescence probes with the highest quantum yield should result in the most sensitive assays. In this work it was possible to demonstrate that for analytical applications in assays this is not necessarily the case. The highest sensitivity in detection of H_2O_2 was achieved for $GdVO_4$ (50% Eu) nanoparticles which have a quantum yield of only one third compared to the brightest $GdVO_4$ (10% Eu) nanocrystals. The quenching efficiency caused by H_2O_2 is more than a hundred times better for $GdVO_4$ (50% Eu) in comparison to $GdVO_4$ (10% Eu). New luminescent nanomaterials are often developed and optimized regarding highest luminescent quantum yield, however for applications as luminescent probes or in assays sensitivity have to be considered and the nanomaterial has to be adapted. A related issue is very often insufficient characterization of the lanthanide nanoparticles, especially the real lanthanide content inside the host lattice. Small variations of the Ln^{3+} ions can lead to significant changes in the optical properties, decreased sensitivity. In our case, we investigated the europium content in $GdVO_4$:Eu by ICP-OES measurements and found large deviations (up to 20%) regarding the theoretical composition of the lanthanide ions used for synthesis. Therefore, one also has to consider the doping strategy in general, as by an exchange on Ln^{3+} also alloys can be formed, or that all Ln^{3+} are not mixable within one host lattice at all ratios. Almost nothing is known about longtime stability of Ln^{3+}-doped nanocrystals in terms of the positions of the dopants within the crystal. First studies show that especially core-shell architectures are prone to exchange ions between the core and the shell. Eu-doped particles would be the best system to study this effect as the luminescence properties of such crystals vary with the concentration of Eu^{3+}. Regarding different crystal architectures and synthesis strategies all of these concerns should be taken into account.

By increasing the europium content inside the nanocrystals, the excitation maximum is shifted to even shorter wavelengths (325 nm $\rightarrow$ 295 nm) causing strong background signals (auto fluorescence) in bioanalytical samples. However, *Stokes* shifts of over 300 nm for the main Eu^{3+} emission at 618 nm minimize the background signals distinctly. The long luminescence lifetime of the europium ions (several hundred µs) offers the opportunity for example for time-gated luminescence imaging or lifetime-based measurements to counteract background luminescence and light scattering of the particles. Lifetime-based measurements are not affected by scattering and are in general independent from the particle concentration. Since the luminescence lifetime of europium is in the µs range, relative simple experimental set ups can be used.

$GdVO_4$ nanoparticles doped with europium ions are not applicable in deep tissue experiments regarding luminescent readout. The tissue penetration of the required UV light for the excitation of the nanoparticles is limited to hundreds of µm, not able to penetrate the epidermis. Here, upconverting nanoparticles are a promising alternative due to their NIR excitation for deeper tissue penetration (up to 8 mm).[1]

Since the efficient synthesis methods regarding size control and size distribution for UCNPs yields in hydrophobic nanocrystals, it is one of the most difficult tasks to fully remove the hydrophobic coating in order to engineer the interface between particle and dispersion media in such way that the particles stay colloidal stable by simultaneous introduction of a functionality which can interact with a target in the media and the light emitted by the particle. This challenge of surface chemistry to envelope an inorganic material by a nanometer thin organic coating providing stability in an aqueous surrounding is currently tackled by many researchers. Different surface modification techniques have been reviewed by us to find the most promising strategy for the preparation of water-dispersible, functionalized upconversion nanoparticles. The three main surface modification techniques are ligand exchange, coating with an amphiphilic polymer and growing of a silica shell. However, the characterization of surface modified UCNPs is only poorly developed and standardized. The particles should be characterized regarding, chemical composition of the surface coating, colloidal stability, zeta potential, particle cross-linking by side reactions, number of functional groups on the surface, yield of particle surface coverage and changes in optical properties. For nanoparticles these parameters are important as one always has to deal with a whole assembly of ligands providing functionality, e.g. in energy transfer systems one has multiple donors within the particle together with a huge number of acceptors located at the surface. The optimization of this ratio is important for designing efficient FRET systems. This was also studied in a joint cooperation with the group of Yves Mely at the Laboratory of Bioimaging and Pathologies in Straßbourg.[2] The results underline the importance of carefully considering

the complex behavior of UCNP–dyes systems before attributing changes in the spectral or in lifetime behavior only to energy transfer events. A new trend for surface modification of upconverting nanoparticles is the tailored synthesis of surface ligands to obtain the desired functionality.[3] Still, colloidal stability of UCNPs in high ionic strength solutions is challenging. A novel approach is to use phosphonic groups combined with carboxylic acid or amine groups. It is assumed, that only the phosphonic acid groups coordinate to the surface of the UCNPs due to their higher binding affinities.[4] The other functional groups should stabilize the nanoparticle due to electrostatic repulsion. Comparative studies have to be performed confirming the superior properties of such a surface architecture.

UCNPs have been successfully designed and prepared for applications as luminescent probes in living cells suitable to induce cell death by singlet oxygen generation upon NIR excitation. In already applied photodynamic therapy (PDT) it is challenging to treat tumors, which are located deep in the tissue due to the short penetration depth of the inserted light source. Further it is difficult to specifically target cancer cells leading to collateral damage of healthy cells. The unique optical property of UCNPs to convert NIR light to visible light was exploited to excite the photosensitizer Rose Bengal (RB) via low energy irradiation. This strategy has two main advantages: a) deeper tissue penetration due to NIR excitation and b) lower photo-toxicity of the excitation light. For high efficiency in singlet oxygen generation, the distance between the emitters (Er^{3+}) and the photosensitizer was kept as short as possible. However here, two conflictive effects have to be considered for the design of the upconverting nanoparticles: a) minimization of non-radiative deactivation of the upconversion luminescence caused by -O-H vibrations[5] by shielding the donors (Er^{3+}) from the particle surface and b) providing a close distance between donors and acceptors (RB), for high energy transfer efficiency. As best compromise, a 0.5 nm thin inert shell of $NaYF_4$ was grown around the particles, which increases the luminescent yield by the factor of 10, minimizing surface quenching and crystal defects. The characterization of such thin shells regarding completeness and integrity is challenging, and regarding reproducibility a critical issue. Since direct attachment of the photosensitizer RB leads to colloidal instable nanoparticles L-lysine was introduced as a short linker molecule for higher binding affinities. A FRET efficiency of 25% was achieved. A future goal would be further surface modifications with antibodies to specifically target cancer cells. With the current surface modification two challenges have to be kept in mind. First, since proteins have many functional groups, cross-linking of the nanoparticles can occur, reducing the overall colloidal stability and the cellular uptake of the functionalized nanoparticles. Secondly, the binding of one single L-lysine to the surface of the nanoparticles might be too weak to connect large proteins to the nanoparticles. Here, for example polymers like polyallylamine can be used as surface ligands to provide higher stability against ligand

detachment after the binding of the antibody. Wilhelm et al. (2016) illustrate that current nanoparticles delivery to tumors is very inefficient, only 0.7% of the administered nanoparticles are found in the tumors.[6] Most of the nanoparticles are intercepted by the mononuclear phagocytic system and the renal clearance pathway. Complete understanding of all involved parameters in particle delivery is very challenging and will take a long time.

Water, with a local absorption maximum at 980 nm, reduces the luminescence intensity of the UCNPs and therefore reduces the energy transfer to the photosensitizer. One strategy to counter this effect is the shift of the excitation wavelength to shorter wavelength by suitable antenna ligands or by co-doping the nanocrystals with Nd^{3+}.[7] Zou et al. (2012) showed that they could enhance the upconversion efficiency by a factor of 3,300 with a NIR dye as an antenna ligand.[8] However, NIR dyes are prone for photobleaching, especially considering lasers as excitation source. Furthermore, the binding of IR sensitive dyes on the surface of the nanoparticles will be in competition with the photosensitizer resulting in lower efficiencies for applications in photodynamic therapy. In case of doping the nanocrystals with Nd^{3+} ions, the excitation wavelength can be shifted to 808 nm.[9] However, it has to be considered, that for efficient upconversion at 808 nm core-shell particles have to be synthesized for spatial separation of the sensitizer and activator ions. This leads to an increase in the distance between activator ions and photosensitizer, probably lowering the energy transfer efficiency, which has to be further investigated.[10]

In general, colloidal stability of the particles is essential for further bioanalytical applications. As shown in **Figure 6.10** non-colloidal dispersions of UCNPs lead to inaccurate and incorrect optical measurements either due to precipitation of the nanoparticles or light scattering on the cloudy dispersion of aggregated nanoparticles.

A strategy to avoid problems regarding colloidal stability is to entrap UCNPs in PVP nanofibermats in microfluidic channels. For high loading capacities of UCNPs inside the PVP nanofibers the surface of UCNPs has to be adapted to the composition of the spinning solution. The $NOBF_4$ assisted surface modification method enables particle concentrations up to 40 mg·mL^{-1} in the spinning solution without the formation of aggregates. After the electrospinning process concentrations up to 254 ± 9 mg·mL^{-1} of the nanoparticles inside the nanofibers were found. In comparison with nanoparticles dispersed in aqueous solutions distinct increase (up to 50 times higher) in particle concentration was achieved.

As a first proof of concept study, the entrapment of UCNPs in nanofibers was investigated in detail by setting-up a microfluidic device for online monitoring. The combination of the new nanomaterial with a microfluidic device has several advantages: a) only small sample volumes are required due to the miniaturization of the setup b) background luminescence

is minimized due to the large anti-*Stokes* shifted emission of the UCNPs, scattering effects of the excitation source are negligible c) visible light can be directly generated inside the microfluidic channels. However, several aspects have to be considered: a) mechanical stability of the fibermats b) transfer of the nanofibersmats c) signal stability inside the microfluidic channel.

The mechanical stability of the nanofiber after the electrospinning process has to be increased for the application in microfluidics. Sintering of the nanofibers (800 -900 °C) would lead to brittle nanofibermats hindering a successful transfer of the fibermats. By heat treatment at 175 °C cross-linking of the nanofibermats was obtained improving mechanical stability of the nanofibermats. They were transferred by a hot embossing method to the microfluidic chip system. Here it was important to conserve the three-dimensional structure of the fibermats taking advantage of their large surface-to-volume ratios inside the channel.

Leakage free entrapment of the nanoparticles is a requirement for the development of a label-free sensing device. For the first-time stable luminescent signal was obtained for a wide pH range (2-12). Also, solvent exchanges could be performed in several minutes without considering colloidal stability of the particles. Solvent changes for dispersed particles require time consuming steps, like centrifugation or dialysis, which are always related with a potential loss of UCNPs.

For sensing application on surfaces upconverting nanoparticles have the unique advantages due to their anti-*Stokes* shifted emission. Scattering effects of the excitation source on the matrix (nanofibers) did not influence the optical readout. Visible light can be directly generated inside the microfluidic channels after NIR excitation. With the well separated emission bands of the UCNPs ratiometric measurements can be performed, showed with RB as a model dye. Ratiometric measurements supersede calibrations steps for every measuring sequence. By changing the composition of the UCNPs even UV-light can be generated in the microfluidic system, which may be also interesting for photo catalytic reaction in the future.

Nanofibermats containing upconverting nanoparticles have also interesting properties for theranostic application like drug delivery or photodynamic therapy for treatment of early stage or inoperable tumors. By entrapping the nanoparticles in the nanofibers, the inefficient nanoparticle delivery to tumors could be omitted. After placing the fibermats around the tumor, repeated laser irradiation with NIR light can be used for cancer treatment. It has to be taken into account that laser irradiation with 980 nm would lead to an overheating effect in the target tissue, therefore the excitation wavelength has to be shifted, for example to 808 nm by co-doping of the nanocrystals with Nd^{3+}. Surface modification of the nanofibers with the photosensitizer, thinner nanofibers for efficient

energy transfer from the embedded nanoparticles to the photosensitizer and biocompatible[11] have to be investigated in the future.

Ramachandran et al (2017) used electrospun nanofibers to develop brain-implants for the prolonged treatment of recurrent glioma.[12] Upconverting nanoparticles can be applied for an alternative triggered drug release by in situ generation of light.

In general, one can conclude, that lanthanide doped nanoparticles have a bright future in bioanalytical applications. Demanding standardization in precise characterization, they are able to offer new approaches in assays, sensor and theranostic applications. Their large *Stokes*, respectively anti-*Stokes* shifted emissions, together with their long luminescent lifetimes are major advantages compared to organic dyes, which suffer from high background signals in biological samples. Multimodal lanthanide doped nanoparticles are promising materials for future applications, combining theranostic with imaging techniques. For example, upconverting nanoparticles modified for photodynamic therapy are functionalized with cancer antibodies. Co-doping of the nanocrystals with Gd^{3+} ions enables magnetic resonance imaging and localization of tumors. After activation with NIR light singlet oxygen can directly be generated in the cancer cells.

However, short- and long-time cytotoxic effects of the lanthanide doped nanoparticles have to be further investigated. General statements about their toxicity cannot be made, since toxic effects are depended on the chemical composition, size and morphology, surface architecture, chemical and physical environment of the nanoparticles. Regarding lanthanide doped nanoparticles low toxicity is asserted, however again reports about long-term toxicity of the particles are missing.[13] Secondary toxicity effects after potential decomposition (e.g. in liver) of the nanoparticles and interaction with other biological molecules have also to be considered.

References

1   S. Wu and H.-J. Butt, Near-infrared-sensitive materials based on upconverting nanoparticles, *Adv. Mat.*, **2016**, 28, 1208–1226.

2   O. Dukhno, F. Przybilla, M. Collot, A. Klymchenko, V. Pivovarenko, M. Buchner, V. Muhr, T. Hirsch, and Y. Mély. Quantitative assessment of energy transfer in upconverting nanoparticles grafted with organic dyes. *Nanoscale* **2017**, 9, 11994-12004.

3   Y. Chen, H. T. T. Duong, S. Wen, C. Mi, Y. Zhou, O. Shimoni, S. M. Valenzuela and D. Jin, Exonuclease III-assisted upconversion resonance energy transfer in a wash-free suspension DNA assay, *Analy. Chem.*, **2018**, 90, 663–668.

4   Y. Que, C. Feng, G. Lu and X. Huang, Polymer-coated ultrastable and biofunctionalizable lanthanide nanoparticles, *ACS Appl. Mater. Interfaces*, **2017**, 9(17), 14647.

5   C. Würth, M. Kaiser, S. Wilhelm, B. Grauel, T. Hirsch and U. Resch-Genger, Excitation power dependent population pathways and absolute quantum yields of upconversion nanoparticles in different solvents, *Nanoscale,* **2017**, 9, 4283–4294.

6   S. Wilhelm, A. J. Tavares, Q. Dai, S. Ohta, J. Audet, H. F. Dvorak and W. C. W. Chan, Analysis of nanoparticle delivery to tumours, *Nat. Rev. Mater.*, **2016**, 1, 16014.

7   M. K. G. Jayakumar, N. M. Idris, K. Huang and Y. Zhang, A paradigm shift in the excitation wavelength of upconversion nanoparticles, *Nanoscale*, **2014**, 6, 8441–8443.

8   W. Zou, C. Visser, J. A. Maduro, M. S. Pshenichnikov and J. C. Hummelen, Broadband dye-sensitized upconversion of near-infrared light, *Nature Photon.*, **2012**, 6, 560–564.

9   S. F. Himmelstoß, L. M. Wiesholler, M. Buchner, V. Muhr, S. Märkl, A. J. Baeumner, and T. Hirsch. 980 nm and 808 nm excitable upconversion nanoparticles for the detection of enzyme-related reactions. *Proc. SPIE* **2017**, 100770L.

10   D. Chen, L. Liu, P. Huang, M. Ding, J. Zhong and Z. Ji, Nd^{3+}-sensitized Ho^{3+} single-band red upconversion luminescence in core-shell nanoarchitecture, *J. Phys. Chem. Lett.*, **2015**, 6, 2833–2840.

11   X. Sun, Q. Lang, H. Zhang, L. Cheng, Y. Zhang, G. Pan, X. Zhao, H. Yang, Y. Zhang, H. A. Santos and W. Cui, Electrospun photocrosslinkable hydrogel fibrous scaffolds for rapid in vivo vascularized skin flap regeneration, *Adv. Funct. Mater.*, **2017**, 27, 1604617.

12   R. Ramachandran, V. R. Junnuthula, G. S. Gowd, A. Ashokan, J. Thomas, R. Peethambaran, A. Thomas, A. K. K. Unni, D. Panikar, S. V. Nair and M. Koyakutty, Theranostic 3-Dimensional nano brain-implant for prolonged and localized treatment of recurrent glioma, *Sci. Rep.*, **2017**, 7, 43271.

13   A. Gnach, T. Lipinski, A. Bednarkiewicz, J. Rybka and J. A. Capobianco, Upconverting nanoparticles: assessing the toxicity, *Chem. Soc. Rev.*, **2015**, 44, 1561–1584.

8 SUMMARY

This thesis presents the design, synthesis, surface modification and characterization of lanthanide doped nanoparticles for bioanalytical applications in assays, sensing and theranostic approaches. In **Chapter 1** nanoparticles are classified regarding their properties. Lanthanide doped nanoparticles are introduced as an interesting alternative to commercial dyes. The mechanism of downconversion and upconversion are explained in detail. Several strategies are introduced to enhance the luminescence properties of upconverting nanoparticles in aqueous solutions.

In **Chapter 2** the aim of the work is described as the identification and preparation of lanthanide doped nanoparticles for (bio)analytical applications considering their unique optical properties. For sensing, assays or theranostics different properties of the nanomaterial are required, additionally intelligent surface engineering may be necessary.

$GdVO_4$ nanoparticles doped with europium are studied as a potential luminescent probe for hydrogen peroxide in **Chapter 3**. The sensitivity to H_2O_2 is depended on the europium concentration inside the nanocrystals. Higher europium concentrations (>10%) lead to lower luminescent quantum yields, but higher sensitivities. $GdVO_4$:Eu (50%) are identified as the efficient luminescent probe for H_2O_2 with a dynamic range from 5 to 250 µM and with a limit of detection of 1.6 µM. Selectivity tests show no significant changes in luminescence for physiological relevant ions (Ca^{2+}, Mg^{2+}, Zn^{2+}). The ability to monitor enzyme-based reaction is proven by glucose oxidase catalyzed detection of glucose. The applicability of the fluorescent nanoparticles is illustrated by the determination of glucose in fetal bovine serum by the standard addition method. Here, good accordance with a commercial sensor can be demonstrated.

In **Chapter 4** functionalization aspects of water dispersible upconversion nanoparticles are discussed. After a short introduction the three main synthesis strategies for upconverting nanoparticles are introduced: thermolysis, Ostwald ripening and hydrothermal strategy. The necessity of surface modifications is explained and ligand exchange method, coating with an amphiphilic polymer and formation of a silica shell are presented as the most interesting techniques to achieve water dispersibility. The reliability of the surface modifications is evaluated according the functionalization of the upconverting nanoparticles with proteins, nucleic acids or dyes. A guideline for the choice of surface engineering for specific bioanalytical applications is established. For sensor applications of the upconverting nanoparticles via energy transfer processes to organic

dyes short distances between emitters and absorbers are favored, which can be accomplished by the ligand exchanges method or by mesoporous silica shells. Coatings with an amphiphilic polymer and with silica are suitable for applications of UCNPs in electrophoresis and cellular imaging. Both surface modification techniques are stable against the detachment of the surface layer. The suitability of the ligand exchange method for cellular application strongly depends on the binding sites to the nanoparticle of the inserted ligand. Here, polymers like polyacrylic acid with many coordinating groups have better stability compared to monodentate ligands.

Chapter 5 describes the application of upconverting nanoparticles in photodynamic therapy. In the first step small and bright core-shell nanoparticles NaYF$_4$:Yb,Er,Gd@NaYF$_4$ are synthesized by thermal decomposition combined with Ostwald ripening method in high boiling solvents. The ligand oleate is replaced by L-lysine to achieve water dispersibility and to bind the photosensitizer Rose Bengal close to the surface of the nanoparticles. Intensity based measurements indicate an energy transfer from the green emission of the Er^{3+} doped UCNPs, confirmed by lifetime measurements, where a FRET efficiency of 25% is calculated. The production of singlet oxygen after NIR excitation is proven with the fluorescent probe 9,10-anthracenediyl-bis(methylene)dimalonic acid. Cellular uptake in human breast cancer cells (SK-BR 3) is confirmed by confocal and two photon microscopy. MTT assays of SK-BR 3 cells show already significant cell death at particle concentrations of 10 µg·mL^{-1} after NIR excitation. After cell death a staining of the cell nuclei with the functionalized nanoparticles is observed in confocal microscopy allowing live/dead imaging without further treatment.

In **Chapter 6** UCNPs are entrapped in electrospun 1-D nanofibers to enable ratiometric sensing in microfluidic channel systems. The nanoparticles are distributed homogeneously inside the nanofibers without forming aggregates. The mass concentration of the nanolamps inside the nanofibers is up to 254 ± 9 mg·mL^{-1} showing a significant increase (up to 50 times) compared to common mass concentration achieved in aqueous solutions. The optical properties of the green (541 nm) and red emission bands (656 nm) of Yb,Er doped UCNPs maintain unchanged after NIR excitation and visible light can be directly generated in the nanofibers. The fibermats are transferred to a microfluidic chip system by hot bonding. The luminescence signal of nanolamps inside the microfluidic channels is not affected by ionic strength or different pH values (2-14), however, shows remarkable and reproducible changes for molecules without the ability to quench the upconversion luminescence, e.g. deuterium oxide (D$_2$O). Ratiometric sensing is tested with the dye Rose Bengal, which absorbs the green light while the red emission

keeps unaffected. The dynamic range is from 1 to 1000 μM with a limit of detection of 0.1 μM.

Chapter 7 provides a critical discussion about the advantages and requirements of lanthanide doped nanoparticles for (bio)analytic application. Future perspectives and challenges of the different nanomaterials in assays, sensing and theranostic applications are validated and different approaches are addressed.

9 ZUSAMMENFASSUNG

Diese Dissertation befasst sich mit der Anwendung von Lanthanoid-dotierten Nanopartikeln in Bereichen der Theranostik, Sensorik und chemischen Assays. Im **1. Kapitel** werden Nanomaterialen anhand ihrer unterschiedlichen Eigenschaften klassifiziert. Lanthanoid-dotierte Nanopartikel stellen eine bemerkenswerte Alternative zu den weit verbreiteten organischen Farbstoffen dar. Der Mechanismus der abwärts- und aufwärtskonvertierenden Nanopartikel wird im Detail erklärt. Es werden verschiedene Strategien vorgestellt, um die Lumineszenz Eigenschaften der aufkonvertierenden Nanopartikel in wässrigen Lösungen zu verbessern.

Das Ziel dieser wissenschaftlichen Arbeit wird im **2. Kapitel** als die Identifizierung und Synthese von Lanthanoid-dotierten Nanopartikeln für (bio)analytischen Anwendungen, unter Berücksichtigung ihrer einzigartigen optischen Eigenschaften beschrieben. Für die Anwendung in chemischen Assays, in Sensoren und der Theranostik werden unterschiedliche Eigenschaften der Nanomaterialien benötigt. In einigen Fällen ist zudem eine intelligente Oberflächenmodifikation der Nanomaterialien erforderlich.

In **Kapitel 3** werden Europium-dotierte $GdVO_4$ Nanopartikel als potenzielle Sonden für die Detektion von Wasserstoffperoxid untersucht. Die Sensitivität gegen H_2O_2 hängt von der Europium-Konzentration in den Nanokristallen ab. Höhere Konzentrationen (>10%) senken die Quantenausbeute des Materials, verbessern aber die Sensitivität gegen H_2O_2. $GdVO_4$ (50%) erweisen sich als die effizientesten lumineszierenden Sonden für H_2O_2 mit einem dynamischen Bereich von 5 bis 250 µM und einer Nachweisgrenze von 1.6 µM. Selektivitätsuntersuchungen gegen physiologisch relevante Ionen wie (Ca^{2+}, Mg^{2+}, Zn^{2+}) zeigen keine signifikanten Änderungen in der Lumineszenz der Europium dotierten Nanopartikel. Die Fähigkeit enzymkatalysierte Reaktionen zu verfolgen, wird durch die Glukose-Oxidase katalysierte Oxidation von Glukose bewiesen. Die praktische Verwendbarkeit der fluoreszierenden Nanopartikel wird durch die Bestimmung von Glukose im fetalen Kälberserum mithilfe der Standardadditionsmethode dargestellt. Die ermittelten Analytkonzentrationen zeigen eine sehr gute Übereinstimmung mit denen eines handelsüblichen Glukose Messgeräts wie man es in Apotheken kaufen kann.

In **Kapitel 4** werden Funktionalisierungsaspekte von in Wasser dispergierbaren aufkonvertierenden Nanopartikel diskutiert. Nach einer kurzen Einführung werden die drei wichtigsten Synthesestrategien für die Nanopartikel vorgestellt: Thermolyse, Ostwald Reifung und Hydrothermalsynthese. Es wird die Notwendigkeit von

Oberflächenmodifikation erläutert und der Ligandenaustausch, das Umschichten mit einem amphiphilen Polymer sowie die Erzeugung einer Silicahülle werden als die vielversprechendsten Techniken vorgestellt, um die Dispergierbarkeit in Wasser zu erreichen. Die Anwendbarkeit der Oberflächenmodifizierungen wird hinsichtlich der Funktionalisierung der aufkonvertierenden Nanopartikel mit Proteinen, Nukleinsäuren und Farbstoffen untersucht. Eine Richtlinie bei der Wahl von Oberflächenmodifizierungen für spezifische bioanalytische Anwendungen wird erarbeitet. Für Sensor Anwendungen, welche auf einem Energietransfer von Nanopartikeln zu Farbstoffen (und umgekehrt) beruhen, werden kurze Abstände zwischen Donor und Akzeptor bevorzugt, die durch Ligandenaustausch oder durch mesoporöse Silicahüllen ermöglicht werden. Ummanteln der Nanopartikel mit einem amphiphilen Polymer und Silica eignen sich besonders für Anwendungen in der Elektrophorese und zellulären Bildgebungsverfahren. Beide Techniken sind stabil gegen die Ablösung ihrer organischen Oberflächenmoleküle. Die Eignung der Ligandenaustausch Methode für zelluläre Anwendungen hängt stark von der „Zähnigkeit" des verwendeten Liganden ab. Hier zeigt sich, dass Polymere wie die Polyacrylsäure mit vielen möglichen Koordinationsgruppen größere Stabilität besitzen als „einzähnige" Liganden.

Kapitel 5 beschreibt die Anwendung von aufkonvertierenden Nanopartikel in der photodynamischen Therapie. Im ersten Schritt werden möglichst kleine und helle Kern-Hülle Nanopartikel ($NaYF_4$:Yb,Er,Gd@$NaYF_4$) durch thermische Zersetzung kombiniert mit Ostwald Reifung in hochsiedenden Lösemittel hergestellt. Der ursprüngliche Ligand Oleat wird durch L-lysine für die Dispergierbarkeit der Nanopartikel in Wasser und für Anbindung des Photosensibilisators Rose Bengal nahe der Oberfläche ersetzt. Intensitätsbasierte Messungen deuten einen Energietransfer von der grünen Emission der Er^{3+} dotierten Nanopartikel an den Photosensibilisator an. Dieser konnte durch Lebenszeit Messungen am Partikel bestätigt und eine FRET-Effizienz von 25% berechnet werden. Die Produktion von Singulett Sauerstoff nach Infrarotanregung wird durch den Fluoreszenzfarbstoff 9,10-anthracenediyl-bis(methylene)dimalon Säure nachgewiesen. Die zelluläre Aufnahme in menschlichen Brustkrebszellen (SK-BR 3) bestätigen die Konfokal- und Zwei-Photonen-Mikroskop Aufnahmen. Viabilitätstest mit SK-BR 3 Zellen zeigt einen deutlichen Zelltod bei einer Partikel Konzentration von 10 µg·mL^{-1} nach Anregung im NIR Bereich. Nach Eintreten des Zelltodes kann im Konfokal Mikroskop eine Markierung der Zellkerne mit den funktionalisierten Nanopartikeln festgestellt werden.

In **Kapitel 6** werden aufkonvertierende Nanopartikel in 1D-Nanofasern eingebunden, um ratiometrische Sensorik in mikrofluidischen Kanälen zu ermöglichen. Die Nanopartikel sind homogen in den Nanofasern verteilt und zeigen keine Aggregatbildung. Die

Massenkonzentration der Nanolampen in den Nanofasern kann auf bis zu 254 ± 9 mg·mL^{-1} erhöht werden, was eine signifikante Erhöhung (bis zum 50fachen) im Vergleich zur Massenkonzentration in wässrigen Dispersionen ist. Die optischen Eigenschaften der grünen (541 nm) und roten Emissionsbanden (656 nm) von den Yb,Er dotierten aufkonvertierenden Nanopartikeln bleiben unverändert und sichtbares Licht kann direkt in den Nanofasern erzeugt werden. Die Fasermatten werden in ein mikrofluidisches Chipsystem transferiert. Das lumineszierende Signal der Nanolampen in den Kanälen wird durch Änderung der Ionenstärke oder des pH-Wertes von den Lösungen nicht beeinflusst, zeigt aber bemerkenswerte und reproduzierbare Signaländerungen gegen schweres Wasser (D_2O). Ratiometrische Sensorik wird mit dem Farbstoff Rose Bengal getestet, welches das grüne Licht absorbiert, während die rote Lumineszenz nicht beeinflusst wird. Der dynamische Bereich liegt bei 1 bis 1000 µM mit einer Nachweisgrenze von 0.1 µM.

Kapitel 7 beinhaltet eine kritische Diskussion über die Vorteile und Anforderungen von Lanthanoid-dotierten Nanopartikeln für die (Bio)Analytik. Zukünftige Herausforderungen für die Anwendung der unterschiedlichen Nanomaterialen in Assays, Sensorik und Theranostik werden aufgezeigt und Lösungsansätze diskutiert.

CURRICULUM VITAE

Personal data

Name: Markus Buchner

Date of birth: 07.02.1988

Birth place: Landshut

Nationality: German

Studies

9/2014 – 3/2018   PHD thesis, Institute of Analytical Chemistry, Chemo- and Biosensors, University of Regensburg
"Surface Engineering of Lanthanide-Doped Nanoparticles for Assays, Sensing and Theranostic Applications"
Supervisor: Prof. Dr. Antje Baeumner and Dr. Thomas Hirsch

10/2012 – 6/2014   Master of Science in Chemistry, University of Regensburg
Master thesis, Institute of Analytical Chemistry, Chemo- and Biosensors:
"Lanthanide-Doped Nanoparticles Amenable to Bioconjugation with Enhanced Luminescence Properties"
Supervisor: PD. Dr. Axel Duerkop and Dr. Thomas Hirsch

10/2008 – 8/2012   Bachelor of Science in Chemistry, University of Regensburg
Bachelor thesis, Institute of Organic Chemistry:
"Kooperative Elektrozyklisierungen"
Supervisor: Prof. Dr. Kirsten Zeitler

Military Service

7/2007 – 8/2008   Panzergrenadierbataillon 112, Bayerwald-Kaserne, Regen

Education

1998 – 2007	A levels, Burkhart Gymnasium Mallersdorf-Pfaffenberg
1994 – 1998	Primary school, Grundschule Ergoldsbach

Awards

9/2015	11th Workshop on Biosensor & Bioanalytical Microtechniques in Environmental, Food & Chemical Analysis: Young Scientist Poster Award

Additional Qualifications

2015	Participation in block seminar: "Qualitätssicherung in der Analytischen Chemie".
2017	Participation in seminar: "Polymer Chemistry: from physical basics to microencapsulation and fiber application."

PUBLICATIONS

(1) **M. Buchner*,** P. García Calavia*, V. Muhr, A. Baeumner, T. Hirsch, M. J. Marín and D. A. Russell., Photosensitiser Functionalized Luminescent Upconverting Nanoparticles for Efficient Photodynamic Therapy of Breast Cancer Cells. Submitted to Nanoscale.

(2) V. Muhr, **M. Buchner**, L. Sauer, B. Goricnik, J. Wegener, A. J. Baeumner, and T. Hirsch. Surface Engineering of Upconversion Nanoparticles for Time-Resolved Analysis of ATP-Responsive Energy Transfer. Submitted to ACS Applied Materials & Intefaces.

(3) **M. Buchner**, U. Ngoensawat, M. Schenck, C. Fenzl, N. Wongkaew, L. Matlock-Colangelo, T. Hirsch, A. Duerkop and A. J. Baeumner, Embedded nanolamps in electrospun nanofibers enabling online monitoring and ratiometric measurements, *J. Mater. Chem. C*, **2017**, 5, 9712–9720.

(4) O. Dukhno, F. Przybilla, M. Collot, A. Klymchenko, V. Pivovarenko, **M. Buchner**, V. Muhr, T. Hirsch, and Y. Mély. Quantitative Assessment of Energy Transfer in Upconverting Nanoparticles Grafted with Organic Dyes. *Nanoscale* **2017**, 9, 11994-12004.

(5) V. Muhr, C. Würth, M. Kraft, **M. Buchner**, A. J. Baeumner, U. Resch-Genger, and T. Hirsch. Particle Size-dependent Förster Resonance Energy Transfer from Upconversion Nanoparticles to Organic Dyes. *Anal. Chem.* **2017**, 89, 4868–4874.

(6) S. F. Himmelstoß, L. M. Wiesholler, **M. Buchner**, V. Muhr, S. Märkl, A. J. Baeumner, and T. Hirsch. 980 nm and 808 nm Excitable Upconversion Nanoparticles for the Detection of Enzyme-related Reactions. *Proc. SPIE* **2017**, 100770L.

(7) V. Muhr*, **M. Buchner***, T. Hirsch, D. J. Jovanović, S. D. Dolić, M. D. Dramićaninb, and O. S. Wolfbeis. Europium-doped GdVO$_4$ Nanocrystals as a Luminescent Probe for Hydrogen Peroxide and for Enzymatic Sensing of Glucose. *Sens. Actuators B Chem* **2017**, 241, 349-356.

(8) **M. Buchner*,** V. Muhr*, S. F. Himmelstoß, and T. Hirsch. Functionalization Aspects of Water Dispersible Upconversion Nanoparticles. In: C. Altaville (ed) Upconverting Nanomaterials – Perspectives, Synthesis and Application. Taylor & Francis, Boca Raton, FL, **2016**, p 69-100.

 * authors contributed equally

PRESENTATIONS

Poster Presentations

9. Deutsches BioSensor Symposium (DBS), 2015, München, Germany:
"Europium-Doped Nanoparticles Amenable to Bioconjugation with Enhanced Luminescence Properties"

ANAKON, 2015, Graz, Austria:
"Europium-Doped Nanoparticles Amenable to Bioconjugation with Enhanced Luminescence Properties"

Conference on Methods and Applications in Fluorescence 14 (MAF), 2015, Würzburg, Germany:
"Functionalization of Luminescent Upconverting Nanoparticles by Photosensitizers for Photodynamic Therapy"

11th Workshop on Biosensor & Bioanalytical Microtechniques in Environmental, Food & Chemical Analysis (BBMEC), 2015, Regensburg, Germany:
"Functionalization of Luminescent Upconverting Nanoparticles by Photosensitizers for Photodynamic Therapy"

Oral Presentations

COST-Meeting, 2015, Regensburg, Germany:
"Surface Modification of Upconverting $NaYF_4$-Nanoparticles for Photodynamic Therapy (PDT)"

10. Interdisziplinäres Doktorandenseminar, 2016, Berlin, Germany:
"Functionalization of Luminescent Upconverting Nanoparticles by Photosensitizers for Photodynamic Therapy"

ANAKON, 2017, Tübingen, Germany:
"Embedded Nanolamps in Electrospun Nanofibers Enabling Online Monitoring and Ratiometric Measurements in Microfluidic Systems"

EIDESSTATTLICHE ERKLÄRUNG

Ich erkläre hiermit an Eides statt, dass ich die vorliegende Arbeit ohne unzulässige Hilfe Dritter und ohne Benutzung anderer als der angegebenen Hilfsmittel angefertigt habe; die aus anderen Quellen direkt oder indirekt übernommenen Daten und Konzepte sind unter Angabe des Literaturzitats gekennzeichnet.

Weitere Personen waren an der inhaltlich-materiellen Herstellung der vorliegenden Arbeit nicht beteiligt. Insbesondere habe ich hierfür nicht die entgeltliche Hilfe eines Promotionsberaters oder anderer Personen in Anspruch genommen. Niemand hat von mir weder unmittelbar noch mittelbar geldwerte Leistungen für Arbeiten erhalten, die im Zusammenhang mit dem Inhalt der vorgelegten Dissertation stehen.

Die Arbeit wurde bisher weder im In- noch im Ausland in gleicher oder ähnlicher Form einer anderen Prüfungsbehörde vorgelegt.

Ort, Datum   Unterschrift